

Role of WD domain of ATG16L1 in maintaining autophagy and tissue homeostasis in mice

Shashank Rai

**A Thesis submitted for the degree of Doctor of
Philosophy (PhD)**

**Norwich Medical School
School of Medicine and Health Sciences
University of East Anglia
2019**

This copy of the thesis has been supplied on condition that anyone who consults it is understood to recognise that its copyright rests with the author and that use of any information derived there-from must be in accordance with current UK Copyright Law. In addition, any quotation or extract must include full attribution.

Abstract:

Macroautophagy or canonical autophagy, referred to as autophagy hereafter, delivers damaged proteins and organelles to lysosomes for degradation and plays important roles in maintaining tissue homeostasis by reducing tissue damage. During autophagy substrates are sequestered in double-membraned autophagosomes within the cytoplasm which recruit LC3 to facilitate fusion with lysosomes.

A related pathway, called non-canonical autophagy, conjugates LC3 to single-membraned endosomes, phagosomes or lysosomes during the entry of extracellular material. Examples include engulfment of neighbouring cells by entosis, uptake of apoptotic cells, and micropinocytosis. In phagocytic cells, such as macrophages and dendritic cells, recruitment of LC3 to phagosomes occurs during pathogen uptake and is called LC3-associated phagocytosis (LAP).

The relative roles played by autophagy and non-canonical autophagy 'in vivo' are poorly understood. Studies on autophagy in mice have relied on inactivation of essential autophagy proteins, however these proteins are also required for non-canonical autophagy, and mouse models are defective in both pathways. The recruitment of LC3 to membranes during both, autophagy and non-canonical autophagy/ LAP, requires the E3 ligase-like activity of the ATG12-ATG5-ATG16L1 complex. The WD domain of ATG16L1 is required for non-canonical autophagy and LAP, but is not required for autophagy. This finding was employed to create mice defective in non-canonical autophagy and LAP by removing WD domain from the *Atg16L1* gene. These mice (called E230) expressed the glutamate residues at 226 and 230 positions in the coiled-coil domain (CCD) of ATG16L1 protein required for binding with WIPI2, an interaction needed for autophagy. A second mouse model was generated that lacked the E230 residue required for autophagy and was called E226.

MEFs from E226 mice were defective in both autophagy and non-canonical autophagy. E226 mice showed growth defects and analysis of liver, kidney, muscle and brain showed accumulation of autophagy substrates p62 and LC3. MEFs from the E230 mice were defective in non-canonical autophagy but could activate autophagy. The E230 mice survived postnatal starvation and grew normally. Liver, kidney, brain and muscle of E230 mice maintained levels of autophagy substrates p62 and LC3 that were the same as littermate controls. Tissue damage associated with loss of autophagy such as presence of p62 inclusions and inflammation were observed in tissue of E226 mice but were absent from E230 mice. This comparative study suggests that autophagy maintains tissue homeostasis in mice independently of the WD domain of ATG16L1 required for non-canonical autophagy/LAP. A comparison of ATG5-ATG12-ATG16L1 complexes formed in liver and brain suggested that autophagy in the brain may be less dependent on strong interactions between WIPI2 and ATG16L1 than in liver. It is possible that E226 mice, which lack E230 required for strong WIPI2 binding, maintain autophagy in the brain to survive neonatal starvation.

Table of contents:

| | |
|---|----|
| List of abbreviations..... | 5 |
| List of figures..... | 8 |
| List of tables..... | 9 |
| Acknowledgement | 10 |
| Chapter 1 | |
| Introduction..... | 11 |
| 1. Autophagy..... | 11 |
| 1.1 Core components of autophagy..... | 11 |
| 1.1.1 Autophagosome Initiation (phagophore nucleation)..... | 11 |
| 1.1.2 Phagophore expansion..... | 13 |
| 1.1.3 Cargo sequestration..... | 16 |
| 1.1.4 Autophagosome fusion with lysosomes..... | 18 |
| 1.2 Non-canonical autophagy and LC3-associated phagocytosis (LAP)..... | 21 |
| 1.2.1 LC3-associated phagocytosis (LAP)..... | 21 |
| 1.2.2 Non-canonical autophagy..... | 23 |
| 1.2.3 Distinguishing between roles of autophagy and LAP..... | 23 |
| 1.3 The WD domain of ATG16L1 is required for non-canonical autophagy..... | 25 |
| 1.4 Rationale for deleting WD domain in mice..... | 28 |
| 1.5 Specific aims..... | 29 |
| Chapter 2 | |
| Materials and methods..... | 31 |
| 2.1 Genotyping..... | 31 |
| 2.1.1 Reagents..... | 31 |
| 2.1.2 Polymerase chain reaction (PCR)..... | 31 |
| 2.1.3 Agarose gel electrophoresis..... | 32 |
| 2.2 Isolation and culture of primary cells..... | 33 |
| 2.2.1 Reagents..... | 33 |
| 2.2.2 Mouse embryonic fibroblasts (MEFs)..... | 34 |
| 2.2.3 Mouse skin fibroblasts..... | 34 |
| 2.2.4 Mouse bone marrow derived macrophages (BMDMs)..... | 34 |
| 2.3 LC3-associated phagocytosis (LAP) assay..... | 34 |
| 2.3.1 Reagents..... | 34 |
| 2.3.2 Coating of beads..... | 35 |
| 2.3.3 Preparation of beads..... | 35 |
| 2.3.4 Preparation of coating..... | 35 |
| 2.3.5 Coating process..... | 35 |
| 2.3.6 Assay..... | 36 |
| 2.4 Autophagy assay..... | 36 |
| 2.4.1 Reagents..... | 36 |
| 2.4.2 Assay..... | 36 |
| 2.5 Fluorescent microscopy..... | 37 |

| | | |
|--------|---|----|
| 2.6 | Western blotting..... | 37 |
| 2.6.1 | Reagents..... | 37 |
| 2.6.2 | Cell western blotting..... | 37 |
| 2.6.3 | Tissue western blotting..... | 38 |
| 2.7 | Growth rate measurements..... | 39 |
| 2.8 | Fertility assessment..... | 39 |
| 2.9 | Morphological analysis of different tissues..... | 39 |
| 2.10 | Tissue preservation and processing..... | 39 |
| 2.10.1 | Reagents..... | 39 |
| 2.10.2 | Process..... | 39 |
| 2.11 | Haematoxylin and Eosin (H & E) staining of tissue sections..... | 40 |
| 2.11.1 | Reagents..... | 40 |
| 2.11.2 | Process..... | 40 |
| 2.12 | Immunostaining of tissue sections..... | 41 |
| 2.12.1 | Reagents..... | 41 |
| 2.12.2 | Process..... | 41 |
| 2.13 | Liver enzyme assay..... | 42 |
| 2.13.1 | Reagents..... | 42 |
| 2.13.2 | Process..... | 42 |
| 2.14 | Gel filtration chromatography..... | 43 |
| 2.14.1 | Reagents..... | 43 |
| 2.14.2 | Process..... | 43 |
| 2.15 | Cytokine assay..... | 43 |
| 2.15.1 | Reagents..... | 43 |
| 2.15.2 | Standard preparation..... | 44 |
| 2.15.3 | Magnetic bead preparation..... | 44 |
| 2.15.4 | Detection antibody preparation..... | 44 |
| 2.15.5 | Assay..... | 44 |

Chapter 3

| | |
|---|----|
| Analysis of canonical and non-canonical autophagy in mice lacking WD domain of ATG16L1..... | 46 |
| 3.1 Generation of mice..... | 46 |
| 3.2 Mouse nomenclature..... | 49 |
| 3.3 Genotyping by PCR..... | 49 |
| 3.4 Analysis of expression of truncated ATG16L1 by western blot..... | 51 |
| 3.4.1 In Mouse embryonic fibroblasts (MEFs)..... | 51 |
| 3.4.2 In different mice tissues..... | 51 |
| 3.5 Analysis of canonical and non-canonical autophagy..... | 51 |
| 3.5.1 Status of autophagy and LAP in cells..... | 53 |
| 3.6 Summary..... | 55 |

Chapter 4

| | |
|--|----|
| Analysis of role of WD domain in tissue homeostasis..... | 56 |
| 4.1 Gross morphology, weight and fertility..... | 56 |
| 4.2 Liver..... | 56 |
| 4.3 Kidney..... | 62 |

| | |
|---|----|
| 4.4 Muscle..... | 64 |
| 4.5 Brain..... | 66 |
| 4.6 Summary & discussion..... | 68 |
| Chapter 5 | |
| Analysis of ATG16L1 complex formation in liver and brain..... | 69 |
| 5.1 Calibration of gel filtration column..... | 70 |
| 5.2 Analysis of liver lysates..... | 70 |
| 5.3 Analysis of brain lysates..... | 73 |
| 5.4 Discussion..... | 73 |
| Chapter 6 | |
| Cytokine analysis..... | 75 |
| Chapter 7 | |
| Discussion..... | 78 |
| References..... | 81 |

List of abbreviations:

AMBRA1 = Activating molecule in Beclin1-regulated autophagy protein 1

ATG = Autophagy-related

Atg16/1 = Autophagy-related 16-like 1 gene (mammalian)

atg16/1 = Autophagy-related 16-like 1 gene (mutated, mammalian)

ATG16L1 = Autophagy-related 16-like 1 protein

Atg16 = Autophagy-related 16 gene (in yeast)

BCA = Bicinchoninic acid

bp = Base pair

BSA = Bovine serum albumin

CALCOCO2 = Calcium-binding and coiled-coil domain-containing protein 2

CCD = Coiled-coil domain

Cre = Cre-recombinase

CTTN = Cortactin

DAPI = 4',6-diamidino-2-phenylindole

DFCP1 = zinc-finger FYVE domain-containing protein 1

DMEM = Dulbecco's modified Eagle medium

dNTP = Deoxyribonucleotide triphosphate

EPG5 = Ectopic P-granules autophagy protein 5 homolog

ER = Endoplasmic reticulum

ES cells = Embryonic stem cells

EDTA = Ethylenediaminetetraacetic acid

FBS = Fetal bovine serum

FIP200 = FAK-family interacting protein of 200

FL = Full length

GABARAP = γ -aminobutyric acid receptor- associated protein

H & E = Haematoxylin & eosin

HBSS = Hank's balanced salt solution

HCl = Hydrochloric acid

HOPS = Homotypic fusion and protein sorting

Hr = Hour

HRP = Horse radish peroxidase

IL = Interleukin

IFN = Interferon

KO = Knockout

k Da = kilo Dalton

LAP = LC3-associated phagocytosis

LC3 = Microtubule-associated protein light chain 3

LPS = Lipopolysaccharide

M-CSF = Murine colony stimulating factor

MEF = Mouse embryonic fibroblast

MHC = Major histocompatibility complex

MgCl₂ = Magnesium chloride

mTOR = Mammalian target of rapamycin

MYO = Myosin

NADPH = Nicotinamide adenine dinucleotide phosphate

NaCl = Sodium chloride

NaOH = Sodium hydroxide

NBR1 = Neighbour of BRCA1 gene 1

NDP52 = Nuclear dot protein 52

NH₄SO₄ = Ammonium sulphate

NOX2 = NADPH oxidase 2

OPTN = Optineurin

PAGE = Polyacrylamide gel electrophoresis

PAS = Phagophore assembly site

PBS = Phosphate buffered saline

PCR = Polymerase chain reaction

PE = Phosphatidylethanolamine

PHOX2 = Paired-like homeobox 2

PI3K = Phosphatidylinositol 3-kinase

PI3P = Phosphatidylinositol 3-phosphate

PINK1 = PTEN-induced kinase 1

PLEKHM1 = Pleckstrin Homology and RUN Domain Containing M1
PRKN = Parkin
PVDF = Polyvinylidene difluoride
RAB7 = Ras-related protein Rab-7
Rac1 = Ras-related C3 botulinum toxin substrate 1
ROS = Reactive oxygen species
Rubicon = RUN domain protein as Beclin-1interacting and cysteine-rich containing
SDS = Sodium dodecyl sulphate
SEM = Standard error of the mean
SNARE = SNAP receptor
SNAP29 = Soluble NSF (N-ethylmaleimide sensitive fusion protein) attachment Protein 29
SQSTM1 = Sequestosome 1
STX17 = Syntaxin 17
TAE = Tris-acetate-EDTA
Taq = Taq polymerase
TBK1 = TANK Binding Kinase 1
TBST = Tris-buffered saline with Tween
TECPR1 = Tectonin Beta-Propeller Repeat Containing 1
TLR = Toll-like receptor
TNF = Tumour necrosis factor
T-PER = Tissue protein extraction reagent
TRIM = tripartite motif family
Tris-HCl = Tris(hydroxymethyl)aminomethane-hydrochloride
ULK1 = Unc-51-like kinase 1
UPS = Ubiquitin proteasome system
UVRAG = UV radiation resistance-associated gene protein
VAMP8 = Vesicle-associated membrane protein 8
VPS34 = Vacuolar protein sorting 34
WD = Tryptophan-Aspartate
WIPI2 = WD repeat domain phosphoinositide-interacting protein 2
WT = Wild type

List of figures:

Figure 1: The process of autophagy

Figure 2: Similarity between ubiquitin-proteasome system (UPS) and autophagy

Figure 3: Cargo sequestration and selective autophagy

Figure 4: Fusion of autophagosome with lysosome

Figure 5: Difference between canonical and non-canonical autophagy/LAP

Figure 6: Non-canonical autophagy or LC3 associated phagocytosis (LAP)

Figure 7: Evolution of ATG16L1 WD domain

Figure 8: Key residues of CCD mediate WIPI2 binding

Figure 9: Deletion of WD domain of ATG16L1

Figure 10: Generation of mice deficient in WD domain

Figure 11: Genotyping of WD deficient mice

Figure 12: Role of WD domain in autophagy

Figure 13: Role of WD domain in autophagy and LAP

Figure 14: Phenotype of E230 and E226 mice

Figure 15: Role played by WD domain in maintaining liver homeostasis

Figure 16: Role of WD domain in preventing hepatomegaly and liver inflammation

Figure 17: Role of WD domain in maintaining kidney homeostasis

Figure 18: Role of WD domain in maintaining muscle homeostasis

Figure 19: Role of WD domain in maintaining brain homeostasis

Figure 20: Calibration of gel filtration column

Figure 21: Analysis of ATG16L1 complex in liver and brain

Figure 22: Role of WD domain on cytokine levels

List of tables:

Table 1: Genotyping PCR details

Table 2: Expected results of PCR and annotation of genotypes

Table 3: Hematoxylin-eosin staining procedure of formalin fixed paraffin embedded tissue sections

Acknowledgement

I would like to extend my sincere acknowledgements to my primary supervisor Prof Tom Wileman for all his guidance, encouragement and support throughout my PhD. Coming from a different country I consider myself extremely fortunate to get an opportunity to do a PhD under his supervision and I also acknowledge him for believing in me. Other than science I also learned a lot from him regarding oral and written communication skills.

I want to thanks Prof. Ulrike Mayer for guiding me through genotyping related issues and also for answering small doubts regarding mouse genetics. The quick discussions with her were always fruitful and informative.

I thank Dr. Naiara Beraza for training me in all the histological techniques which was used throughout my PhD. I appreciate the patience she showed towards me while training all the new techniques. The trouble shooting approaches I have learned from her are going to help me in my later career as well.

I would like to thank Dr. Monica Maizo Ferre for all the kind gestures she showed for me while I worked till late in Naira's lab at Quadram institute.

I would like to thanks all my current and previous lab mates for their kind support and help during my PhD. I thank Matt for being a mentor, a friend and a chatter box of lab to keep the lab environment happy. Although I have some experience of lab management from my past, the skills I learned from Matt are the ones I was missing. I thank Sophia for being a sweet lab mate and friend who is always approachable and helpful. I thank Weijiao for being a fantastic lab mate, a caring friend, buddy and a vast source of information. I admire the knowledge, experience and expertise he possess in his area of interest. I thank him for all the opportunities he gave me to experience and relish Chinese cuisines. I thank Ben for being a jolly and helpful lab mate. I thank Penny for all the guidance and support I received from her. I will miss all the together time I spend with Matt, Weijiao, Sophia and Ben during our movie and dinner outings.

I sincerely thank Dr. Timothy Pearson for all the tricks and methods he showed me to overcome day to day lab troubles. I acknowledge him for all his help for difficult western blot and initial key experiments of my project. I also acknowledge Dr. Julia Maryam Arasteh for making those transgenic mice which are the centre point of this thesis.

My PhD would not be possible without the encouragement and support of my friends in India: Sanjeev, Manoj, Mukesh and Arvind. Although they were far away but they never ceased to stay in touch in my good and bad times. I also want to thanks my local friends and house mates Radoslaw, Niccolo, Yanko, Victoria and Tomas for making my stay comfortable, joyful and a learning experience. I thank Abhishek and Sujith for all their practical advice for a smooth settle down in a culturally different country.

I can't thank enough to my parents Mr. Brahamanand Rai and Mrs. Prema Rai. It is because of their support I could achieve whatever I have till now and will later. I am and will be always grateful to them. I treasure all the support and guidance received by my elder brother Prashant regrading living and surviving in a foreign land.

Last but not least I thank my girlfriend turned fiancée turned wife, Deeti whose love and affection gave me stability and patience to continue my work. I thank her for all the sacrifices she has made for my PhD and wellbeing.

Chapter-1

Introduction

1. Autophagy:

Macroautophagy, hereafter referred as autophagy (Greek, auto = 'self', phagein = 'to eat') is a cellular recycling process that is conserved in eukaryotes from yeast to humans (1, 2) during which excess and damaged cytoplasmic materials (cargo) are captured in double membrane vesicles called autophagosomes which then fuse with lysosomes (autolysosomes) to degrade the cargo. The degradation products, which are mostly amino acids, get recycled in to cytoplasm to be utilised in metabolic pathways. The most common trigger of autophagy is amino acid starvation. Other than the induction of autophagy by starvations, cells can use low levels of constitutive or general autophagy to clear damaged organelles, proteins and aggregates to maintain tissue homeostasis. Hence, dysfunctional autophagy has been associated with various conditions like neurodegenerative disorders, cancer, ageing, inflammatory diseases etc (3). Autophagy is also involved in the removal of pathogens (xenophagy) and plays role in providing immune-protection (3).

1.1. The core components of autophagy.

To date more than 30 autophagy related (Atg) genes have been identified. These were first identified in yeast and many orthologs have been identified in higher eukaryotes. Autophagy can be viewed as a series of sequential steps (Figure 1A) involving signalling events that initiate autophagosome formation (phagophores nucleation), the expansion and closure of the autophagosome during cargo capture and fusion of the autophagosome with the lysosome (4).

1.1.1 Autophagosome Initiation (phagophore nucleation).

Initiation of autophagy is regulated by the mammalian/mechanistic target of rapamycin complex (mTOR). The mTOR kinase senses amino acid levels, and when amino acids levels are high, mTOR

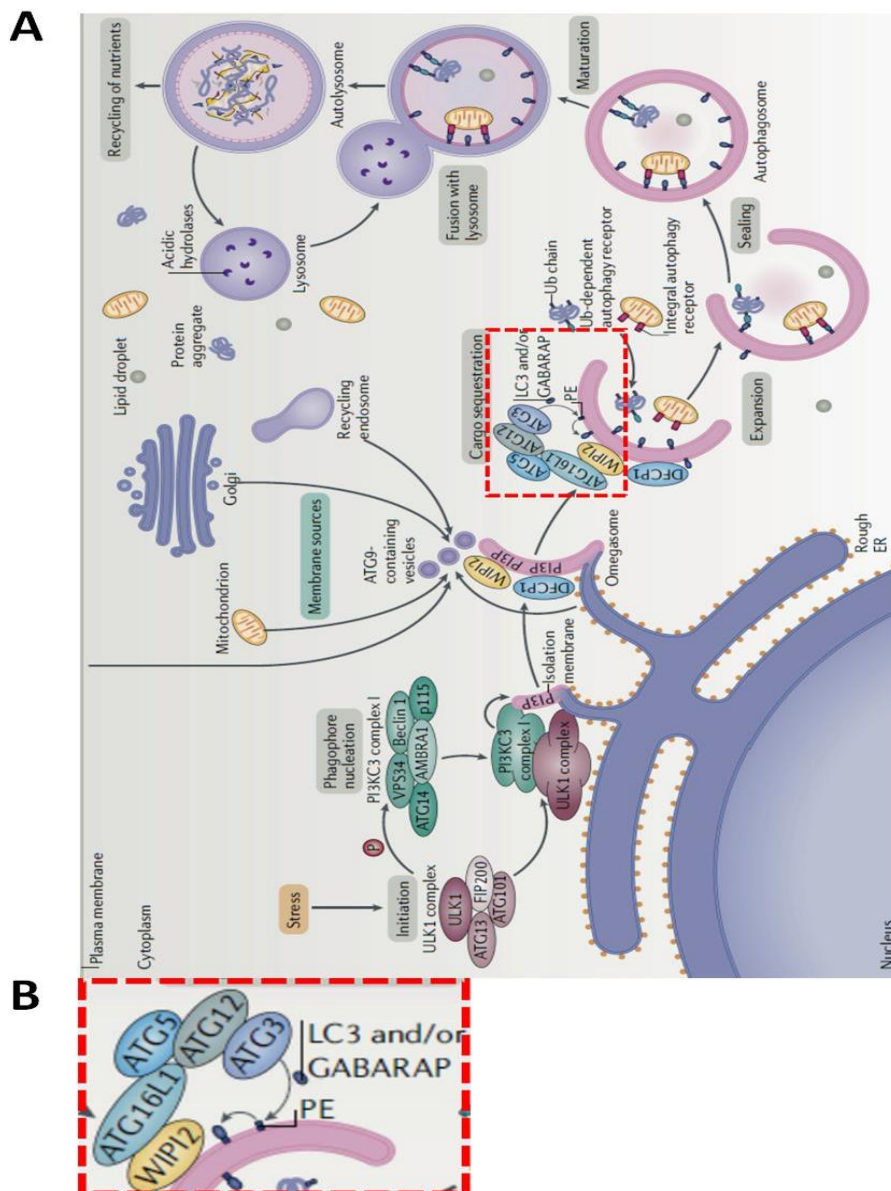


Figure 1: The process of autophagy: A. Starvation and other stress signals activate ULK1 complex (ULK1, ATG13, FIP200 & ATG101) (initiation) to phosphorylate and recruit components of class III PI3P kinase complex I (VPS34, Beclin 1, ATG14, AMBRA 1 and p115) on to isolation membrane at PAS (phagophore assembly site) region of endoplasmic reticulum (ER) (phagophore nucleation). PI3P kinase complex generated PI3P recruit further proteins like DFCP1 and WIPI2 on expanding phagophore at omegasomes (phagophore expansion). Various cellular sources provide membrane during phagophore expansion. WIPI2 recruits ATG3 via ATG12-ATG5-ATG16L1 complex to mediate LC3 conjugation to membrane associated PE. WIPI2 interaction with ATG16L1 is essential for this process (highlighted in B). The cargo sequestration within growing double membrane of phagophore is performed by the help of various mechanisms involving tag proteins like ubiquitin (ub) or cargo receptor protein binding cargo/ tag and PE conjugated LC3. Once completely formed the double membraned phagophore, called autophagosome, fuses with lysosome to mature in autolysosome. Cargo in autolysosome gets degraded by acidic hydrolases present in the lumen and the degradation products get recycled in the cytoplasm. **B.** ATG16L1 interacts with WIPI2 on membrane to bring ATG3 through ATG12-ATG5-ATG16L1 complex interaction. Figure taken from (4).

phosphorylates proteins required for m-RNA translation to increase protein synthesis. At the same time active mTOR phosphorylates and inhibits the ULK1 complex required for autophagy. The ULK1 complex contains ULK1/2, ATG13 and FIP200 and inactivation of mTOR during starvation leads to dissociation from mTOR and activation of the ULK1/2 kinase which phosphorylates ATG13 and FIP200 to initiate autophagosome formation which begins at specific area on endoplasmic reticulum (ER) called omegasomes that are PI3P rich and marked by PI3P-binding protein zinc-finger FYVE domain-containing protein 1 (DFCP1 also known as ZFYVE1) (Figure 1A). Nascent autophagosomes are termed as phagophores and area of phagophore nucleation are referred as phagophores assembly site (PAS). Other than ER, ER-mitochondria contact sites, ER-plasma membrane contact sites (5, 6) as well as organelles like golgi complex, plasma membrane and recycling endosomes were also recently implicated as PAS (7) (Figure 1A).

1.1. 2 Phagophore expansion. The activated Unc-51-like kinase 1 (ULK1) complex (consisting of ULK1, autophagy-related protein 13 (ATG13), RB1-inducible coiled-coil protein 1 (FIP200) and ATG101) formed in response to low amino acids recruits the Class III PI3 kinase complex (consisting of class III PI3K, vacuolar protein sorting 34 (VPS34), Beclin1, ATG14, activating molecule in Beclin1-regulated autophagy protein 1 (AMBRA1) and general vesicular transport factor (p115)) to membranes that will initiate autophagosome expansion during autophagosome formation (Figure 1). Most autophagosomes are thought to originate from the endoplasmic reticulum (ER) but mitochondria, plasma membrane, recycling endosomes, Golgi complex and ATG9 containing vesicles have also been implicated as membrane source provider during expansion of phagophores (Figure 1A). The PI3 kinase activity of Vps34 kinase phosphorylates inositol lipids to generate local phosphatidylinositol-3-phosphate (PI3P) at particular structure of ER called Omegasome (Figure 1A). These PI3Ps provide a signal for autophagy proteins WD repeat domain phosphoinositide-interacting protein 2 (WIPI2) and zinc-finger FYVE domain-containing protein 1 (DFCP1) required for autophagosome expansion (Figure 1A & B). These proteins carry FYVE domains that bind phosphorylated inositols generated by Vps34. The most important is WIPI2 which recruits

downstream autophagy proteins ATG5, ATG12 and ATG16L1 that facilitate incorporation of LC3 into the limiting membrane of the autophagosome. WIPI2 binds directly to ATG16L1 and in this way brings ATG16L1 to membranes phosphorylated by Vps34 (Figures 1B).

The conjugation of LC3 to the PE of growing phagophore membrane follows the same pattern as ubiquitin proteasome system (UPS) for the tagging and degradation of proteins (8). UPS involves E1, E2 and E3 enzymes for activation, conjugation and ligation steps, respectively, for coupling of proteins to ubiquitin required for degradation (8) (Figure 2A). The LC3 conjugation is preceded by cysteine protease ATG4 mediated processing of C-terminal of LC3 to expose glycine residue essential for the process (Figure 2B). This processed form of LC3 gets activated by E1-like enzyme ATG7 before its conjugation to membrane associated PE by the activity of ATG3 (Figure 2B). In this process a cytoplasmic free form of LC3 (LC3-I) gets converted in to membrane anchored form of LC3 (LC3-II) (Figure 2B). The E1 like enzyme ATG7 also activates ATG12 to form ATG5–ATG12 conjugate with the help of E2 like enzyme ATG10 (Figure 2C). The E3 like enzyme activity of ATG5–ATG12 conjugate stimulates ATG3 for conjugation of LC3 to membrane associated PE (Figure 2C). The ATG5–ATG12 conjugate associates with ATG16L1 to form a complex which eventually localises to phagophore's membrane due to interaction between ATG16L1 and WIPI2 (Figures 1B). This conjugation system works similarly for all the ATG8 family proteins like LC3 and γ -aminobutyric acid receptor- associated proteins (GABARAPs). Different isoforms of ATG4 operate on the processing of ATG8 family proteins. Processing of LC3 is done by ATG4B whereas GABARAPs are processed by ATG4A. This conjugation process facilitates phagophores expansion and possibly closure as well.

The cysteine protease ATG4 also plays role in limiting phagophores expansion by de-conjugating LC3 from its membrane. This way LC3 gets recycled in the next expansion step. This critical two-way activity (LC3 processing and de-conjugation) of ATG4 is tightly regulated by methods like mitochondria generated ROS or de-phosphorylation by ULK-1 (9-11).

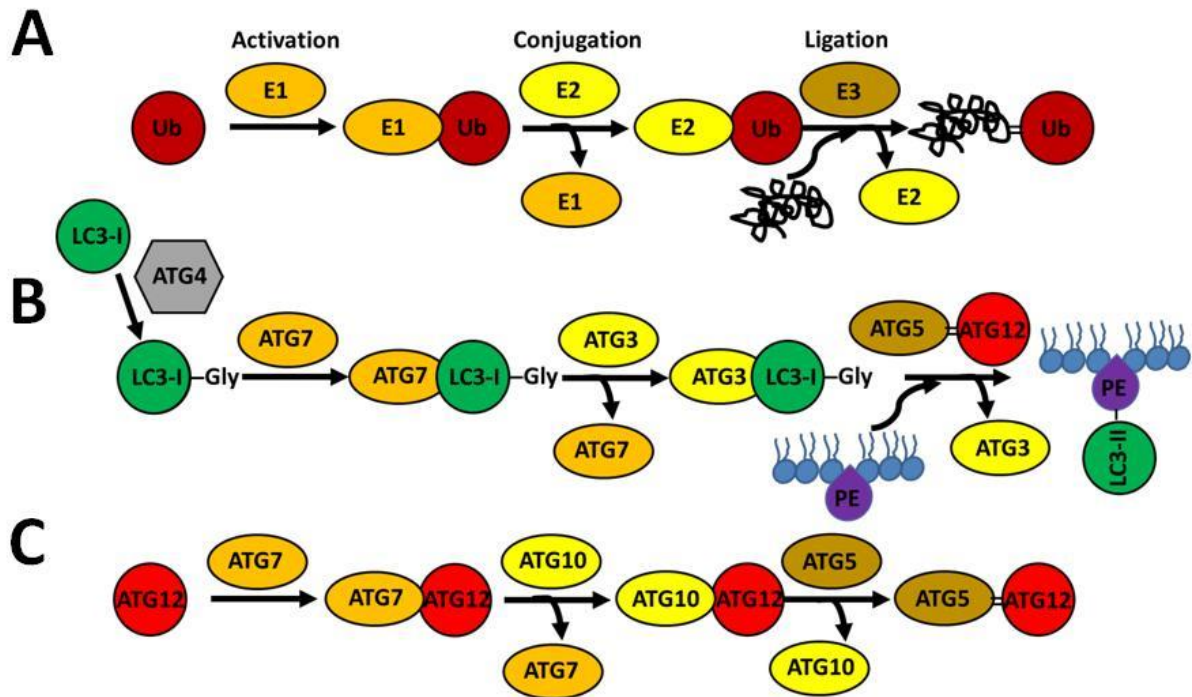


Figure 2: Similarity between ubiquitin-proteasome system (UPS) and autophagy: Short half-life proteins in cells get marked with ubiquitin (Ub) to be directed for degradation. This conjugation process involves three sequential steps in which Ub gets finally conjugated to the target protein as marker for degradation. **A.** The three steps are mediated by E1, E2 and E3 enzymes for activation, conjugation and final ligation of Ub to the protein to be degraded, sequentially. LC3 conjugation to existing membrane of phagosomes, endolysosomes or autophagosomes happens in similar way where different proteins show E1, E2 or E3 like activity. **B.** The ATG4 mediated activation of LC3 initiates sequential activities of E1 like ATG7, E2 like ATG3 and finally E3 like ATG12–ATG5 conjugate to transfer LC3 to membrane associated PE. **C.** E3 like ATG12–ATG5 conjugate is created by similar sequential activities of E1 and E2 like ATG7 and ATG10 respectively, on ATG12 to make a covalent conjugation with ATG5 required for final step of LC3 conjugation to PE on membrane. Figure modified from (8).

1.1.3 Cargo sequestration.

The membrane conjugated LC3 has more roles than just phagophores expansion. All the ATG8 family proteins like LC3 bind with a specific motif (W/F/Y₁X₂X₃L/I/V₄) present on other proteins called LC3 interacting regions (LIRs). Various cargo receptor proteins (also called adapter proteins) like sequestosome 1 (p62/SQSTM1), B-box coiled coil motif containing neighbour of BRCA1 gene 1 protein (NBR1) and nuclear dot protein 52 (NDP52) also known as calcium-binding and coiled-coil domain-containing protein 2 (CALCOCO2) bind to the cargo at one and LC3-II to another end acting like a bridge to help in cargo capturing (Figures 1A& 3). Often these cargo receptors bind to “eat me” signals (e.g. ubiquitin or galectins) displayed on the cargo surface to form the bridge (Figures 1A & 3). This process of capturing “earmarked” cargo for autophagic degradation is termed as selective autophagy which is different from the starvation induced “bulk autophagy” which is also known as general autophagy.

Selective autophagy is named differently for every cargo it chooses to degrade by suffixing with the initials of the target cargo’s name e.g. mitophagy (for mitochondria), aggrephagy (protein aggregates), xenophagy (intracellular pathogens), ribophagy (ribosomes), ERphagy (ER), pexophagy (peroxisomes), lipophagy (lipid droplets), nucleophagy (part of nucleus) and likewise. The process of selectively capturing specific cargo follows different mechanisms employing various proteins based on the choice of cargo (Figure 3) (12). In most known cases the selected cargo either directly binds to membrane anchored LC3-II via its own LIR motif or first gets labelled with a tag like ubiquitin which bind to a receptor protein that finally binds to LC3-II (Figure 3) (12). These receptor proteins carry both a LIR motif and an ubiquitin-binding domain hence acting as a bridge between cargo and LC3-II. In case of cargo comprising components of inflammasome or IFN signalling, TRIM family receptor proteins, bridge the gap between cargo and GABARAP without ubiquitin tagging (13) (Figure 3). The process of selective autophagy has more physiological relevance than bulk autophagy which is more like a homeostasis mechanism. A tight regulation of the selective autophagy must be necessary as an

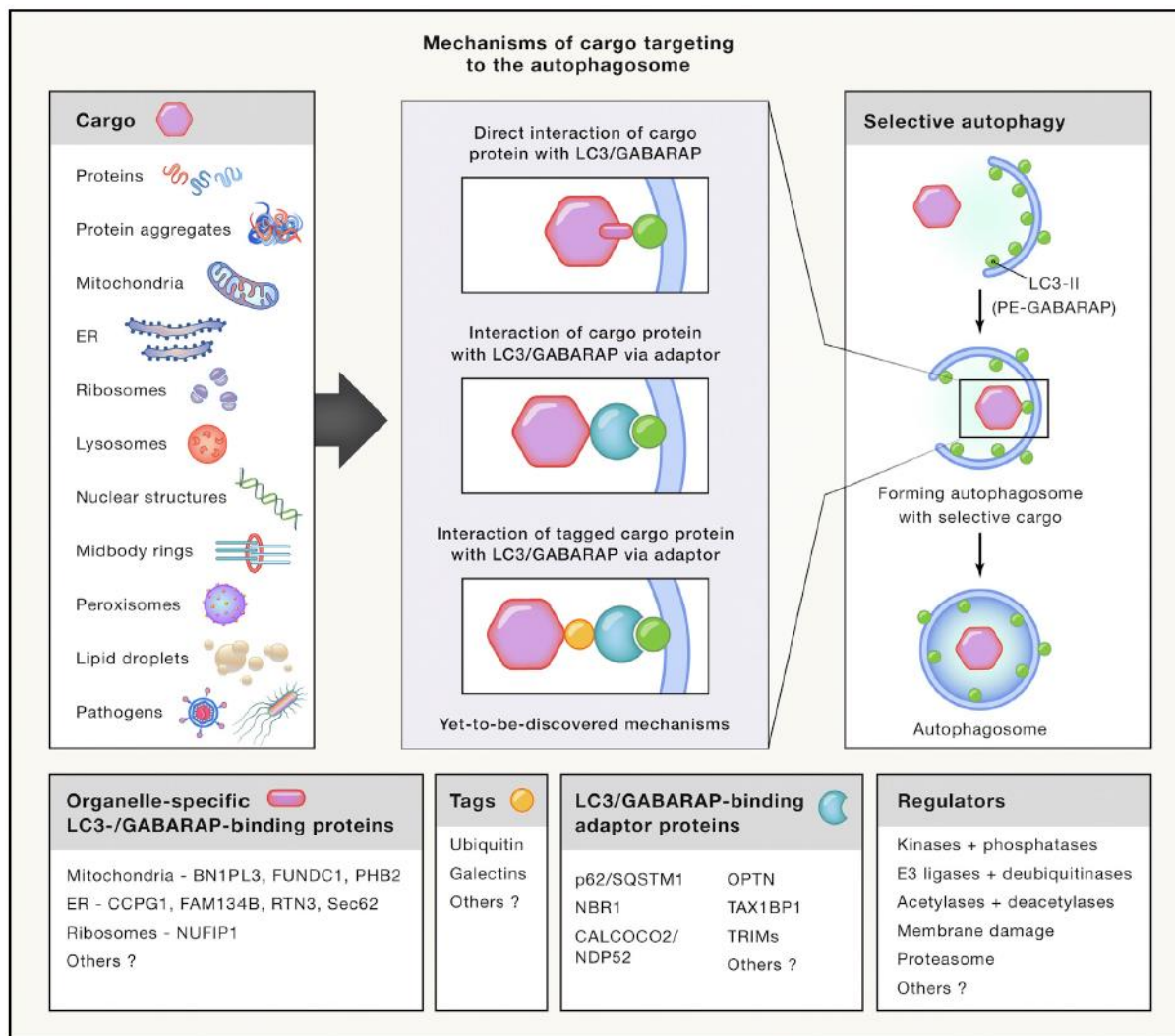


Figure 3: Cargo sequestration and selective autophagy: The figure shows various cargoes directed for degradation via autophagy, get sequestered in the autophagosome by various mechanisms. Different cargoes interact with membrane conjugated LC3/GABARAP for the sequestration process. Depending on cargo, this interaction can happen directly between cargo and LC3/ GABARAP or it can get facilitated by intermediate interaction with adaptor/receptor (p62/SQSTM1, NBR1, NDP52, OPTN etc.) proteins and/or tags (ubiquitin, galectin etc.). The involvement of additional tag and adaptor proteins make this process selective for specific cargoes and hence it is termed as selective autophagy which is different from non-specific or bulk autophagy. The figure also shows a non-exhaustive list of known organelle specific LC3/ GABARAP binding proteins, Tags, adapter proteins and regulators. Figure taken from (12).

inappropriate display in space and time of any of the selectivity factor can lead to disturbed homeostasis. Mutation in various selective autophagy factors like receptor proteins has been associated with diseases like neurodegenerative disorders (p62/SQSTM1, optineurin/OPTN (14-17)), parkin/PRKN (18-20), PINK1 (21), TBK1 (22, 23)), inflammatory bowel disease (NDP52/ CALCOCO2) (24) and autoimmunity disorder (TRIM20) (25) etc.

1.1.4 Autophagosome fusion with lysosomes:

After closure, fully formed autophagosomes go through the process of maturation which starts with the stripping of all the proteins involved in phagophore expansion. The fusion of autophagosomes to lysosomes requires close positioning of both the structures which starts with the perinuclear clustering of lysosomes driven by intracellular pH change (26). Once completely formed, autophagosomes move towards perinuclear region by the help of motor protein dynein and kinesin which propels its centripetal movement along microtubule (27, 28) (Figure 4). Besides microtubule-based motors, actin-based motors MYO6/ myosin VI and MYO1/myosin I also participate in this process (28-30) (Figure 4). Once they are in close proximity, for efficient fusion, autophagosomes gets tethered to lysosomes through various factors. These factors broadly fall in three categories: HOPS (homotypic fusion and protein sorting) complex, RAB7 and adaptors (EPG5, PLEKHM1, TECPR1) that link autophagosomal and lysosomal components to the core tethering or fusion machinery (Figure 4) (28).

The core tethering factor for autophagosome-lysosome fusion, the HPOS complex interacts with Q-SNARE STX17 to form a trans SNARE complex needed for fusion (28, 31, 32) (Figure 4). The fusion process is further aided by specificity provided by RAB7 and adaptors. The adaptors EPG5 binds to RAB7 present on the lysosomes and LC3-II of autophagosome providing specificity to the fusion process (Figure 4)(28). Similarly, the adaptor PLEKHM1 bridges the gap between autophagosome and lysosome by binding to HOPS complex, LC3-II and RAB7 of lysosome (Figure 4)(28). Another

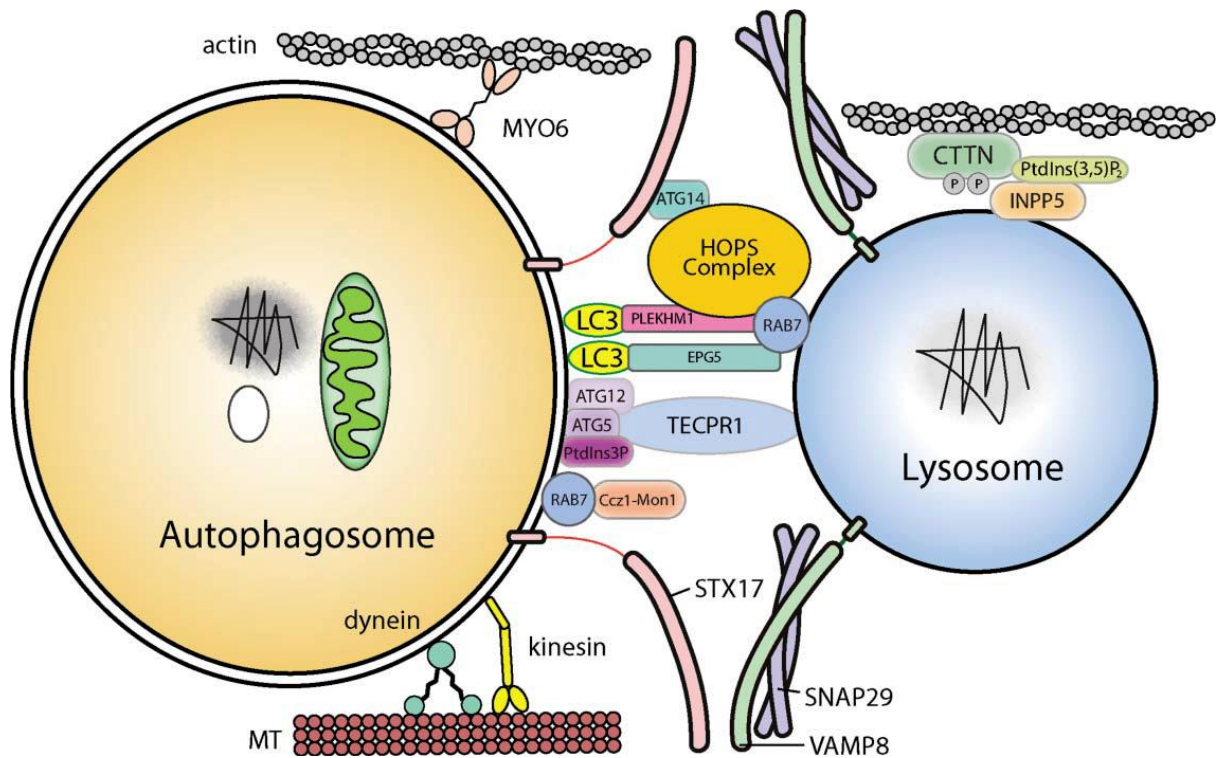


Figure 4: Fusion of autophagosome with lysosome: Autophagosome move closer to lysosomes with the help of microtubule based motor proteins dynein, kinesin and actin based motor protein myosin (MYO6). Once placed in close proximity, the autophagosomes get tethered to lysosomes with the help of HOPS complex, RAB7 and adaptors PLEKHM1, EPG5 and TECPR1. Adaptors provide specificity to the fusion process by binding directly or to different factors associated with autophagosomal (LC3, ATG12–ATG5) or lysosomal (RAB7) membranes. The final fusion process is mediated by fusion of SNARES on autophagosomes (STX17) and lysosomes (VAMP8, SNAP29) to form a trans-SNARE complex. Interaction of lipid molecules with various factors like Ptdins3P-TECHPR1 and CTTN (cortactin)-Ptdins(3,5)P₂-CTTN, helps in the stabilisation of fusion complex. Figure taken from (28).

adaptor TECPR1 binds directly to the lysosome but via ATG12–ATG5 and PtdIns3P to autophagosome (28, 33) (Figure 4).

SNAREs are the core components of the fusion machinery. During membrane fusion R-SNAREs and Q-SNAREs on separate membranes assemble on to trans-SNARE complexes to provide necessary force for fusion. During autophagy autophagosomal Q-SNARE STX17 interacts with SNAP29 and the lysosomal R-SNARE VAMP8 to form a trans-SNARE complex to facilitate fusion (28, 34) (Figure 4).

Many factors regulate the SNARE complex of autophagosome. ATG14 interacts with STX17 to stabilise the binary Q-SNARE complex STX17-SNAP29 on autophagosomes to promote fusion (28, 35) (Figure 4).

Apart from all the above mentioned cytoskeletal elements, motor proteins, tethering factors, adaptor proteins and SNAREs, the membrane lipid molecule phosphatidylinositol (PI) also plays a key role in autophagosome-lysosome fusion. Among its seven different forms (phosphorylated and dephosphorylated), PtdIns3P, PtdIns4P and PtdIns(3,5)P₂ are required for autophagosome-lysosome fusion (33, 36-39). INPP5 of lysosome dephosphorylates PtdIns(3,5)P₂ to induce CTTN (cortactin) dependent actin filament stabilisation on lysosome, promoting autophagosome-lysosome fusion (Figure 4) (28). As mentioned earlier, PtdIns3P also plays an important role in the fusion process by binding to TECPR1 assisted by its interaction with ATG12–ATG5 (28, 33) (Figure 4).

At the end of this step, the outer membrane of autophagosome fuses with the membrane of lysosome and the single membraned vesicle gets delivered in to the lumen of autolysosome (fusion product of autophagosome and lysosome). In the lumen, the inner membrane of autophagosome gets digested by the action of lysosomal hydrolases and exposes the cargo for further degradation (40-42). At the end of cargo degradation, the generated products mainly amino acids and sugars gets transported out of autolysosome through lysosome efflux transporters leading to concomitant decrease in the volume of autolysosome. Autolysosomes are not permanent structure and

disintegrate at the end autophagy via a process dubbed as autophagic lysosome reformation (ALR) (43).

1.2 Non-canonical autophagy and LC3-associated phagocytosis (LAP):

Non-canonical autophagy and LC3-associated phagocytosis (LAP) uses the ubiquitin-like reactions of the ATG12–ATG5-ATG16L1 complex to conjugate LC3 to phosphatidylethanolamine (PE or PtdIn) in membranes of existing endolysosomes or endocytic vesicles containing extracellular or particulate materials to facilitate fusion with lysosomes (Figure 5A). This process is termed as LC3-associated phagocytosis (LAP) in phagocytic cells (e.g. macrophages, dendritic cells) where it leads to rapid removal of pathogens to modulate immune response (44-49). During canonical autophagy described above activation of the ULK1 complex (ULK1-ATG13-ATG101-FIP200) and class III PI3K complex leads to conjugation of LC3 to PE in cup-shaped phagophores that expands and seals engulfing cargoes within double-membraned autophagosomes (Figures 1A & 5B). During non-canonical autophagy, activation of the class III PI3K complex like UVRAG complex containing RUBICON, takes place without the aid of ULK1 complex leading to LC3-PE conjugation on pre-existing single membraned compartments that are not autophagosomes (Figures 5B & 6) (50).

1.2.1 LC3-associated phagocytosis (LAP): LAP is activated by TLR signalling following recognition of pathogens encased inside phagosomes and subsequent activation of class III PI3K complex (Figure 6). This class III complex contains beclin1, VPS34, UVRAG and Rubicon (Figure 6) (50). Recruitment of this complex on phagosomal membrane activates PtdIns3P production required for further recruitment of NADPH oxidase/NOX2 complex (Figure 6) (50). The NOX2 complex assembly forms when intraphagosomal components (NOX2 and p22 PHOX2) are joined by cytosolic NOX2 components (Rac1, p40 PHOX, p47 PHOX and p67 PHOX) (Figure 6) (50). The NOX2 assembly gets further stabilised by association with Rubicon (Figure 6). The stabilised NOX2 complex generates reactive oxygen species (ROS) which along with PtdIns3P recruit further downstream factors, same as required for autophagy (ATG7, ATG3, ATG12–ATG5-ATG16L1), for LC3 conjugation on the limiting

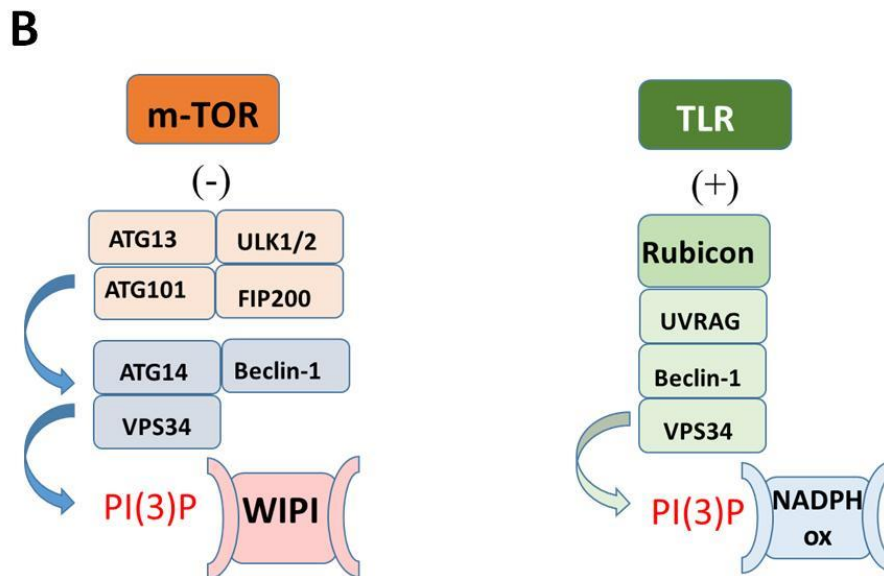
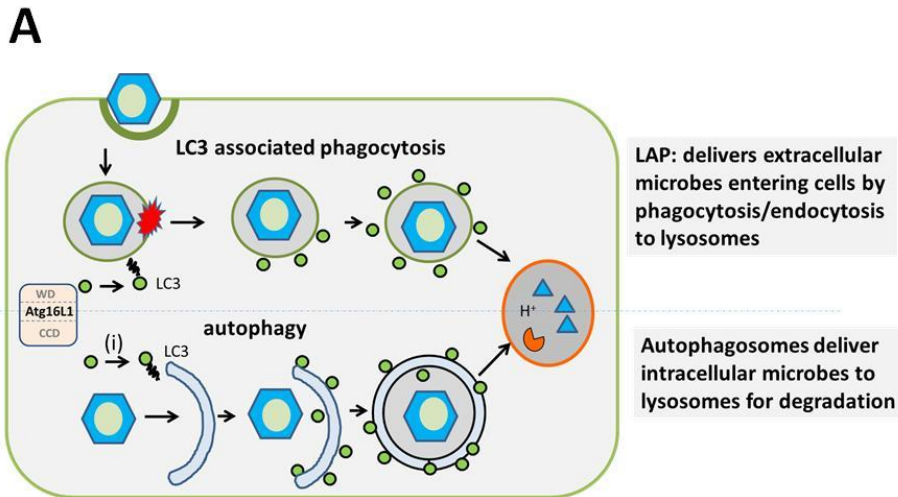


Figure 5: Difference between canonical and non-canonical autophagy/LAP: Autophagy and LAP both require membrane conjugation of LC3 via ATG16L1 to facilitate fusion with lysosomes. These processes slightly differ in their cargo selection and signalling events. **A.** LAP captures extracellular cargo (e.g. pathogen) in single membrane phagosome followed by LC3 lipidation on phagosome membrane. During autophagy intracellular cargos are captured in double membrane autophagosomes which gets LC3 conjugated on both outer and inner membranes. **B.** Autophagy and LAP differ in their initial signalling events. During autophagy, inhibition of mTOR during starvation recruits UKL-1 (ATG13, ULK1, ATG101, FIP200) and class III PI3K (ATG14, Beclin 1, VPS 34) complexes to generate local PI3P pool on membranes required for WIPI interaction. On the other hand, LAP is positively regulated by TLR mediated signalling to recruit UVRAG complex (Beclin 1, UVRAG, VPS34 and RUBICON) and NOX2 (NADPH oxidase 2) complex to generate PI3P and reactive oxygen species (ROS).

membrane of phagosomes (Figure 6) (50). This conjugation facilitates fusion of pathogen containing phagosomes with lysosomes for degradation and antigen presentation (Figure 6).

1.2.2 Non-canonical autophagy: During non-canonical autophagy, LC3 is recruited to endo-lysosomal compartments in non-phagocytic cells during micropinocytosis, engulfment of neighbouring cells by entosis, lysosomotropic drug treatment and during the uptake of particulate material or apoptotic cells (47, 48, 51).

1.2.3 Distinguishing between roles of autophagy and LAP:

Various in vitro studies showed that mammalian cells evolved two similar pathways namely autophagy and LAP for pathogen removal (50, 52-56) and hence to maintain tissue homeostasis by reducing tissue damage, the relative importance of one over other is not known. Since both the processes are very similar and most of the genes involved are same, it is difficult to find out which process has more importance in vivo. To address this problem a common strategy would be to generate in vivo models deficient in either autophagy or LAP. Mice carrying complete knock out of proteins essential for autophagy die soon after birth as they cannot survive the starvation generated after loss of placental nutrition (57). The role played by autophagy 'in vivo', therefore, has been studied using tissue specific knock out of autophagy genes (57-61). Many tissue specific autophagy deficient mice survive the post-natal period but show multiple tissue abnormalities including accumulation of ubiquitin positive inclusions containing protein aggregates and high level of inflammation and tissue damage (57-61). Most of these tissue-specific knockout mice were generated by targeted loss of *Atg3*, *Atg5*, *Atg7*, *Atg12* or *Atg16L1* which are autophagy proteins that are also required for LAP (57-61). These studies, hence could not determine whether the tissue abnormalities were seen because of absence of autophagy or LAP or both. During the course of this PhD, in another study, LAP-deficient mice have been generated by deleting Rubicon/RUBCN to

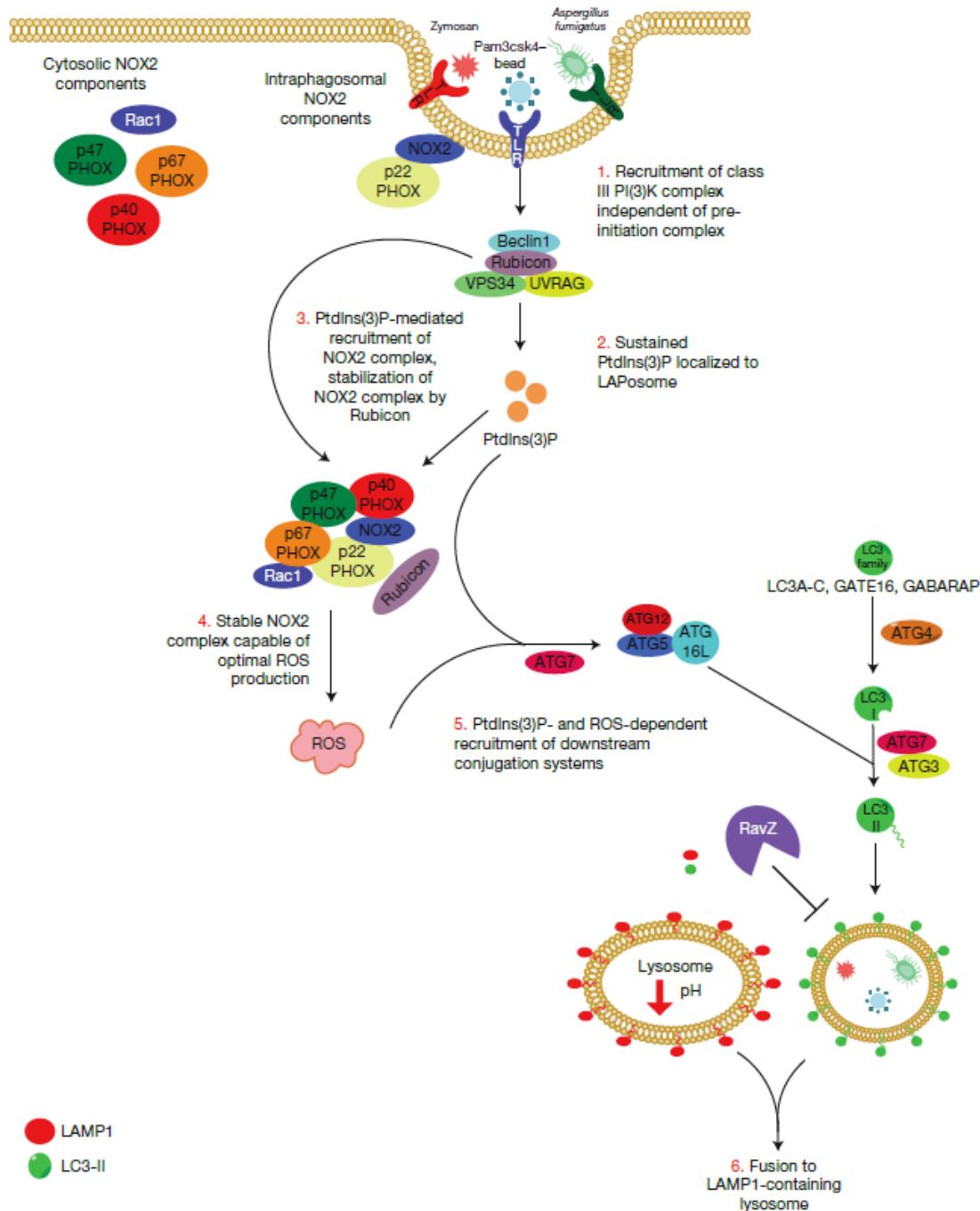


Figure 6: Non-canonical autophagy or LC3 associated phagocytosis (LAP): Various extracellular particulate materials or pathogens bind to specific toll like receptors (TLRs) to activate the signalling which involves recruitment of class III PI3K complex containing Beclin 1, RUBICON, VPS34 and UVRAG. This UVRAG complex generates local pool of PI3P (Ptdins3P) which helps in the recruitment of cytoplasmic RAC1, p40 PHOX, p47 PHOX and p67 PHOX on to phagosome/endosome associated NOX2 and p22 PHOX to form NOX2 complex stabilised by RUBICON. The stable NOX2 complex produces reactive oxygen species (ROS) which along with PI3P, generated by activated UVRAG complex, recruit downstream LC3 conjugation system involving ATG7, ATG12–ATG5–ATG16L1. Once conjugated with LC3, phagosomes/ endosomes fuse with LAMP positive lysosomes for cargo degradation. Figure taken from (50).

inactivate the UVRAG complex which conjugates LC3 to PE in pre-existing single membraned compartments (62). In these mice, the ULK1 complex (ULK1-ATG13-ATG101-FIP200) functions normally allowing them to activate autophagy. When challenged with apoptotic cells, RUBCN^{-/-} mice showed active engulfment but defect in clearance of dying apoptotic cells which is consistent with the previously reported in vitro study (47, 62). As a result to this, high serum levels of pro-inflammatory cytokines but not anti-inflammatory interleukin 10 (IL10) were detected supporting earlier in vitro data (47, 62). Similar observation was made when spontaneous serum levels of pro-inflammatory cytokines and IL10 was analysed in aged (52 weeks) LAP^{-/-} (*rubcn*^{-/-}, *nox2*^{-/-}) mice (62). Upon multiple injection of dying cells for over a period of 8 weeks, these mice (starting age 6 weeks) showed high levels of anti-nuclear antibodies and anti-dsDNA autoantibodies (62). These animals also displayed IgG and C1q deposition in the kidney glomeruli closely resembling to an autoimmune disease called systemic lupus erythematosus (SLE) (62). One problem for using the *rubcn*^{-/-} mouse for infection studies is that Rubicon has functions outside its role during LAP. Rubicon binds NOX2, p22PHOX and facilitates ROS production and also modulates pro-inflammatory cytokine signalling via NFkB. Defects in pathogen handling 'in vivo' may therefore arise because of altered ROS production and cytokine signalling rather than defects in phagocytosis and fusion with lysosomes (63-65).

Overall these results suggested the possible roles of LAP in removal of pathogens, clearance of dead cells, suppression of pro-inflammatory cytokines and production of anti-inflammatory interleukin 10 (IL10) in myeloid cells but could not reveal if the same holds true in non-myeloid cells. Therefore, an in vivo model with systemic loss of LAP, but intact autophagy, is required to address this question.

1.3 The WD domain of ATG16L1 is required for non-canonical autophagy.

ATG16L1 is a mammalian ortholog of the yeast Atg16 protein. In yeast, the protein is made up of two domains: N-terminal ATG5 binding domain and a C-terminal coiled coil domain (CCD) (Figure 7A).

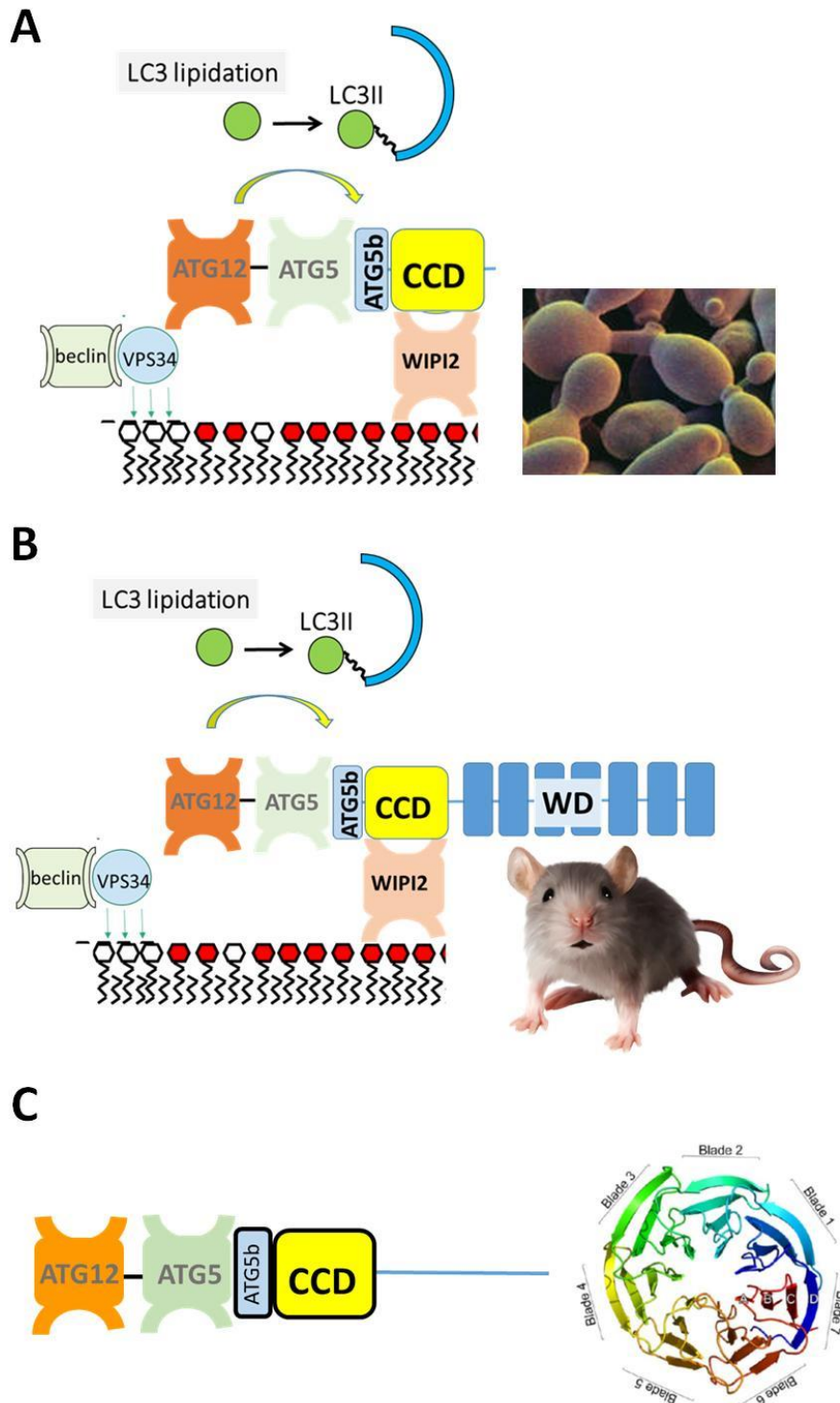


Figure 7: Evolution of ATG16L1 WD domain: **A.** ATG16 of the lower eukaryote yeast doesn't have a WD domain but does have an ATG5 binding domain and coiled coil domain (CCD) sufficient to activate autophagy. The remaining signalling in yeast is same as higher eukaryotes where VPS34 mediated PI3P generation facilitates WIPI2 binding which interacts with CCD of ATG16L1. **B.** Higher eukaryotes like mammals evolved a WD domain at the C terminus of ATG16L1. **C.** The WD domain forms a circular 7 bladed β barrel like structure (66).

As the name suggests, the N terminal domain binds ATG5 which is coupled covalently to ATG12 (Figure 7A). The C terminal CCD interacts with WIPI2 which brings the ATG12–ATG5–ATG16 complex close to membranes of autophagosomes allowing LC3 conjugation to PE (Figures 7A). CCD also participates in the homo-oligomerisation of ATG16L1 which aids in complex formation. Higher eukaryotes have evolved an additional N-terminal stretch of 40 tryptophan-aspartic acid repeats called the WD repeat domain which is joined to the CCD via a short linker region (Figure 7B). Crystallisation studies have shown that the 7 WD repeat domains are folded together to form a circular β propeller (Figure 7C) (66). The shorter version of Atg16 in yeast forms an active Atg12–Atg5–Atg16 complex which is sufficient for autophagy (Figure 7A). Similarly, expression of the N-terminal ATG5 binding and coiled coil domains of ATG16L1 in *atg16L1*^{-/-} mammalian cells reconstitutes autophagy (67). Although WD domain constitutes a significant portion of ATG16L1 protein, its cellular role remained uncertain for a long time. A recent collaboration between our lab and Oliver Florey at the Babraham Institute, Cambridge, UK showed that WD domain is required for non-canonical autophagy like pathway/LAP (67).

This study by Fletcher et al was conducted by reconstitution of various domain combinations of ATG16L1, in vitro, to find out the role of WD domain. Full length (FL), Δ FBD (missing 219-242 residues required for WIPI2 and FIP200 binding) and Δ WD (missing WD domain) versions of ATG16L1 were expressed in various *atg16L1*^{-/-} cell lines which restored canonical autophagy in cells with FL and Δ WD ATG16L1 (67). Monensin is an ionophore which induces LC3-II formation by raising lysosomal pH causing blockage of canonical autophagy flux. Monensin also causes osmotic imbalance of endolysosomal compartments targeting them for non-canonical LC3 lipidation. Monensin induced LC3 lipidation on membranes of endolysosomes, phagosomes with apoptotic corpse and LAMP1-positive bead containing phagosomes was found intact in cells with FL or Δ FBD versions but not in Δ WD ATG16L1 expressing cells. Further experiments using agents inducing non-canonical LC3 lipidation like NH₄Cl and *Helicobacter pylori* secreted virulence factor VacA showed similar results. Further analysis of FL or Δ WD ATG16L1 immunoprecipitates from cells, via western blotting and

mass spectrometry confirmed the presence of ATG12–ATG5–ATG16L1 complex. Point mutation based experiments demonstrated F467 and K490 as key residues of WD domain required for non-canonical LC3 recruitment. Expression of only WD domain in *atg16L1*^{-/-} cell lines didn't recover canonical autophagy or non-canonical LC3 conjugation on membranes confirming that WD domain is required but not sufficient for non-canonical LC3 lipidation on membranes. In further set of experiments this study showed more physiologically relevant evidence where lack of WD domain lead to defect in E- α peptide (an exogenous antigen) mediated antigen presentation on MHC class II molecules of macrophages and dendritic cells. In later experiments, the Δ WD cells failed to activate LC3-II formation following influenza-A infection. Overall, it was shown for the first time that WD domain of ATG16L1 is essential to activate non-canonical LC3 lipidation but dispensable for canonical autophagy (67).

1.4 Rationale for deleting WD domain in mice: Deletion of the WD domain of ATG16L1 can be used to generate mice deficient in non-canonical autophagy/LAP. Maryam Arasteh, a PhD student in the lab had introduced stop codons into the *Atg16l1* gene (Maryam Arasteh, PhD thesis, 2012) to engineer mice expressing ATG16L1 lacking the WD domain (delta WD mice) (Figure 8A-D). These mice were designed by taking account of the amino acids required in the CCD of ATG16L1 to bind WIPI2 (Figure 8A-D-C) (42). Two consecutive stop codons were inserted after CCD to terminate the translation of linker region and WD domain but preserve glutamate residues at 226 and 230 positions in CCD that are required for WIPI2 binding (Figure 9A-D). These mice are described in more detail in chapter 3.

Homeostasis is the property of cells, tissues and organisms to maintain a constant and continuous levels of various essential biochemical and physiological processes against different environmental stimuli like change in nutrients, invasion of pathogens etc. As LAP is a part of innate immune pathway to protect different tissues against pathogen infection and hence contributing in keeping up homeostasis, this thesis describes the characterisation of delta WD mice to determine if they can

maintain tissue homeostasis in absence of non-canonical autophagy/LAP. If they can, these mice will provide a novel model for studying the role played by non-canonical autophagy during infection 'in vivo'.

1.5 Specific aims: The specific aims of study presented in this thesis are:

1. To investigate the expression of WD deficient version of ATG16L1 protein in cells and tissues of E230 and E226 mice

2. To investigate the activity status of autophagy and LAP in cells and tissue of E230 and E226 mice

3. To analyse the status of homeostasis in various non-immune tissues of E230 and E226 mice

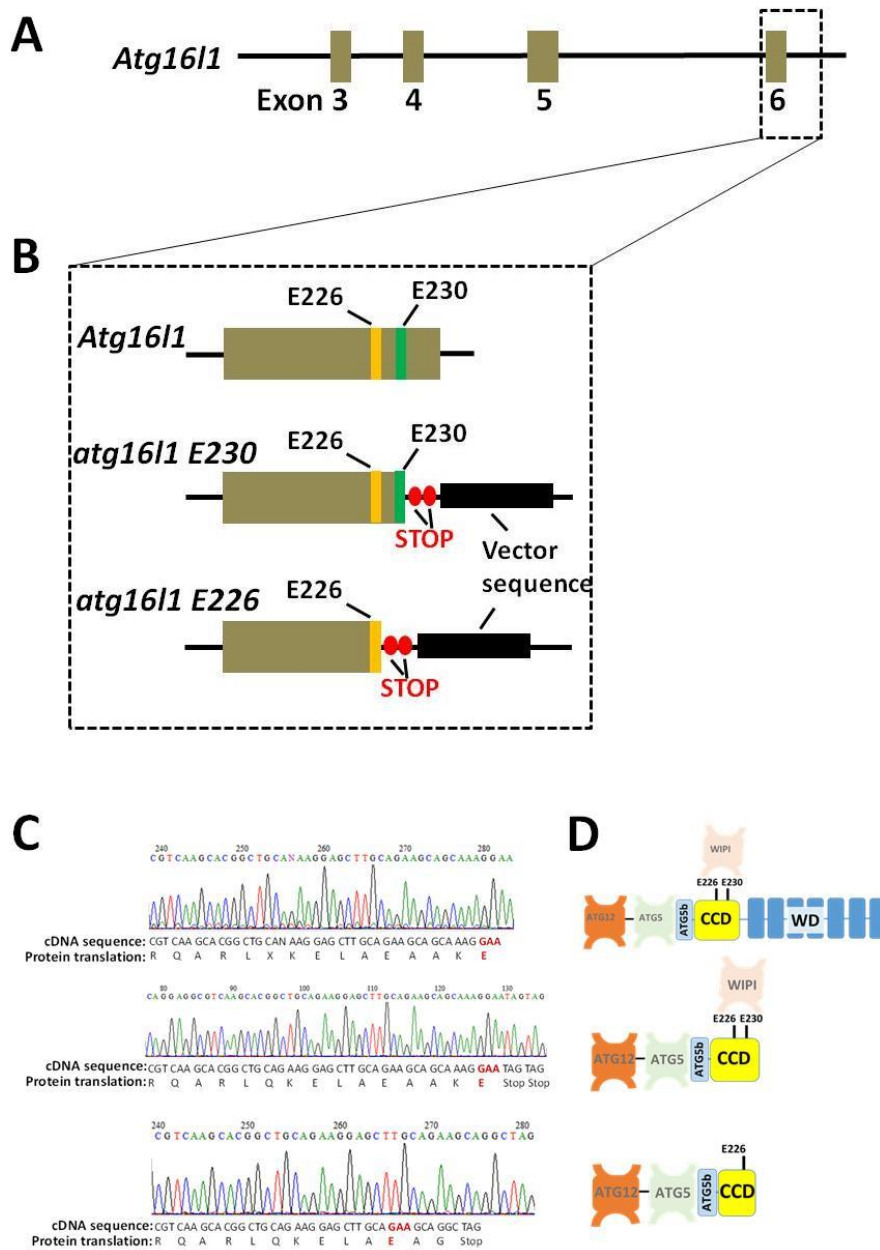


Figure 8: Deletion of WD domain of ATG16L1: **A.** The representative exon map of *Atg16l1* gene shows the exon 6 which was engineered to remove WD domain. **B.** The magnified view of exon 6 (representative) highlighting the regions on the gene, specific for glutamate residues at 226 (E226, yellow) and 230 (E230, green) positions on CCD. In *atg16l1^{E230}* mice, two stop codons (red circles) were introduced after sequences corresponding to glutamate 230 to remove the WD domain. In *atg16l1^{E226}* mice the stop codons got placed after glutamate 226 sequences removing glutamate 230 sequences. Part of targeting vector sequences (black region) was inserted along with the stop codons near exon 6. **C.** The c-DNA sequencing results showing peaks along with corresponding amino acid sequences highlighting positions of glutamate residues (E) and stop codons in the genomic DNAs from control, E230 and E226 mice. **D.** The representative domain diagram of full length, E230 and E226 versions of ATG16L1 protein, indicating role of E230 and E226 residues in WIPI2 binding. The WIPI2 binds to full length and E230 version of ATG16L1 through glutamate 226 and 230 but not with E226 version because of loss of glutamate 230.

Chapter-2

Materials and methods

2.1 Genotyping:

2.1.1 Reagents: Tris base (Fisher Scientific, BP152-1), HCl (Fisher Scientific, H/1200/PB08), EDTA (Fisher Scientific, BP120-500), Acetic acid (Fisher Scientific, A/0360/PB17), SDS (Fisher Scientific, BP166-500), NaCl (Fisher Scientific, S/3160/60), Proteinase-K (non-commercial), Sterile water (Fisher Scientific, BP2484-100), dNTPs (Bioline, BIO-39025), Oligonucleotide primers (Sigma Aldrich), 10X Dream Taq Buffer (with MgCl₂) with Dream Taq DNA polymerase (500U, 5U/μl, Thermo Scientific, REF EP0702), Agarose (Bioline, BIO-41025), Glycerol (Fisher Scientific, 10795711), Orange G (Sigma, O3756), Ethidium bromide (Fisher Scientific, E/P800/03)

2.1.2 Polymerase chain reaction (PCR): Mice ear biopsies were digested in lysis buffer (100 mM Tris-HCl pH 8.5, 5 mM EDTA pH 8.0, 0.2% SDS, 200 mM NaCl, 100μg/ml Proteinase K and sterile water) overnight at 55°C. Lysed biopsies were diluted 1:20 in distilled water before being used as template for the PCR using specific oligo-nucleotide primers (Table 1B). The PCR mix was prepared (Table 1A), and PCR program (Table 1C) was executed for (~2 hours) using thermos-cycler (Applied biosystems, Veriti 96 well). PCR products were stored at 4°C until further step.

Table 1: Genotyping PCR details:

| (A). PCR mixture recipe: | (B). Sequence of primers used: |
|--|---------------------------------------|
| dNTP mix = 0.5 μl (250 μM) | 290 (forward): CAAATATGCCTTCAGAACTG |
| Dream Taq Buffer (10X with MgCl ₂) = 5.0 μl (1X) | 291 (reverse) :GCTGTAGTTCCAATCCCTAA |
| Forward & reverse primer mix = 1.0 μl (20pM) | 338 (reverse) :TCGATGCTAGCCTACTATTC |
| Dream Taq DNA polymerase = 0.25 μl | |

| | |
|--|--|
| Biopsy lysate (1:10 diluted) = 3 μ l | |
| Water = 40.25 μ l | |
| Total = 50.0 μ l | |
| (C). PCR program used: Touchdown PCR (Annealing temperature decreases from 65°C to 56°C at the rate of 1°C/cycle) | |
| 95°C – 10 minutes | |
| 95°C – 45 seconds | |
| 65°C – 1min (decreases 1°C/ cycle) | |
| 72°C – 1 minute | |
| 95°C – 45 seconds | |
| 55°C – 1 minute | |
| 72°C – 1 minute | |
| 72°C – 10 minutes | |
| 04°C – forever (hold) | |

2.1.3 Agarose gel electrophoresis: The agarose gels were casted by boiling 1% agarose solution (in TAE buffer) and then cooled down to room temperature after pouring it in a casting tray with the combs to create wells. Gels were submerged in electrophoresis tank filled with TAE buffer. The genotyping PCR products were mixed with 5X orange coloured DNA loading dye (50% Glycerol + 1X TAE buffer + 0.25g Orange G dye + distilled water) (1:5) and appropriate amount of the mixture was loaded in the wells of agarose gels. For every gel, one well was loaded with standard DNA size markers to facilitate size determination. Samples were subjected to electrophoresis by applying electricity at constant 250 volts for 40minutes. Gels was then stained in staining buffer (TAE buffer with 0.1% Ethidium bromide) for 30 minutes and visualised using gel documentation system fitted

with UV light source and camera. Genotypes were defined based on expected amplicon sizes as shown in the table below.

Table 2: Expected results of PCR and annotation of genotypes:

| Strain | Primer pair used | Genotype | Expected amplicon size |
|--------|------------------|--------------------|------------------------|
| E230 | 290 & 291 | Wild Type (+/+) | 291 bp |
| | | Heterozygous (+/-) | 291 bp& 639 bp |
| | | Mutant (-/-) | 639 bp |
| | 290 & 338 | Wild Type (+/+) | No amplification |
| | | Heterozygous (+/-) | 179 bp |
| | | Mutant (-/-) | 179 bp |
| E226 | 290 & 291 | Wild Type (+/+) | 291 bp |
| | | Heterozygous (+/-) | 291 bp& 639 bp |
| | | Mutant (-/-) | 639 bp |
| | 290 & 338 | Wild Type (+/+) | No amplification |
| | | Heterozygous (+/-) | |
| | | Mutant (-/-) | |

2.2 Isolation and culture of primary cells:

2.2.1 Reagents: DMEM(ThermoFisher scientific, Gibco, 11570586), FBS (ThermoFisher scientific, Gibco, 10500-064), Penicillin-streptomycin (ThermoFisher scientific, Gibco, 15140-122),Trypsin (ThermoFisher scientific, Gibco, 25200-072), Cell strainers (40µm, ThermoFisher scientific, 22363547), Ethanol (VWR, 20821.330), RPMI (ThermoFisher scientific, Gibco, 61870-010), M-CSF (Peprotech, 315-02-100µG)

2.2.2 Mouse embryonic fibroblasts (MEFs): To make MEFs, 13.5 days pregnant females were sacrificed and the embryos were dissected out. After removing the liver, heart and head, rest of the body of embryos were cut into small pieces and submerged in DMEM media. A small tail piece from all the embryos were frozen to confirm genotypes later. These embryos were further digested for 30-60 minutes at 37°C by adding trypsin in the suspension. Once a fine suspension was ready, it was passed through cell strainers to filter out tissue chunks. The cells were then grown in growth media (DMEM+10% FBS+1% Penicillin-streptomycin) till confluent. The MEF culture from embryos of required genotypes (e.g. E230, E226 and littermate controls) were continued and rest (e.g. heterozygous for E230 and E226) were frozen.

2.2.3 Mouse skin fibroblasts: Small shaved area of mice skin were cut in to small pieces, washed with 70% ethanol and then grown in growth media (DMEM+10% FBS+1% Penicillin-streptomycin) in a 24 well plate. Skin fibroblasts were gradually migrated from tissue to the plate within 7 days. The cells continued to grow for 1-2 weeks.

2.2.4 Mouse bone marrow derived macrophages (BMDMs): Femur bone from mice legs were dissected out and attached muscle, ligaments and tendons were cleaned off. The bone marrow cells were flushed out by passing RPMI media through bone. Those cells were filtered through cell strainer and collected in 15 ml tubes. Cells were pelleted down by centrifugation at 1000 rpm for 5 minutes. Cell pellets were re-suspended in growth media (RPMI +10% FBS+1% Penicillin-streptomycin), seeded on 100 mm tissue culture dishes and cultured in presence of growth factor M-CSF (50ng/ml) for 72 hours. After this the cells were washed and re-supplemented with growth media with M-CSF and cultured for further 72 hours.

2.3LC3-associated phagocytosis (LAP) assay:

2.3.1 Reagents: Carboxyl-modified beads (Polybead carboxylate 3.0 µm, Bangs Laboratories, 09850), Pam3csk4 (Invivogen, TLRL-PMS), MES free acid (Sigma, M8250), NaOH (Fisher Scientific, S/4920/53), EDC (Sigma), PBS (Oxoid, BR0014G), Tween-20 (Sigma, P1379), EDAC/ WSC (Sigma),

Glycine (Fisher Scientific, BP38-1), Blocking molecules, Methanol (VWR, 20847.320), Goat serum (ThermoFisher Scientific, Gibco, 16210-072), Triton X-100 (Sigma, T8787), Anti LC3 A/B antibody (Cell Signalling Technologies, 4108), Anti Rabbit secondary antibody (Alexa 488, Invitrogen, A11008), DAPI (Thermo Scientific, 62248), BSA (EUROPA, EQBAH62-1000), Fluoromount-G (SouthernBiotech, 0100-01)

2.3.2 Coating of beads: Carboxyl polystyrene particles (beads) were coated with Pam3csk4 by via following steps (Bangs Laboratories, Inc. Tech Note 205, III).

2.3.3 Preparation of beads: 2.5×10^6 beads were added to 62 μl of 0.1M MES buffer (aqueous solution of MES free acid with pH adjusted to 5.7 – 7.2 via HCl/ NaOH).

2.3.4 Preparation of coating: 5 nano moles of amino modified oligonucleotide were added to 25 μl of 0.1M MES buffer followed by 0.3 mg of EDC (1-ethyl-3-(3-dimethylaminopropyl) carbodiimide hydrochloride) and then vortexed before incubation for 20 minutes at room temperature. This step (0.3 mg EDC addition, vortexing and incubation) was repeated thrice and a final incubation at room temperature was given for 80 minutes on a rotary mixer. Mixture was centrifuged and the pellet was re-suspended in 1 mL of 0.1M PBS containing 0.02% Tween-20. Once again the mixture was centrifuged and pellet was re-suspended in 150 μl of TE buffer (10 mM Tris, pH 8.0 + 1 mM EDTA, pH 8.0 + distilled water). Finally this mixture was again subjected to centrifugation followed by pellet re-suspension in 200 μl of TE or IBS and stored at 4°C until further use.

2.3.5 Coating process: 40 μl of beads (25mg/ml) were washed (mixed and centrifuged) twice in 1ml of activation buffer (MES) and the pellet was re-suspended in 100 μl of activation buffer (MES), ensuring that the beads are well suspended (by vortexing). This made the bead suspension dilute to 10 mg/ml. While mixing, 1mg of Water soluble carbodiimide (WSC) was added and allowed to react for 15 minutes at room temperature (18-25°C). Beads were washed twice (mixed and centrifuged) in and then re-suspend in 50 μl of coupling buffer (PBS) with

continuous mixing to keep them well suspended. The coating preparation (1-10X excess of calculated monolayer) was mixed with 50µl of coupling buffer, combined with bead suspension and allowed to react at room temperature for 2-4 hours with constant mixing. Coated beads were washed and re-suspended in 100µl of quenching solution (30-40 mM Glycine + 0.05-1% w/v Blocking molecules) while mixing gently for 30 minutes. Beads were finally washed and re-suspended in storage buffer (0.01-0.1% w/v blocking molecule, pH 7.0-7.5) to desired storage concentration (10 mg/ml). These coated beads were stored at 4°C until used.

2.3.6 Assay: Actively growing BMDMs on cover glasses (in RPMI +10% FBS+1% Penicillin-streptomycin) were fed with coated beads at a ratio of 1:10 (cell: bead) for 90 minutes. After incubation, media was removed, cells were washed with PBS and fixed by adding chilled methanol and incubating at -20°C for 7 minutes. Cells were washed with PBS and then permeabilized and blocked simultaneously by incubating for 30 minutes (with slow rocking) in blocking cum permeabilization buffer (5% Goat serum + 0.3% Triton X-100+ PBS). Cells were probed with appropriately diluted (dilution buffer = 1% BSA + 0.3% Triton X-100 + PBS) anti LC3 antibody (Rabbit, polyclonal) at 4°C overnight. Next day, the cells were washed with PBS, incubated with secondary antibody (Anti rabbit, green fluorescent) for 2 hours at room temperature (protected from light). The cells were washed with PBS, stained with DAPI (diluted 1:5000 in PBS) for 5 minutes at room temperature and washed again to remove excess DAPI. Finally the cover glasses (with attached cells) were mounted on glass slides using mounting media (Fluoromount-G). The cells were observed under fluorescent microscope for LC3 associated phagosomes containing beads.

2.4 Autophagy assay:

2.4.1 Reagents: HBSS (ThermoFisher scientific, Gibco, 14025-050),

2.4.2 Assay: Approximately 2×10^6 cells (e.g. MEFs or skin fibroblast) were grown on cover glasses in 24 well tissue culture plates. Once the cells were fully attached on cover glasses, the

unattached cells were washed out by PBS and cells were further grown in either growth media (DMEM/ RPMI +10% FBS+1% Penicillin-streptomycin) or starvation media (HBSS) for 2 hours. After incubation, cells were washed, fixed and processed as mentioned in the previous section (LAP assay). Cells were observed under fluorescent microscope for active autophagy as LC3 puncta (autophagosomes).

2.5 Fluorescent microscopy: Mounted cells (e.g. BMDMs, MEFs or skin fibroblasts) were observed for green and blue fluorescence. Fluorophores were excited with appropriate light source and emitted signal were observed under 63X objective followed by photographing through the mounted camera.

2.6 Western blotting: Based on the downstream application, western blotting was done in following three ways:

2.6.1 Reagents: M-PER (ThermoFisher Scientific, 78501), Protease inhibitor cocktail (Sigma, Roche, 04693159001), BCA assay kit (ThermoFisher Scientific, 23225), Precast SDS-PAGE gels (RunBlue 4-12%Bis-Tris gels, Expedeon, NBT41212), PVDF membrane (Immobilon, Millipore, IPFL00010), Skimmed milk (Oxoid, LP0031), Anti ATG16L antibody (MBL, M150-3), Anti p62/SQSTM1 (Abcam, ab91526), Anti β actin/ ACTB antibody (Sigma, A5441), IRDye labelled secondary antibodies (LI-COR biosciences, 926-32211, 926-68020), Sodium deoxycholate [Sigma, D-5670], Protease inhibitor (Sigma, P8340), Phosphatase inhibitors (Sigma, P5726), anti GAPDH antibody (Abcam, ab9482), Nitrocellulose membranes (Bio-Rad, 1620115), Supersignal West Pico chemiluminescent substrate (ThermoFisher Scientific, 34080).

2.6.2 Cell western blotting: Approximately 2×10^6 cells were washed with PBS, detached by scrapping in 100 μ l of lysis buffer (M-PER + protease inhibitor cocktail), re-suspended and incubated on ice for 30 minutes. The lysates were centrifuged at 16000Xg (at 4°C) and supernatants were transferred to fresh tubes. Total proteins were quantified by BCA assay kit. Equal amount of protein was loaded in the wells of precast SDS-PAGE gels and electrophoresed

at 150 volts for nearly 2 hours. Separated proteins were transferred to PVDF membrane by standard wet transfer protocol and apparatus. After transfer, membranes were incubated in blocking buffer (5% skimmed milk in 1X TBS [50mM Tris (pH 7.5) + 150mM NaCl]) for 1 hour at room temperature followed by probing with appropriately diluted (in blocking buffer) primary antibodies (Anti ATG16L, Anti LC3 A/B, Anti p62/ SQSTM1 and Anti β actin antibodies) (at 4°C for overnight). Next day, the blots were washed thrice, for 15 minutes each, in wash buffer (1X TBS + 0.5% Tween 20) and probed with 1:10000 diluted secondary antibodies (IRDye labelled) (at room temperature for two hour, protected from light). After one hour, the blots were again washed thrice, as before, and the signals were (visualized and imaged) using the Odyssey infrared system (LI-COR).

2.6.3 Tissue western blotting: Mice were dissected to harvest organs (e.g. livers, kidneys muscles and brains). Organs were snap frozen in liquid nitrogen and stored in -80°C freezer until further used. Using a clean and chilled mortar, pestle and liquid nitrogen, frozen organs were crushed into fine powder. Appropriate amount of crushed organs were suspended and lysed in RIPA buffer (150 mM NaCl + 1% TritonX-100 + 0.5% Sodium deoxycholate + 0.1% SDS + 50 mM Tris, pH 8.0 + protease and phosphatase inhibitors) by incubating on ice for 30 minutes, further homogenisation and subjecting to freeze thaw cycles. Lysates were briefly sonicated followed by centrifugation at 16000Xg to transfer supernatants into fresh tubes. Total proteins were quantified (BCA assay kit), resolved on SDS gels (4-12% Bis-Tris gels), transferred to nitrocellulose membranes and probed with appropriate primary (Anti ATG16L, Anti LC3 A/B, Anti p62/ SQSTM1 and anti GAPDH antibodies) and secondary antibodies (1:5000 of Anti-mouse HRP or anti-rabbit HRP) as mentioned above. The signal was developed via exposure to chemiluminescent HRP substrates (Supersignal West Pico) and imaged by Chemidoc XR system (BioRad). Images were quantified via Image J (NIH, USA) and plotted by using GraphPad Prism 7.

2.7 Growth rate measurements: Mice were weighed every week (from 3rd to 9th week post birth). Growth rates were measured by plotting body weights (g) on Y axis and time (weeks) on X axis using GraphPad Prism 7.

2.8 Fertility assessment: Mice breeding pairs were continuously monitored for recording the number of pups born along with their genotypes.

2.9 Morphological analysis of different tissues: Whole bodies and dissected tissues from control and mutant mice were photographed and weighed. Tissue weights (g) and the percentage of ratio of tissue to whole body were plotted as columns using GraphPad Prism7.

2.10 Tissue preservation and processing:

2.10.1 Reagents: NBF (Sigma, HT501128),

2.10.2 Process: Dissected tissues were fixed by submerging in 10% neutral buffered formalin (NBF) for overnight at room temperature. Next day, the tissues were transferred to 70 % ethanol and stored at room temperature until further processing. Tissues were later subjected to overnight dehydration in an automatic tissue processor (Leica, ASP 300S). Next day, those dehydrated tissues were submerged and stored in molten paraffin wax (Paraplast, Sigma, P3558) till embedding station (Leica, EG1150) was ready to be used. Tissues were, one by one, embedded in paraffin wax by placing them in correct orientation on top of a partially solidifies thin paraffin layer inside a metal or plastic mould. Once the tissue was set on its position, rest of the volume of mould was filled with molten paraffin wax and allowed to cool down by putting on top of precooled platform. This process generated solid cuboidal tissue blocks for long term tissue preservation. These formalin fixed paraffin embedded (FFPE) tissue blocks were stored at room temperature before making 5 μ thick sections using microtome (Microm, HM355S).

Tissue sections were generated by first cooling the tissue blocks for easy cutting. The cooled blocks were fixed on the holder and several 5 μ thick sections were sliced out using microtome

(Microm, HM355S). Those thin sections were overlaid on top of warm water (42°C) to flatten them. These sections were then carefully transferred on glass slides (Thermo Fisher Scientific, Superfrost plus, J1800AMNZ) and left to stick and dry overnight at room temperature. These sections were labelled and stored for further staining procedures like H & E staining or immunostaining.

2.11 Haematoxylin and Eosin (H & E) staining of tissue sections:

2.11.1 Reagents: Histoclear (National diagnostics), Harris hematoxylin (Sigma, HHS128), Sodium bicarbonate (ThermoFisher Scientific, S/4240/53), Eosine (Sigma, HT110116), DPX mounting medium (ThermoFisher Scientific, D/5319/05).

2.11.1 Process: Above tissue sections were H & E stained by passing them through different solutions as indicated in table 3:

Table 3: Hematoxylin-eosin staining procedure of formalin fixed paraffin embedded tissue sections:

| Step no. | Solution | Time |
|----------|---------------------------------|-------------|
| 1 | Histoclear solution-I | 5 minutes |
| 2 | Histoclear solution -II | 5 minutes |
| 3 | 100% Ethanol | 2 minutes |
| 4 | 80% Ethanol | 2 minutes |
| 5 | 70% Ethanol | 2 minutes |
| 6 | Rinsing under running tap water | 5 minutes |
| 7 | Hematoxylin solution | 2 minutes |
| 8 | Washing under running tap water | 5 minutes |
| 9 | 1% HCl in 70% Ethanol | 15 seconds |
| 10 | Rinsing in water | ~10 seconds |

| | | |
|----|----------------------------------|------------|
| 11 | 0.1% Sodium bicarbonate solution | 1 minute |
| 12 | Washing under running tap water | 5 minutes |
| 13 | Eosin solution | 30 seconds |
| 14 | 70% Ethanol | 2 minutes |
| 15 | 80% Ethanol | 2 minutes |
| 16 | 100% Ethanol | 2 minutes |
| 17 | Histoclear solution -II | 5 minutes |
| 18 | Histoclear solution -I | 5 minutes |

Sections were then mounted using cover glasses and mounting media (DPX) followed by overnight drying at room temperature. Those sections were observed under bright field microscope.

2.12 Immunostaining of tissue sections:

2.12.1 Reagents: Tri Sodium Citrate di hydrate (Fisher Scientific, S/3320/53), Citric acid (Fisher Scientific, S/6200/53), Hydrogen peroxide (Sigma, 216763), Antibody dilution buffer (Dako, K3468), Chromogen buffer (Dako, K3468), anti MKI67/Ki67 antibody (Abcam, ab66155), anti ITGAM/Cd11b antibody (Abcam, ab133357), Anti rabbit-HRP (Dako, K4003),

2.12.2 Process: Tissue sections (after sectioning and drying) were first de-paraffinised and rehydrated by following steps 1-6 of table 3. Antigen retrieval was performed by microwaving (600 watts) the sections in antigen retrieval buffer (~0.053% w/v Tri Sodium Citrate di hydrate + 0.17% w/v Citric acid + distilled water), twice for 10 minutes each, with replenishment of lost buffer. Sections were left in the antigen retrieval buffer to cool down at room tempera before washing them in PBS (thrice for 3 minutes each). Sections were incubated for 10 minutes at room temperature in 10% (v/v) hydrogen peroxide (H₂O₂) solution in methanol (CH₃OH) to block active peroxidases followed by washing in PBS as before. Non-specific binding site were blocked

by incubation in blocking buffer (10% v/v Goat serum + 0.3% v/v Triton X-100 + PBS) for 1 hour at room temperature before overnight probing with primary antibody (diluted in antibody dilution buffer) (anti SQSTM1/p62 antibody, anti MKI67/Ki67 antibody, anti ITGAM/Cd11b antibody) at 4°C. Next day, tissue sections were washed in PBS (as before), probed with appropriate secondary antibody (diluted in antibody dilution buffer) (anti rabbit-HRP; Dako, K4003) for 1 hour at room temperature, washed again and developed by adding chromogen buffer (2% v/v Chromogen + Substrate buffer). Once sufficient signal was observed under microscope, the reaction was stopped by submerging the sections in PBS. Finally sections were counter stained by following steps 6-18 (H & E staining) and avoiding step 13. Sections were then mounted using cover glasses and mounting media (DPX) followed by overnight drying at room temperature. Next day those sections were observed under bright field microscope (Axioplan 2, Zeiss, fitted with coloured Axio Cam HRc camera).

2.13 Liver enzyme assay:

2.13.1 Reagents: ALT/ GPT assay kit (Roche),

2.13.2 Process: Levels of Alanine amino transferase (ALT) also known as Glutamate pyruvate transaminase (GPT) in mice blood serum were measured as a marker for liver damage. Mice were killed by cervical dislocation and their hearts were punctured to collect blood through a sterile 1 ml needleless syringe. Collected blood samples were left at room temperature for 30 minutes to clot followed by centrifugation at 3000 rpm for 10 minutes. Supernatants (serums) were transferred to fresh tubes, snap frozen in liquid nitrogen and then stored in -80°C freezer for later use. At the time of assay, serums were thawed on ice, appropriately diluted and transferred to 2ml assay tubes along with enzyme substrate standards. The assay tubes were placed in respective slots of the automatic reader and the appropriate program was executed. The machine automatically prepared serial dilution of substrate standards to generate a standard curve. The software then used the standard curve to calculate and display final

concentration of ALT (units/ml) in serum samples. The data was plotted and compared using GraphPad Prism7.

2.14 Gel filtration chromatography:

2.14.1 Reagents: ENrich™ SEC 650 (Bio-Rad, 780-1650), Blue dextran (Sigma, D4772-1VL), protein standards (Sigma, MWGF1000), Anti ATG5 antibody (Abcam, ab108327), Anti WIPI2 antibody (Abcam, ab101985).

2.14.2 Process: Freshly dissected liver and brain tissues were Dounce homogenised in chilled PBS (supplemented with protease inhibitor cocktail). Tissue homogenates were clarified by first spinning at 100Xg (4°C) for 5 minutes (no pallet) and then 13000Xg (4°C) for 20 minutes. The supernatants were used to separate cytoplasmic fractions by spinning at 100,000Xg at 4°C for 1 hour. Obtained supernatants (cytoplasmic fractions) were then loaded on a gel filtration column (ENrich™ SEC 650) to purify (AKTA purifier, GE Healthcare) protein complexes of different sizes collected as various eluted fractions. Those fractions were then analysed for the presence of ATG16L1, ATG5 and WIPI2 proteins via SDS-PAGE and western blotting. For size determination of protein complexes, the void volume (V_0) of the column and elution volume (V_e) of known protein standards were obtained by sequentially passing blue dextran and mixture of protein standard through the column. A standard curve was generated by plotting the ratios (V_e/V_0) on X axis and log of molecular masses on Y axis. Size of different protein complexes were extrapolated through the standard curve.

2.15 Cytokine assay:

2.15.1 Reagents: ProcartaPlex™ Simplex Immunoassay kits (ThermoFisher Scientific, EPX01A-26015-901, EPX01A-20603-901, EPX01A-26004-901, EPX01A-26005-901, EPX01A-20607-901 and EPX01A-26002-901).

Serums from young(2-3 months old) and aged(5-6 months old) mice were used to measure cytokine levels using various Luminex kits (ProcartaPlex™ Simplex Immunoassay kits)by following manufacturer's instructions:

2.15.2 Standard preparation: Based on antigens of interest, various lyophilised specific antigen standards were first reconstituted in 1X universal assay buffer and then combined appropriately to a final volume of 250µl. Standards were serially diluted up to 4 folds using 1X universal assay buffer and stored on ice until used.

2.15.3 Magnetic bead preparation: According to the need of specific antibodies, a(1X) 5ml pool of magnetic beads was prepared by combining 100µl each from various (50X) suspensions of beads coated with capture antibodies against specific antigens, in 1X wash buffer. The mixture was stored on ice until used.

2.15.4 Detection antibody preparation: As per use of capture antibodies (on beads), a pool of different detection antibodies was prepared by diluting 50X stocks (of each) in antibody diluent to a final volume of 3 ml (1X).

2.15.5 Assay: The assay plate was secured on the hand-held magnetic plate holder and appropriate amount of magnetic bead mixture was added in each well. Beads were allowed to accumulate at the bottom of wells for 2 minutes and then the liquid was removed by inverting the plate (with magnetic holder) on a paper towel. Beads were washed in 150µl (1X) wash buffer in the similar fashion. In each designated well 25µl of (1X) universal assay buffer and 25µl of corresponding antigen standard or sample (serum) was added. The wells dedicated for blanks were filled with 25µl of (1X) universal assay buffer. The plate was sealed, covered and incubated with shaking at 500 rpm for overnight at 4°C. Next day the plate was further incubated, with shaking at 500 rpm for 30 minutes at room temperature before washing three times as before. 25µl of 1X detection antibody mixture was added in each well followed by sealing, covering and incubation (500 rpm) for 30 minutes at room temperature. Wells were washed thrice as earlier

before adding 50µl of SAPE in each well. Again the plate was sealed, covered and incubated (500 rpm) at room temperature for 30 minutes. After washing thrice, 120µl of reading buffer was added in each well and the plate was sealed, covered and incubated for 5 minutes (500 rpm) at room temperature. Plate was read on Luminex instrument (Luminex™100/200™), obtained data was plotted and analysed using GraphPad Prism7.

Chapter-3

Analysis of canonical and non-canonical autophagy in mice lacking the WD domain of ATG16L1

3.1 Generation of mice: Unlike yeast, the ATG16L1 protein of higher eukaryotes including mammals carries a C-terminal WD40 domain (Figure 7A & B). As published earlier WD40 domain is reported to play a role in non-canonical autophagy 'in vitro'(67). To extend this finding mouse models lacking the WD40 domain of ATG16L1 (Δ WD) were generated by Maryam Arasteh, a PhD student in the lab (Julia Maryam Arasteh, PhD thesis, 2012) (Figure 8A-D). These mice were made by introducing two stop codons at the end of coiled coil domain (CCD) to preserve the glutamate residues at 226 (E226) and 230 positions (E230) in CCD of ATG16L1 as they are required for its interaction with WIPI2 protein to activate autophagy (42) (Figure 9A-D).

The exact location of coiled coil domain (CCD) on the *Atg16l1* gene was already worked out in yeast homologue which was later shown to be conserved in mice (68, 69). The stop codons were introduced into exon 6 to ensure its presence in all the four alternate spliced forms of *Atg16l1* (Figures 9A&B). The final targeting vector containing the neomycin resistance gene, bovine growth hormone polyadenylation site (bGH-pA) and frt sequences was transfected into mouse embryonic stem (ES) cells and the positive cells were selected based on neomycin resistance (Figure 10A). The ES cell clones that had undergone correct homologous recombination (Figure 10A) were selected via southern blotting and PCR. These cells were injected into blastocyst and transplanted in to a surrogate mouse mother.

The chimeras delivered by the surrogate mother were confirmed for the presence of mutation by PCR. These chimeras were crossed with C57BL/6 to confirm the germ line transmission of the mutation. Once the mutation was confirmed via PCR in the offspring, they were subjected to further crosses with Flp mice and C57BL/6, respectively, to remove neomycin resistance gene and flp gene

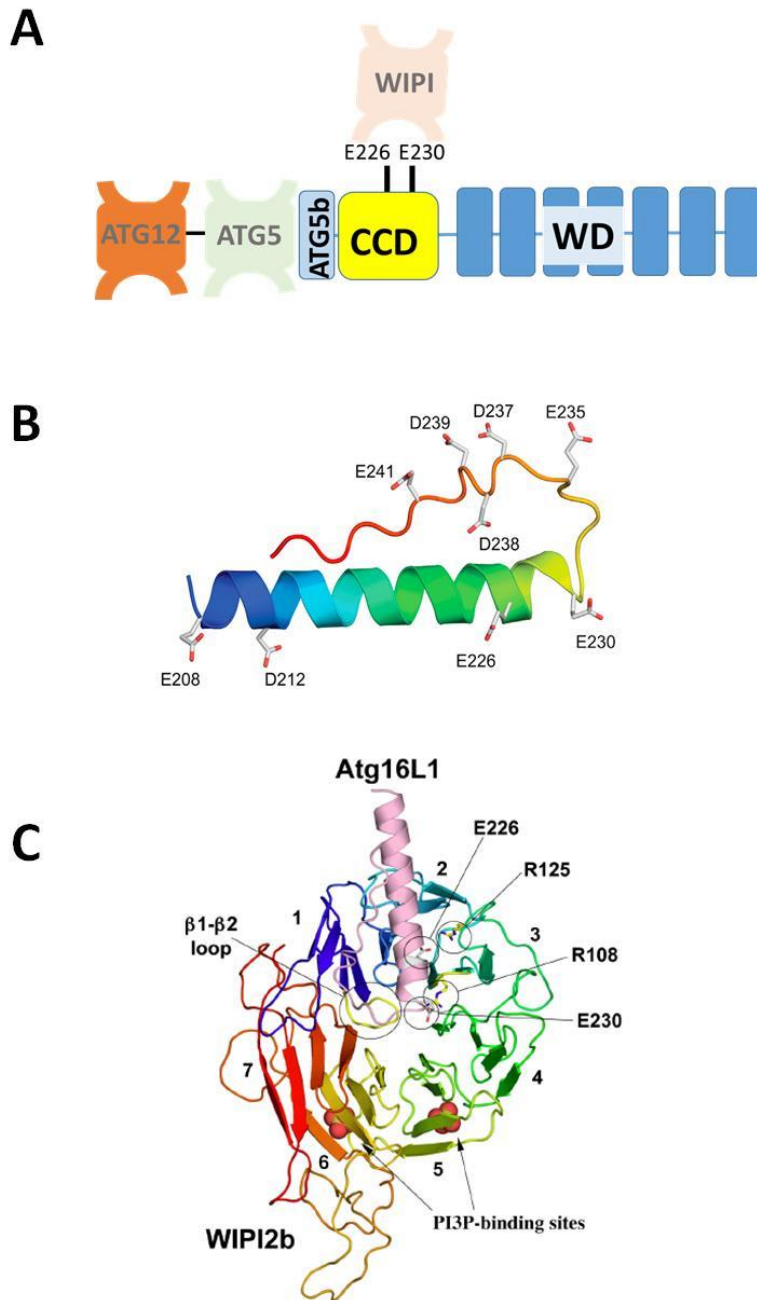


Figure 9: Key residues of CCD mediate WIPI2 binding: **A.** The graphical model shows that ATG16L1 is made up of an N terminal ATG5 binding domain (ATG5b), a coiled coil domain (CCD), a linker region and an N terminal WD domain. The glutamate residues at 226 (E226) and 230 (E230) positions on CCD are essential for WIPI2 binding. **B.** Structural model (taken from ref. 39) of CCD of ATG16L1 showing important residues required for its interaction with WIPI2. **C.** Structural model of WIPI2 (circular β pleated structure) in association with CCD of ATG16L1 (pink coloured α helix) highlighting key residues of CCD (E226, E230) and WIPI2 (R125, R108) required for interaction. The WIPI structure also shows PI3P binding sites and 7 β blades and β 1- β 2 loop, a major distinguishing feature between WIPI isoforms (taken from ref. 39).

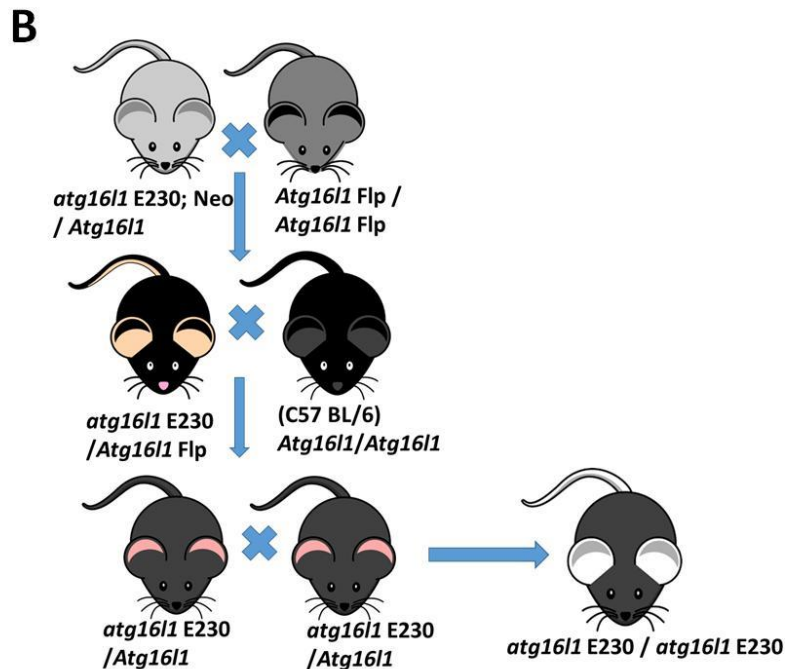
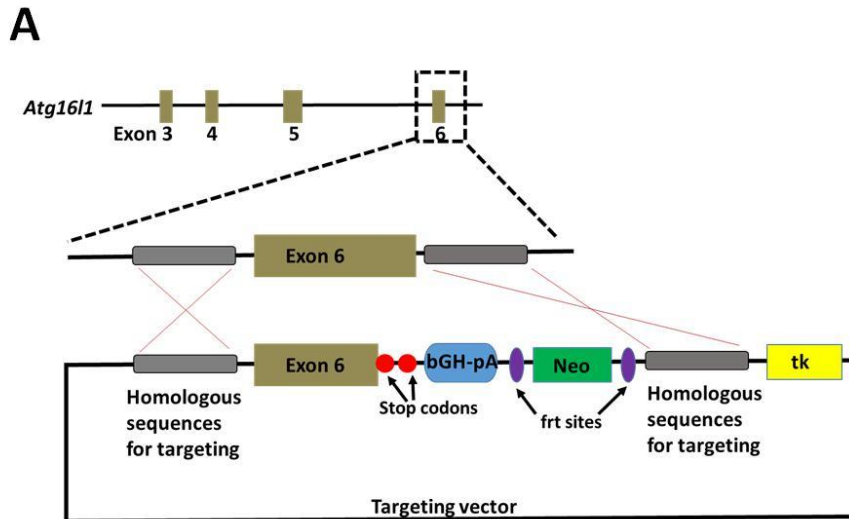


Figure 10: Generation of mice deficient in WD domain: A. Exon 6 of *Atg16l1* gene was engineered to create WD deficient mice. The targeting vector containing upstream and downstream regions of homology, engineered exon 6, stop codons, polyadenylation sequence (bGH-pA), frt sites, neomycin resistance gene and a thymidine kinase gene (tk) was used for transfection. **B.** Obtained chimeras were crossed with flp mice to remove neomycin gene by flp-frt mediated excision. Further obtained mice were crossed with C57BL/6 to remove flp and to obtain pure heterozygous mice. The heterozygous mice were crossed together to obtain homozygous mutant mice.

sequentially (Figure 10B). The resulting heterozygous mice were crossed to generate homozygous mutant mice (Figure 10B). These mice were genotyped via PCR using specific primers (Figure 11A-C).

3.2 Mouse nomenclature: In generating mice lacking the WD domain, two stop codons were located after the E230 residue of ATG16L1 required for the WIP12 binding sites (Figure 9B-D). These mice were named 'E230' mice. Surprisingly, due to an unexpected recombination event, we also got a second population of mice where the stop codons got inserted after the E226 residue causing translation termination before E230 residue (Figure 9B-D). These mice were named 'E226' mice.

3.3 Genotyping by PCR: These mice were genotyped by PCR using three primers (290, 291 & 338) (Figure 11A-C). The primers 290 and 291 were designed to specifically bind to upstream and downstream intronic region of exon 6 (Figure 11A). A third primer 338 was designed to bind to the vector cassette inserted next to the exon 6. The primer set 290-291 amplified 291 bp fragment in case of littermate control mice (+/+) (Figure 11A). In case of E230 and E226 mice, because of homologous recombination and insertion of vector sequences with stop codons, the binding site of 291 got pushed further away from 290 sites (Figure 11A). Therefore, in case of mice with a copy of either E230 or E226 version of *Atg16l1* gene, the PCR amplified a fragment of 639 bp (Figure 11B & C). As expected ear lysates from all the littermate control (or wild type (WT)) mice (+/+) showed a single amplicon of 291 bp whereas biopsies from homozygous mutant mice (-/-) showed a single amplicon of 639 bp (Figure 11B & C). Heterozygous mice (+/-) with only one copy of mutant gene amplified two bands: 291 bp and 639 bp corresponding to wild type and mutant copy of genes respectively (Figure 11B & C). A third primer 338 was employed to differentiate between E230 and E226 genotypes as it was targeted to bind sequences corresponding to E230 region of exon 6 and also to the stop codons on the inserted cassette (Figure 11A). Since the sequences corresponding to E230 and stop codons were missing in E226 and littermate control (+/+) lysates, the combination of 290 and 338 primers gave a single amplification band of 179 bp for E230 mutant (-/-) and heterozygous (+/-) mice (Figure 11B).

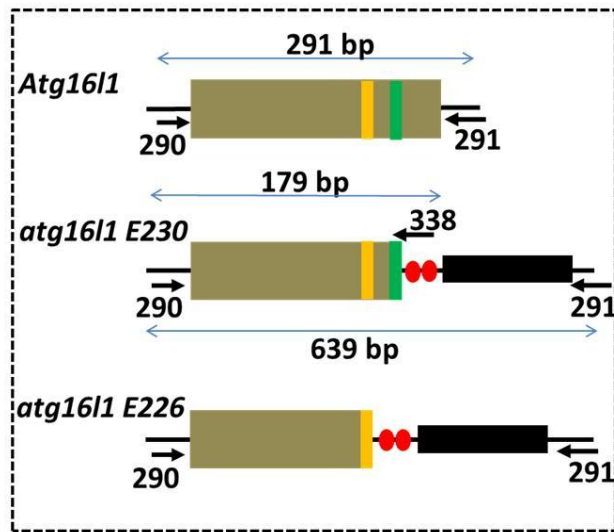
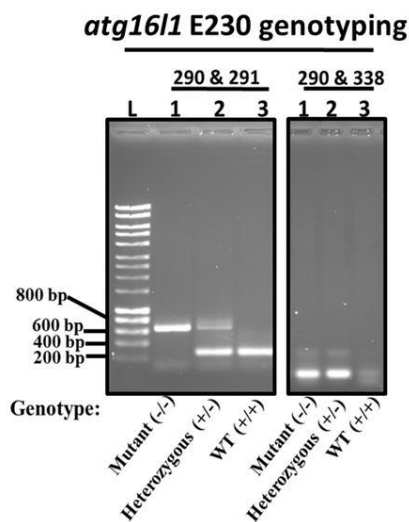
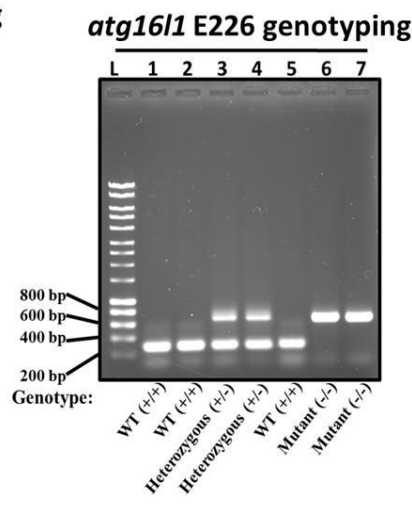
A**B****C**

Figure 11: Genotyping of WD deficient mice: **A.** The representative map of exon 6 in control (*Atg16l1*), E230 (*atg16l1^{E230}*) and E226 (*atg16l1^{E226}*) mice genomes is shown along with the sequences for glutamate residues at 226 and 230 positions indicated in yellow and green, respectively. Stop codons are shown as red circles. The specific binding regions of genotyping primers 290, 291 and 338 are indicated. The expected amplification size is indicated against each respective primer pair **B.** Agarose gel picture as a result of genotyping PCR for E230 mice is shown. The mutants (-/-) and wild types (WT, +/+), as expected, showed amplification of 639 bp and 291 bp respectively whereas heterozygous (+/-) mice showed both the band (639 bp and 291 bp). The second gel showed a single band of 179 bp for mutant and heterozygous mice but no bands for WT mice which was expected. **C.** The genotyping PCR results for E226 mice showed similar results, like E230 mice, where a band of 291 bp for WT, a band of 639 bp for mutant and both the bands were seen in heterozygous mice.

3.4 Analysis of expression of truncated ATG16L1 by western blot: Once the genotypes were assigned, cells and tissues from these mice were tested for the expression of WD deficient ATG16L1 via western blotting (Figure 10).

3.4.1 In Mouse embryonic fibroblasts (MEFs): Heterozygous (+/-) E230 mice were crossed together and pregnant females were dissected on 13.5-day post mating to harvest embryos. The embryos were used to make mouse embryonic fibroblasts (MEFs). Cells were grown in nutrient rich or starvation media for 2 hours and then lysed and immunoblotted for ATG16L1. As shown in the figure 12A, ~66 kDa (both α and β isoforms) bands corresponding to full length ATG16L1 was observed in control MEFs but not in E230 and E226 MEFs both in nutrient rich and starvation conditions. The ~66 kDa band was also missing in lysates of MEFs with full length knock out of *Atg16l1* gene (FL KO) (Figure 12A). These results confirmed the absence of full length ATG16L1 in E230 and E226 MEFs but couldn't confirm the stable expression of truncated protein of ~27 kDa.

3.4.2 In different mice tissues: Further, the expression of truncated version of ATG16L1 was examined in different mice tissues (Figure 12B). Mice were dissected to harvest liver, brain and gastrocnemius muscle. Lysates from these tissues were immunoblotted for ATG16L1 protein and as expected a ~66 kDa band of full length ATG16L1 was seen in all the tissue lysates prepared from littermate control mice (Figure 12B). Two bands corresponding to α and β isoforms of ATG16L1 were detected in liver and muscle lysates (69). Although the full length band was missing from the tissue lysates of E230 mice, a smaller band of ~27 kDa corresponding to E230 version of ATG16L1 appeared on the western blot confirming the stable expression of truncated version of ATG16L1 (Figure 12B). A smaller band of E226 version of ATG16L1 couldn't be detected possibly because of instability of the protein.

3.5 Analysis of canonical and non-canonical autophagy: To confirm that removal of WD domain of ATG16L1 didn't affect canonical autophagy but created defect in LAP, cells from E230, E226 and

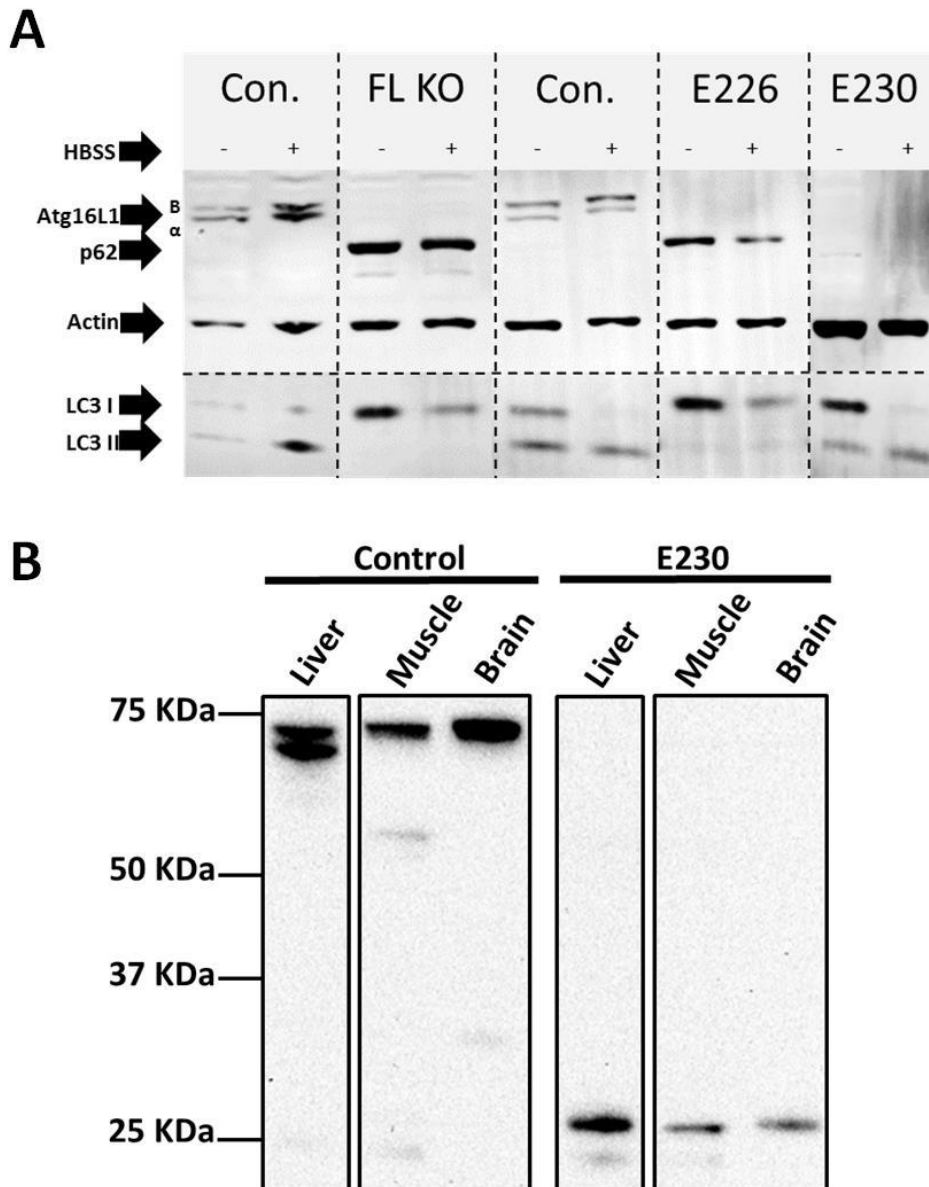


Figure 12: Role of WD domain in autophagy: A. Mouse embryonic fibroblasts (MEFs) isolated from control, E230 and E226 mice were grown in nutrient rich and starvation conditions (HBSS) for 2 hours. Cells were lysed and immunoblotted for ATG16L1, p62, LC3 and loading control protein actin. Two bands corresponding to α and β isoforms of full length ATG16L1 (~66 kDa) were observed in the lanes for control lysates (con.) but no bands were seen in the lanes of E230 and E226 MEFs. These were similar to the lane of MEFs with full length knock out of ATG16L1 (FL KO). This confirms the loss of full length ATG16L1 in E230 and E226 MEFs. Bands indicating p62 accumulation were seen in lysates of FL KO and E226 MEFs but not in control and E230 MEFs indicating loss of autophagy in FL KO and E226 MEFs. LC3-II bands corresponding to active autophagy were seen in control and E230 MEFs with more LC3-II formation upon starvation. LC3-II bands were not detected in FL KO and E226 MEFs confirming defective autophagy. Actin was used as loading control. **B.** Lysates of liver, muscle and brain from control, E230 and E226 mice were used for western blotting to detect ATG16L1. Full length ATG16L1 (~66 kDa) was detected in lysates from control mice whereas a small band of ~27 kDa, corresponding to size of ATG16L1^{E230} was seen in the lysates from E230 mice confirming the stable expression of truncated ATG16L1.

control mice were subjected to autophagy and LAP assays and results are described in the following section.

3.5.1 Status of autophagy and LAP in cells: Standard autophagy assays involve analysis of status of autophagosomal marker LC3 and cargo adapter protein p62/SQSTM1 on western blots(70).

Induction of autophagy is detected by appearance of a smaller sized LC3-II band (16 kDa) and very faint or no band for p62(70). As shown in figure 12A, MEFs from E230 mice showed LC3-II band and no p62/SQSTM1 band just like control MEFs. These results were comparable to MEFs from control mice confirming the presence of starvation induced autophagy in E230 mice. On the other hand absence of LC3-II band and high levels of p62/SQSTM1 in E226 and FL KO MEFs confirmed the defect in autophagy in these cells (Figure 12A).

Similar results were observed in microscopy based autophagy assay using E230, E226 and control MEFs and skin fibroblasts (Figure 13A & B).MEFs and skin fibroblasts were grown in nutrient rich (Media) and starvation media (HBSS) before immunostaining them for LC3. As expected, multiple green fluorescent LC3 puncta were observed in control and E230 MEFs and skin fibroblasts grown in starvation media but not in nutrient rich media confirming successful induction of autophagy (Figure 13A & B). No puncta were seen in E226 cells grown either in nutrient rich or starvation media confirming dysfunctional autophagy (Figure 13A & B).

As shown in previous in vitro studies (67), further examinations were made to test the status of LAP in bone marrow derived macrophages (BMDMs)of WD deficient E230 and E226 mice along with their littermate controls. Pam3CSK4 coated polystyrene beads were used for phagocytosis assay on BMDMs and cells were immunostained for LC3. Although macrophages from all three genotypes showed phagocytosis of beads, only control macrophages showed translocation of LC3 to phagosomes containing beads which confirmed the absence of LAP in E230 and E226 macrophages (Figure 13C). Overall these results establish that loss of WD domain doesn't disturb canonical autophagy in E230 mice cells but causes dysfunctional LAP.

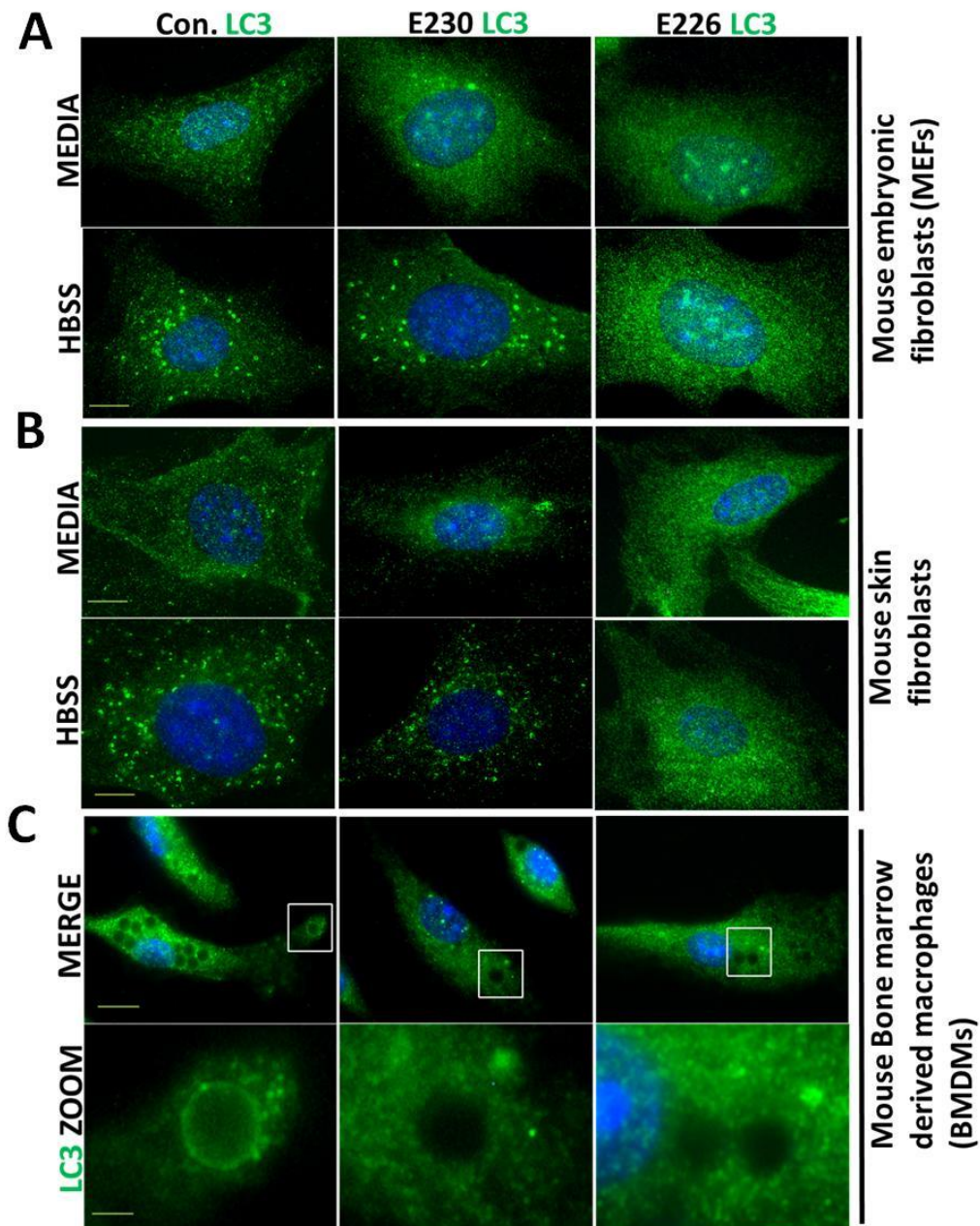


Figure 13: Role of WD domain in autophagy and LAP: A&B. MEFs and skin fibroblasts from control, E230 and E226 mice were grown for 2 hours in nutrient rich (media) or starvation conditions (HBSS). Cells were fixed and stained for LC3. Starvation induced LC3 positive puncta in control (con.) and E230 MEFs and skin fibroblasts but not in E226 MEFs or skin fibroblasts indicating defective autophagy in E226 fibroblasts. **C.** BMDMs from control, E230 and E226 mice were incubated with Pam3CSK4 coated polystyrene beads for 90 minutes then fixed and stained for LC3. Phagocytosis of beads was seen in all the cells but only control cells showed LC3 positive phagosomes (zoomed in lower panel) indicating lack of LAP in both E230 and E226 BMDMs. Magnification 63X. Scale bar 10 μ m.

3.6 Summary: LAP deficient mice (named E230 mice) were generated by placing 2 stop codons at the end of CCD while preserving glutamate residues at 226 and 230 positions required for WIPI interaction and hence for autophagy (Figure 9 A-D). Insertion of stop codon at targeted location on exon 6 was confirmed by genotyping PCR (Figure 11A-B) and expression of truncated ATG16L1 was seen in cells and tissues via western blotting (Figure 12A & B). Cells from E230 mice showed activation of autophagy via microscopy (Figure 13A & B) and western blotting (Figure 12A). No LAP activity was detected in BMDMs of E230 mice after phagocytosis of polystyrene beads (Figure 13C). Another population of WD deficient mice were generated which lacked glutamate at 230 position on CCD (Figure 9A-D). These mice were named E226 mice and cells from them were found deficient in both autophagy and LAP via western blotting (Figure 12A) and microscopy respectively (Figure 13A & B). E226 mice acted as good control against E230 and control mice to compare between autophagy and LAP.

Chapter-4

Analysis of role of WD domain in tissue homeostasis

The experiments above demonstrated that cells cultured from the E230 mice lacking the WD domain of ATG16L1 could activate autophagy but were defective in non-canonical autophagy/LAP (Figures 12A&13A-C). Further investigation was made regarding effect of loss of WD domain on tissue homeostasis. Tissues which does not make direct contact with microbes and do not fall in the category of immune organs were analysed to test the overall fitness of E230 and E226 mice. The following sections explain the role of WD domain in maintenance of tissue homeostasis in mice.

4.1 Gross morphology, weight and fertility: 2-3 months old E230 and E226 mice were compared for their body sizes, body weights and fertility with their littermate controls. E230 mice were comparable in body size with controls whereas E226 mice were smaller (Figure 14A). Body weights were recorded every week and compared as growth rate curves (Figure 14B). E230 mice grew at the same rate as control mice but E226 mice showed retarded growth rate (Figure 14B). The E226 mice, unlike E230 and litter mate controls, were non-fertile (homozygous mating) and their breeding (heterozygous mating) didn't follow Mendelian frequency (data not shown). The E230 and control mice lived more than 2 years whereas E226 mice had a maximum life span of 7 months (data not shown).

4.2 Liver:

The role of autophagy in maintenance of homeostasis in liver has already been reported. Komatsu *et al*(58) generated conditional liver specific autophagy knock out *Atg7* mice (*Atg7^{F/F}:Mx1-Cre*, plpC injected). The hepatocytes from these mice showed abnormalities in autophagosome formation, processing of LC3, GABARAP and GATE16, clearance of defective organelles such as mitochondria and peroxisomes upon starvation. Livers of these mice were abnormally large (hepatomegaly) with hepatocyte swelling, disorganised hepatic lobules and accumulation of ubiquitin tagged protein

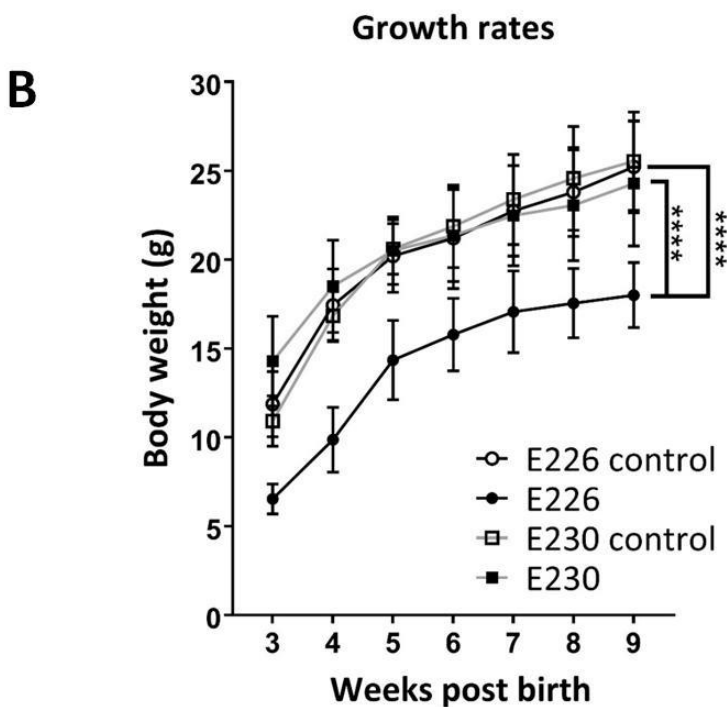
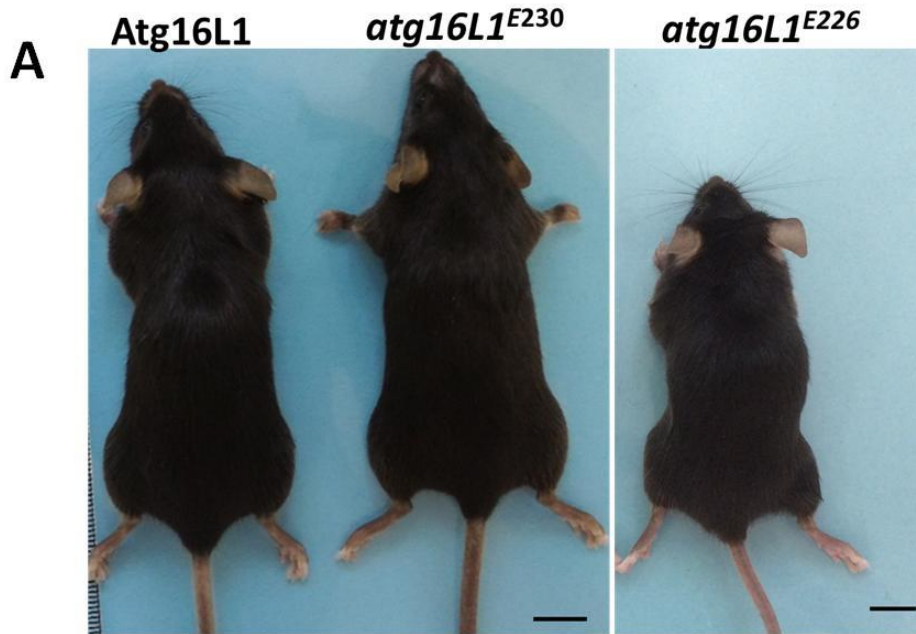


Figure 14: Phenotype of E230 and E226 mice: **A.** Representative picture of 2 months old mice compares the full body size of control (ATG16L1), E230 (*atg16l1*^{E230}) and E226 mice (*atg16l1*^{E226}). E230 mice were similar to control mice whereas E226 mice were significantly smaller in size. Scale bar 1cm. **B.** Body weights recorded at regular intervals were plotted as growth curve showing growth lag in E226 mice compared to control and E230 mice. No growth defect was observed in E230 mice and they were comparable to littermate control mice. n = 11 and 6 for E230(*atg16l1*^{E230}) and control (ATG16L1), respectively; n = 11 and 8 for E226 (*atg16l1*^{E226}) and control, respectively. Data across control mice were pooled. Statistical analysis was done by unpaired t test. Error bars represents ±SEM. ****-P < 0.0001.

aggregates. Further liver damage markers such as alkaline phosphatase, aspartate aminotransferase (AST), alanine aminotransferase/ glutamic pyruvic transaminase (ALT/ GPT) were increased in the serum. Although these mice had normal function of proteasome machinery in liver, due to lack of autophagy the turnover of long life proteins was decreased (58).

Likewise, livers from E230, E226 and litter mate controls were analysed for gross morphological features like size, weight and appearance. E230 livers were comparable to controls (5% body weight, average weight 1.6 g) whereas E226 livers were larger taking up 11% body weight with average weight of 2.6g (Figure 15A & B). These results are similar to those recorded for mice lacking *Atg7* (58) or *Atg5* in liver (71). Serum analysis showed elevated ALT/ GPT in autophagy defective E226 mice but these enzymes were not raised in E230 mice compared to litter mate controls (Figure 15C).

Status of autophagy was examined in liver lysates of E230, E226 and control mice by looking at levels of autophagy substrate proteins LC3-I and p62/SQSTM1. Results showed high levels of LC3-I and p62/SQSTM1 in E226 liver lysates compared to littermate controls however no such raised levels were detected in E230 liver lysates (Figure 15D). Liver sections of E230, E226 and control mice were therefore examined for the presence of p62/SQSTM1 inclusions. p62/SQSTM1 inclusions were obvious in E226 but were not observed in E230 mice or littermate controls (Figure 15E). To further investigate the hepatomegaly, liver sections were examined for hepatocyte swelling as shown in liver specific *atg7*^{-/-} mice (58). Measurement of hepatocyte circumference of H & E stained liver sections revealed large hepatocytes (>2 fold) in E226 livers as compared to E230 and controls (Figure 16A). Also unlike Komatsu et al (58) large number of a mitotically active hepatocytes were detected in E226 livers sections upon immunostaining with anti Ki67/MKI67 antibody (Figure 16B). The numbers of Ki67 positive hepatocytes in E230 and control livers were comparable but much less (<4 fold) than E226 livers (Figure 16B). These liver conditions correlated with hepatocellular hypertrophy. Also, it explains that hepatomegaly in autophagy deficient E226 mice is because of hepatocytes proliferation and hepatocyte swelling. Liver inflammation was analysed by

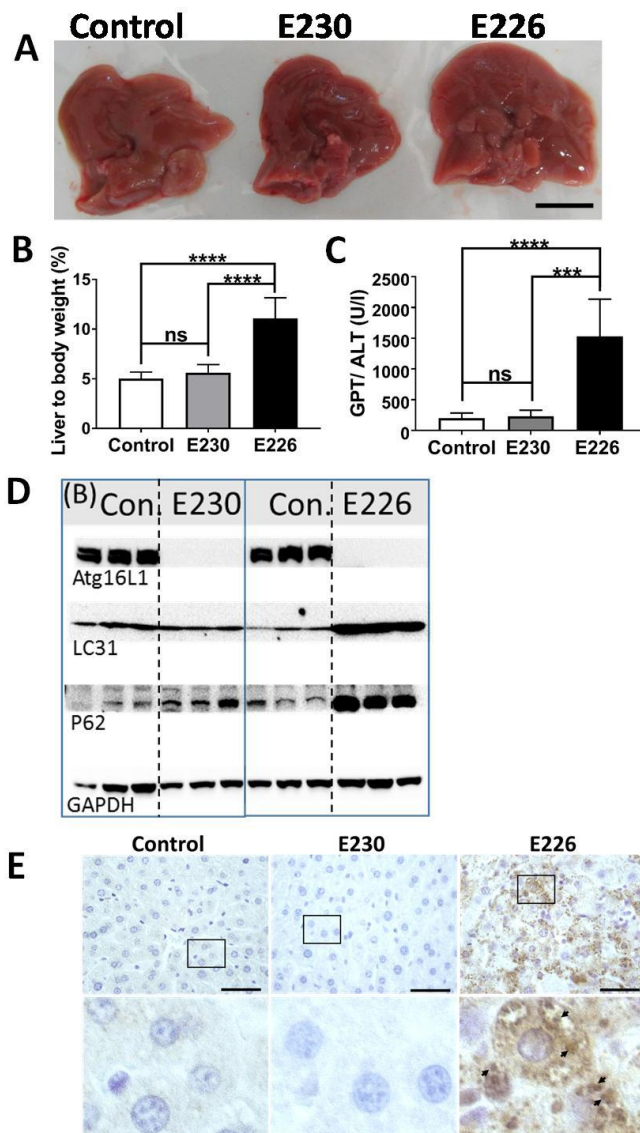


Figure 15: Role played by WD domain in maintaining liver homeostasis: A. Representative picture of livers from 2-3 months old control, E230 and E226 mice showing morphology. E226 livers were larger in size compared to E230 and control livers. E230 and control livers appeared similar. Scales bar 1cm. **B.** Percentage of liver to body weight ratios for 2-3 month old mice were plotted. E226 mice weigh nearly twice as much as control and E230 livers indicating hepatomegaly in E226 livers. Weights of E230 and control livers were comparable. E230 n = 9, control n = 8; E226 n = 9, control n = 7. **C.** Serum levels of liver enzyme ALT/GPT were measured in 2-3 month old mice and represented as bar graph. ALT/GPT levels in E230 and control serums were similar whereas the levels were nearly 5 fold higher in E226 serums indicated liver damage in E226 mice. E230 n = 7, control n = 5; E226 n = 5, v control n = 5. **D.** Liver lysates from 3 different 2-3 month old mice were examined for autophagy substrate proteins. Status of p62 and LC3-I was comparable in E230 and control mice whereas these levels were high in E226 livers. Full length ATG16L1 was detected in control lysates but not in E230 and E226 lysates. **E.** Liver sections from 2-3 month old control, E230 and E226 mice were stained for p62 and a representative image is shown. Control and E230 liver sections didn't stain for p62 whereas E226 liver sections showed multiple inclusions as highlighted in the enlarged lower panel. Arrows indicate p62 inclusions. In all figures data from littermate controls for E230 and E226 were pooled. Statistical analysis was done by unpaired t test. Error bars represents \pm SEM. ****-P < 0.0001, ***-P < 0.001; ns, non-significant. Image magnification 40X, scale bars: 50 μ m.

immunostaining with anti Cd11b/ITGAM antibody specific for monocytes/ macrophages. The high staining of Cd11b (~7 fold against control, ~3 fold against E230) in E226 liver indicated increased infiltration of macrophages compared to E230 and littermate controls (Figure 16C) indicating liver inflammation in E226 mice. Slightly higher (>2-fold) macrophage infiltration was seen in E230 livers compared to their littermate controls indicating raised inflammation and a possible role of LAP in preventing liver inflammation (Figure 16C).

In summary, above results confirm that livers of E230 mice appear and weigh like their littermate controls and didn't show cell swelling or damage-induced cell proliferation (Figures 15A,B & 16A,B). E226 mice, on the other hand, had hepatomegaly, displayed damage induced cell proliferation, cell swelling and hence were similar to liver specific *atg7*^{-/-} mice (58) (Figures 15A,B & 16A,B). Although only slightly higher levels of immune cell infiltration were seen in E230 livers, it was much less compared to E226 livers (Figure 16C).

In another study, Takamura et al (71) generated mice (*Atg5*^{F/F};CAG-Cre) with mosaic deletion of *Atg5* in liver, muscle, brain and heart. These mice showed severe hepatomegaly at 6 months and developed multiple small benign tumours at the age of 9 months, only in liver but not in other organs. These tumours grew in size and number and covered the whole liver in 19 months.

Hepatocytes only from tumour areas showed autophagy defects in the form of appearance of ubiquitin positive protein aggregates and p62 inclusions. These cells also showed signs of increased oxidative stress, DNA damage and accelerated cell proliferation, considered as hallmarks of tumorigenesis. Takamura et al (71) further analysed liver specific *Atg7* deficient mice (*Atg7*^{F/F}; Alb Cre) made by Komatsu et al (72) and observed hepatic tumour formation similar to *Atg5*^{F/F};CAG-Cre mice. The size of hepatic tumours detected in *Atg7*^{F/F}; Alb Cre mice reduced upon simultaneous deletion of p62 (*Atg7*^{F/F}; Alb Cre; *p62*^{-/-}) which pointed towards a role of p62 in tumour formation and progression. According to previous reports (73, 74) p62 inclusions trap and inactivate oxidative stress regulator protein Keap1 which leads to activation of transcription factor Nrf2. Accumulation of

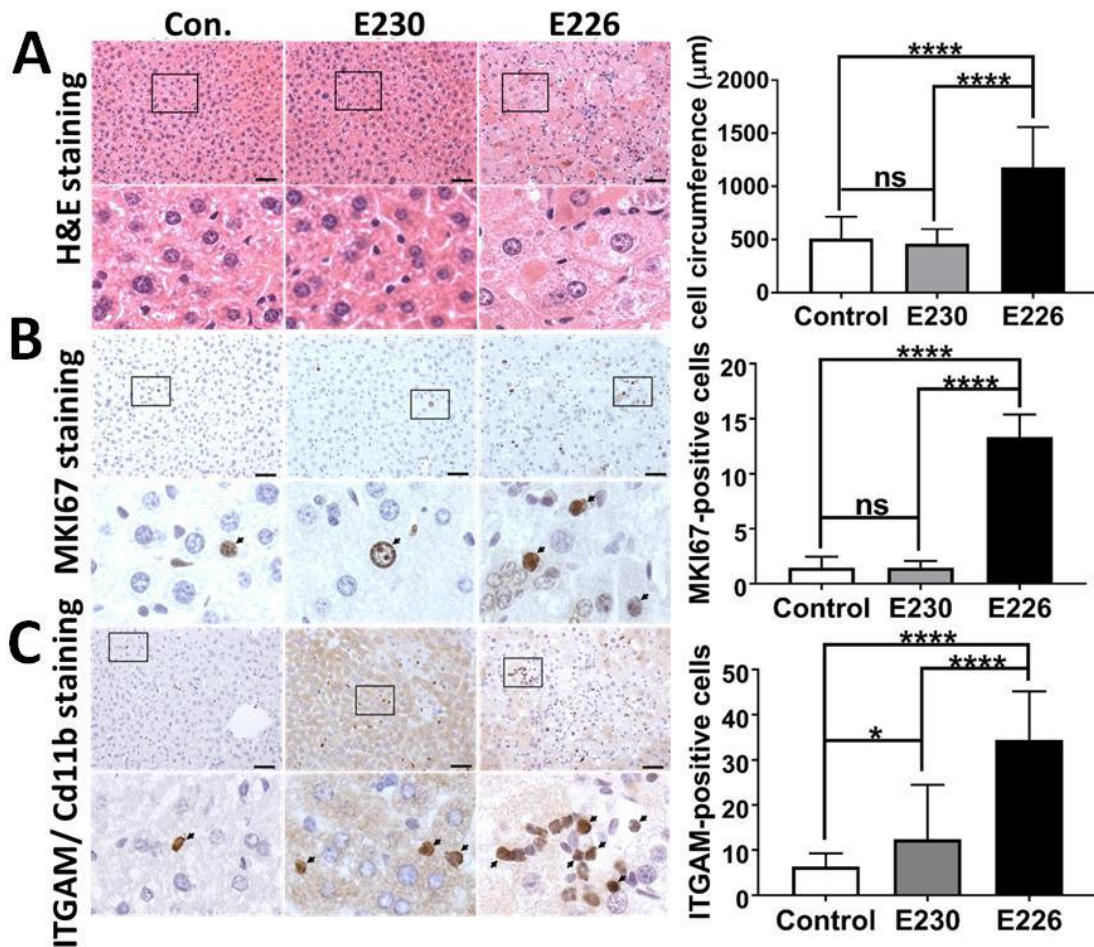


Figure 16: Role of WD domain in preventing hepatomegaly and liver inflammation: A. Liver sections from control, E230 and E226 mice were stained with hematoxylin and eosin followed by examining under microscope and a representative image is shown. The circumference of hepatocytes were measured and plotted as bar graphs. Size of hepatocytes in control and E230 liver sections were comparable whereas E226 hepatocytes were nearly twice larger in size as highlighted in enlarged lower panel, representing cell swelling. **B.** Liver sections were examined for proliferating hepatocytes by staining for MKI67/Ki67. Ratios of number of Ki67 positive nuclei to total number of nuclei present in the 5 different fields were used for the plot. Normal levels of Ki67 positive nuclei were detected in control and E230 livers whereas nearly 7 fold increased staining was observed in E226 livers, as shown by arrows in lower enlarged panel, indicating damage induced cell proliferation. **C.** Liver sections were stained for Cd11b/ITGAM to examine for macrophage infiltration and a representative image is shown. Numbers of positive cells across 5 different fields were used for the plot. Nearly 2 fold higher levels of Cd11b staining was observed in E230 compared to control mice whereas the levels were more than 10 fold higher in E226 livers, as shown by arrows in lower enlarged panel, indicating liver inflammation. Livers from 2-3 months old mice were used in all the above experiments. n = 3 for all the strains in all the above experiments. Data across littermate control mice for E230 and E226 were pooled. Statistical analysis was done by unpaired t test. Error bars represent \pm SEM. ****-P < 0.0001, *-P < 0.1. Magnification 20X, scale bars: 50 μ m.

Keap1 and activation of Nrf2 responsive factor Nqo1 (NAD(P)H dehydrogenase quinone 1) was noticed in *Atg7^{F/F}; Alb Cre* mice but not in *Atg7^{F/F}; Alb Cre; p62^{-/-}* mice. These data suggest that accumulation of p62 due to defective autophagy has role in tumour formation and progression. Moreover, only benign tumours were observed in these mice which didn't get cancerous perhaps because of autophagy deficiency. Which suggest that although autophagy has a role in tumour suppression, once the tumours are formed it may play role in cancer development. Although p62 inclusions were observed in E226 livers (Figures 15E), no tumours were seen. This may be because E226 mice don't survive more than 7 months which is less than the reported age of 9 months to develop tumours (data not shown).

4.3 Kidney:

On morphological analysis, kidneys from E226 mice appeared smaller (~ 50%) than E230 and control kidneys but when their weights were normalised against whole body weight, the difference was non-significant (Figure 17A-C). When kidney lysates from E230, E226 and control mice were tested for the levels of autophagy substrate proteins, due to lack of autophagy, raised levels of LC3-I and p62/SQSTM1 were observed in E226 but not in E230 and control mice (Figure 17D-F). The presence of p62/SQSTM1 inclusions was therefore tested in kidney sections via immunostaining and figure 17G shows distinct p62/SQSTM1 inclusions in autophagy deficient E226 kidneys. However, such inclusions were not noticed in E230 and control kidneys (Figure 17G). As published earlier, mice with lack of non-canonical autophagy/ LAP in myeloid cells, due to removal of Rubicon, showed deposition of immune complexes (IgG and C1q) in kidney glomeruli and other symptoms resembling SLE(62) however no such depositions were detected upon immunostaining for IgG autoantibodies in kidney sections of LAP deficient E230 or autophagy and LAP deficient E226 mice (data not shown). No other obvious histological differences were noticed between E230, E226 and control kidneys (data not shown). Although SLE like phenotype in kidney was not observed in E230 or E226 mice, it may develop in later age.

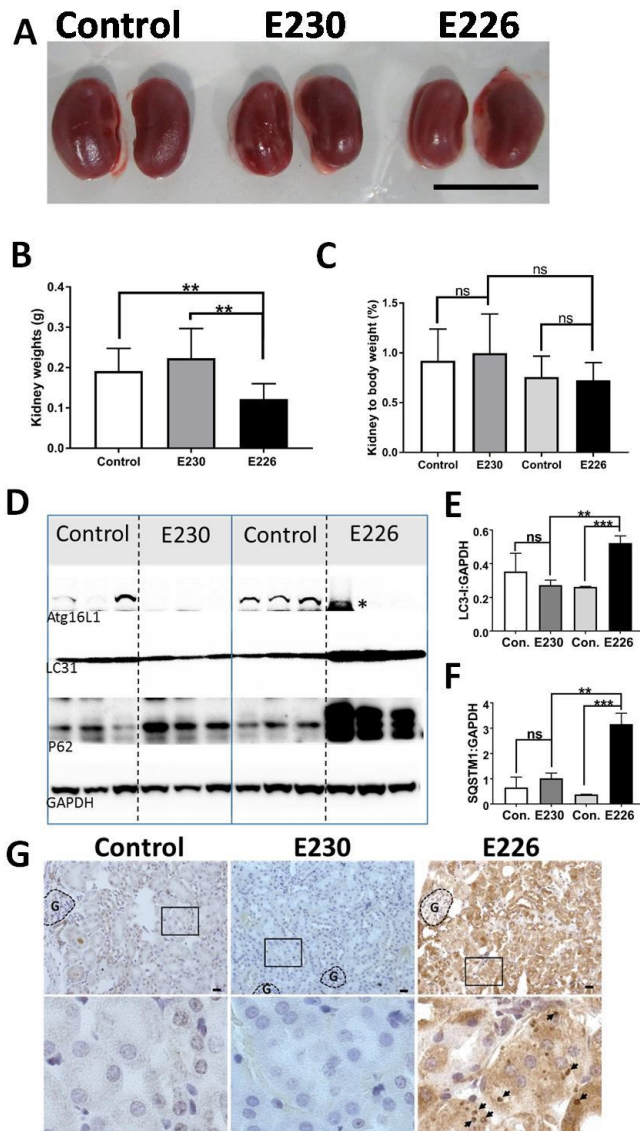


Figure 17: Role of WD domain in maintaining kidney homeostasis: **A.** Representative image comparing size and morphology of control, E230 and E226 kidneys is shown. E226 kidneys appeared smaller than E230 and control kidneys. Scale bar 1 cm. **B&C.** Kidney weights were recorded and plotted as weight and as percentage of ratio of kidney to body weight. E226 kidneys weighed less (E230 n = 8, control n = 8, E226 n = 7, control = 8) but when normalised for whole body weight (E230 n = 9, control n = 8, E226 n = 7, control = 6), there was no significant difference found. **D-F.** Kidney lysates from three different mice were examined for autophagy substrate proteins. Raised levels of LC3-I and p62 were observed in E226 kidney lysate but not in control and E230 kidneys. Upon quantification, ~2 fold higher levels of LC3-I and ~6 fold higher levels of p62 was found in E226, than control and E230 kidneys. **G.** Kidney sections from control, E230 and E226 mice were stained for p62 and a representative image is shown. No p62 staining was seen in control and E230 kidney sections whereas prominent p62 inclusions were detected in E226 kidneys as pointed by arrows in lower enlarged panel. G represents glomerulus. Data from control mice were pooled. Statistical analysis was done by unpaired t test. Error bars represent \pm SEM. ***-P < 0.001, **-P < 0.01; ns, non-significant. Magnification 20X, scale bars: 50 μ m.

4.4 Muscle:

Important role of autophagy in maintenance of muscle homeostasis was shown by Masiero et al in 2009 (75). They generated a muscle specific autophagy deficient mouse by making targeted deletion of *Atg7*. Cultured myofibers from these mice failed to generate autophagosomes upon starvation and contained p62/SQSTM1 aggregates. At 2 months age, although indistinguishable in appearance, the muscle lacking ATG7 displayed various signs of atrophy and myopathy such as: decreased gain of muscle mass with age, loss-of-force production, decrease in myofiber size, vacuolated and centrally nucleated myofibers, muscle loss due to activation of apoptosis, accumulation of damaged mitochondria and sarcoplasmic distension. The loss in force generation was age-dependent as 5 months old mice displayed increased loss in specific force compared to 2 month old mice. *atg7*^{-/-} muscles from these mice also showed different set of morphological features for myopathy upon induction of catabolic conditions of muscle wasting like denervation and fasting. Denervation showed muscle loss, upregulation of several atrophy related genes and features including presence of abnormal myonuclei, accumulation of hematoxylin-positive inclusions and vacuolated areas which were not noticed in muscles from littermate control mice. Interestingly the size of ubiquitin positive p62 inclusions increased upon denervation of *atg7*^{-/-} muscles. Upon fasting similar morphological features of muscle degeneration like hematoxylin-positive inclusions, vacuolated cytosol but smaller sized p62 inclusions were observed in *atg7*^{-/-} but not in control muscles. However, upregulation of atrophy related genes was not observed. Hence, these observations conclude that autophagy plays different important roles in different conditions of muscle loss but was found crucial for maintenance of normal homeostasis in physiological and pathophysiological conditions.

Gastrocnemius muscles from E230 mice appeared and weighed normal (Figure 18A & B). They didn't display any of the abnormalities reported by Masiero et al for *atg7*^{-/-} muscle, and hence were comparable to their litter mate controls. On the other hand gastrocnemius muscles of E226 mice were found significantly smaller than muscles of E230 and control mice indicating muscle wasting

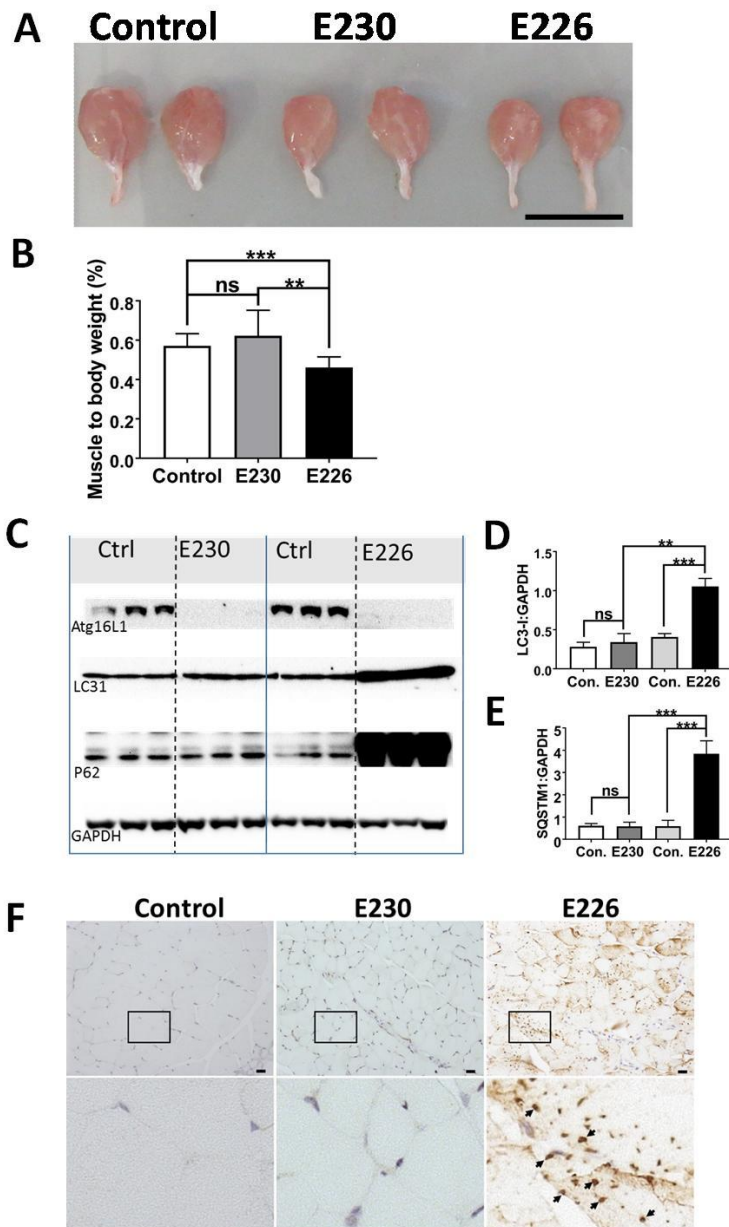


Figure 18: Role of WD domain in maintaining muscle homeostasis: A. The representative image compares the morphology of gastrocnemius muscles of control, E230 and E226 mice. E226 muscles appeared smaller in size compared to control and E230 muscles Scale bar 1 cm. **B.** Muscle weights were recorded and plotted as percentage ratio against whole body weight. Muscles of E230 mice weighed as much as control mice but E226 muscles were significantly lighter indicated muscle wasting. E230 n = 6, control n = 5; E226 n = 8, control n = 6. **C-E.** Muscle lysates from three different controls, E230 and E226 mice were examined for autophagy substrate proteins. Accumulation of LC3-I and p62 was observed in E226 muscles whereas no accumulation was detected in E230 and control mice. Quantification of immunoblots confirmed the same results where ~2 fold higher LC3-I and ~4 fold higher p62 was found in E226 muscles compared to E230 and controls. **F.** Muscle sections were examined for p62 inclusions via immunostaining. No p62 staining was detected in control and E230 muscle sections whereas p62 inclusions were obvious in E226 muscles as pointed out by arrows in the lower enlarged panel. Muscles from 2-3 months old mice were used in all the above experiments. Statistical analysis was done by unpaired t test. Error bars represent \pm SEM. ***- $P < 0.001$, **- $P < 0.01$; ns, non-significant. Magnification 20X, scale bar: 50 μ m.

(Figure 18A & B). Upon western blotting, accumulation of autophagy substrate proteins LC3-I and p62/SQSTM1 was seen in E226 muscle lysates indicating loss of autophagy (Figure 18C-E). E230 and control muscle lysates didn't show LC3-I or p62/SQSTM1 accumulations confirming no defect in autophagy (Figure 18C-E). Further histological analysis showed p62/SQSTM1 aggregation in E226 muscles but not in E230 and control muscles (Figure 18F). Further signs of muscle degeneration in myofibers like, decrease in size, excess vacuole formation and central nucleus etc., were not seen in E230, E226 and control mice up till 3 months of age (data not shown).

4.5 Brain:

The important role of autophagy in protection against neurodegenerative diseases has been emphasized previously. Komatsu *et al* (76) engineered neuron specific autophagy deficient mice by deleting *Atg7* (*atg7^{ff}; nestin-cre*). These mice were comparable to littermate controls at the time of birth but had retarded growth rate and couldn't survive more than 28 weeks. Motor coordination and other behavioural deficits with abnormal limb-clasping reflexes and tremor were recorded. H & E staining of brain sections revealed atrophy of cerebral cortical region and reduction in number of Purkinje and similar cells in cerebellar cortex and hippocampal pyramidal cell layer. Upon immunostaining, brain sections showed increased neuronal damage marker, glial fibrillary acidic protein (GFAP) and increased apoptotic cell death. Although normal activity of proteasome was seen, ubiquitin positive inclusions were detected in the brain sections underlining important role of autophagy in clearance of long lived proteins.

Brains from E230 mice along with littermate controls were examined for some of the above deficits. E230 brains appeared normal and were comparable to their littermate control brains in weights (Figure 19A-C). E226 mice brains looked smaller and weighed less compared to E230 and control mice however when normalised against whole body weight, they showed no significant difference (Figure 19A-C). Further examination of status of autophagy in brain lysates from E230, E226 and control mice was performed via western blotting. The brain lysates from E230 and control mice

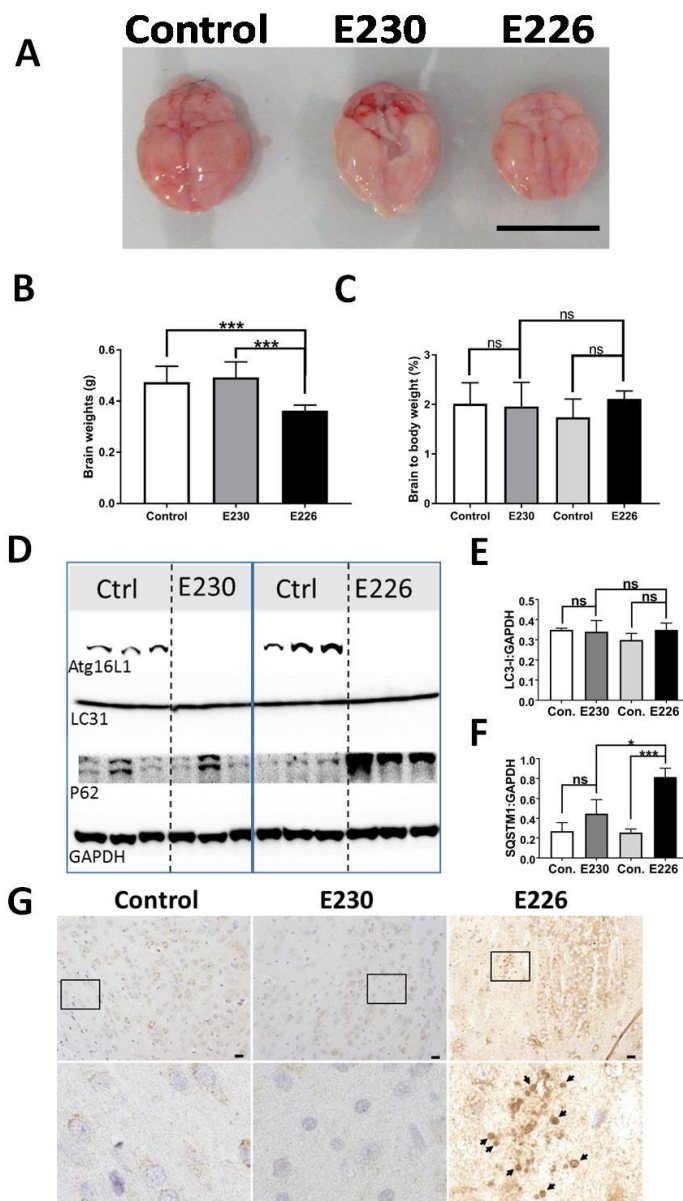


Figure 19: Role of WD domain in maintaining brain homeostasis: **A.** Representative image comparing size and morphology of control, E230 and E226 brains is shown. E226 brains appeared smaller than E230 and control brains. Scale bar 1 cm. **B&C.** Brain weights were recorded and plotted as weight and as percentage of ratio of brain to body weight. E226 brains weighed less (E230 n = 8, control n = 7, E226 n = 7, control = 7) but when normalised for whole body weight (E230 n = 8, control n = 9, E226 E226) n = 6, control = 5), there was no significant difference found. **D-F.** Brain lysates from three different mice were examined for autophagy substrate proteins. Raised levels of p62 were observed in E226 brain lysate but not in control and E230 brains. Interestingly, LC3-I levels were comparable across brains lysates of all the three genotypes. Upon quantification, ~4-fold higher levels of p62 was found in E226, than control and E230 brains. **G.** Brain sections from control, E230 and E226 mice were stained for p62 and a representative image is shown. No p62 staining was seen in control and E230 brain sections whereas prominent p62 inclusions were detected in E226 brain sections as pointed by arrows in lower enlarged panel. Brains from 2-3 months old mice were used in all the above experiments. Data from control mice were pooled. Statistical analysis was done by unpaired t test. Error bars represents \pm SEM.***-P < 0.001, *-P < 0.1; ns, non-significant. Magnification 20X, scale bars: 50 μ m.

didn't show accumulation of LC3 and p62/SQSTM1 upon immunoblotting (Figure 19D-F). On contrary, E226 brain lysates showed ~4 fold higher levels of p62/SQSTM1 indicating defect in autophagy (Figure 19D-F). Interestingly, unlike other peripheral tissues, LC3-I levels were not raised in the brain lysates of E226 mice and were comparable to their littermate control brain lysates (Figure 19D-F). In the next step, brain sections of E230, E226 and control mice were investigated for the presence of p62/SQSTM1 inclusions. Brain sections from E230 and control mice didn't stain for p62/SQSTM1 indicating a lack of inclusions (Figure 19G) and functional autophagy. E226 brain sections, similar to *atg7*^{-/-} mice, were full of p62/SQSTM1 inclusions indicating lack of autophagy (Figure 19G)(76). In spite of showing no obvious behavioural or motor coordination defects, some E230 mice developed head tilt (data not shown) which suggested there may be an abnormality in balance origination in the inner ear.

4.6 Summary & discussion:

As seen in morphological, behavioural, immunoblot and histological analysis of E230 and control mice, in liver, kidney, muscle and brain, loss of WD domain (and hence LAP) didn't affect the status of autophagy and homeostasis. Slightly raised level of macrophages indicated liver inflammation (Figures 15-19) and possible role of LAP in limiting inflammation in liver. On the other hand E226 mice due to lack of autophagy showed morphological and behavioural abnormalities with severely disturbed tissue homeostasis (Figures 15-19) mirroring the ones reported by Komatsu *et al*(58), Masiero *et al*, (75), Komatsu *et al*, (76) and Yoshi *et al* (77). Surprisingly, normal levels of LC3-I in E226 brain lysates pointed towards the active status of autophagy in brain.

Chapter 5

Analysis of ATG16L1 complex formation in liver and brain

Autophagy is required for the neonatal survival of mice (57, 77). At the time of birth, mice (and most mammals) undergo a striking starvation because of discontinuation of trans-placental nutrition supply. This starvation period ends with the supply of mother's milk. It is thought that autophagy allows mice to survive post-natal starvation by providing amino acids from protein degradation. The precise role played by autophagy remains controversial as when compared with littermate control, *atg5^{-/-}* mice died quickly after birth. Upon post mortem analysis, *atg5^{-/-}* pups had low serum amino acids and no milk in stomach. This suggested that postnatal starvation may result from a sucking defect. The data in the previous chapters has shown that the E226 mice generated in this study are defective in autophagy but survive post-natal starvation (Figures 12A, 13A,B & 14A,B). They grew more slowly than littermate controls but survived for 7 months (Figure 14B). It was therefore interesting to consider why the E226 mice survive but *atg5^{-/-}* mice die after birth.

During the course of this PhD Yoshii et al (77) rescued *atg5^{-/-}* mice from neonatal lethality by restoring ATG5 expression in neurons. These mice survived for 6-8 months but, as seen for E226 mice, had several systemic defects characteristic of loss of autophagy. Similarly, autophagy and LAP deficient E226 mice were small, weak, non-fertile, had disturbed tissue homeostasis and lived for maximum 7 months. These similarities suggested that E226 mice may have a low level of autophagy in neurons. This was supported by the observation that levels of LC3-I in the brain lysates of E226 mice were similar to littermate controls and were not elevated as seen in peripheral tissues (Figure 19D& E). Autophagy requires the assembly of a multimeric ATG12-ATG5-ATG16L1 complex which associates with WIPI2 through the E230 and E226 residues in ATG16L1. E226 contains glutamate 226 and may associate weakly with WIPI2 and this may be sufficient for autophagy in brain, but not

peripheral tissues. Gel filtration chromatography was therefore used to determine the sizes of ATG16L1 complexes in lysates from brain and liver, and determine if they contained WIPI2.

5.1 Calibration of gel filtration column: Gel filtration separates proteins according to size with larger proteins eluting in early fraction (Figure 20A). The gels were calibrated by following the elution of marker proteins of known size. The ENrich™ SEC 650 column was calibrated with molecular size markers 29-700 kDa (Figure 20B). Figure 20B shows that there was a linear relationship between protein size and elution volume and that the column would be able to resolve the size of ATG16L1 complexes between 29 kDa and 700 kDa.

5.2 Analysis of liver lysates: The analysis of liver lysates from control mice showed elution of full length ATG16L1, seen as a 66 kDa band, on western blot of fractions corresponding to a broad size range (600-150 kDa) (Figure 21A & B). These fractions also contained ATG12-ATG5 (~ 52 kDa) and WIPI2 (49 kDa) (Figure 21A & B). This confirmed the formation of a large ATG16L1 complex and indirect evidence for interaction with ATG5-ATG12 and WIPI2 to propel autophagy. E230 liver lysates showed slightly slower elution of ATG16L1 suggesting a smaller size between 400-150 kDa (Figure 21A). There was co-elution with ATG12-ATG5 but only faint signal for WIPI2 was detected in high molecular weight fractions (400 kDa) containing ATG16L1 (Figure 21A). This suggests that smaller sized ATG12-ATG5-ATG16L1 complex forms in E230 mice with possibly weak interactions with WIPI2 but the immunoblot analysis (Figure 15D) presented in chapter 4 showed that this is still able to carry out autophagy. E226 liver lysates, similar to E230, showed ATG16L1 in later fractions along with ATG12-ATG5 but WIPI2 was not shifted to higher molecular size (Figure 21A). This suggested that the ATG16L1 complex in the liver lysates of E226 mice has very weak interaction with WIPI2. This would explain lack of autophagy in peripheral tissues and reconfirm the previously mentioned importance of glutamate residue at 230 position (E230) for WIPI2 binding and its role in carrying out autophagy (42) (Figures 8A,C&9D).

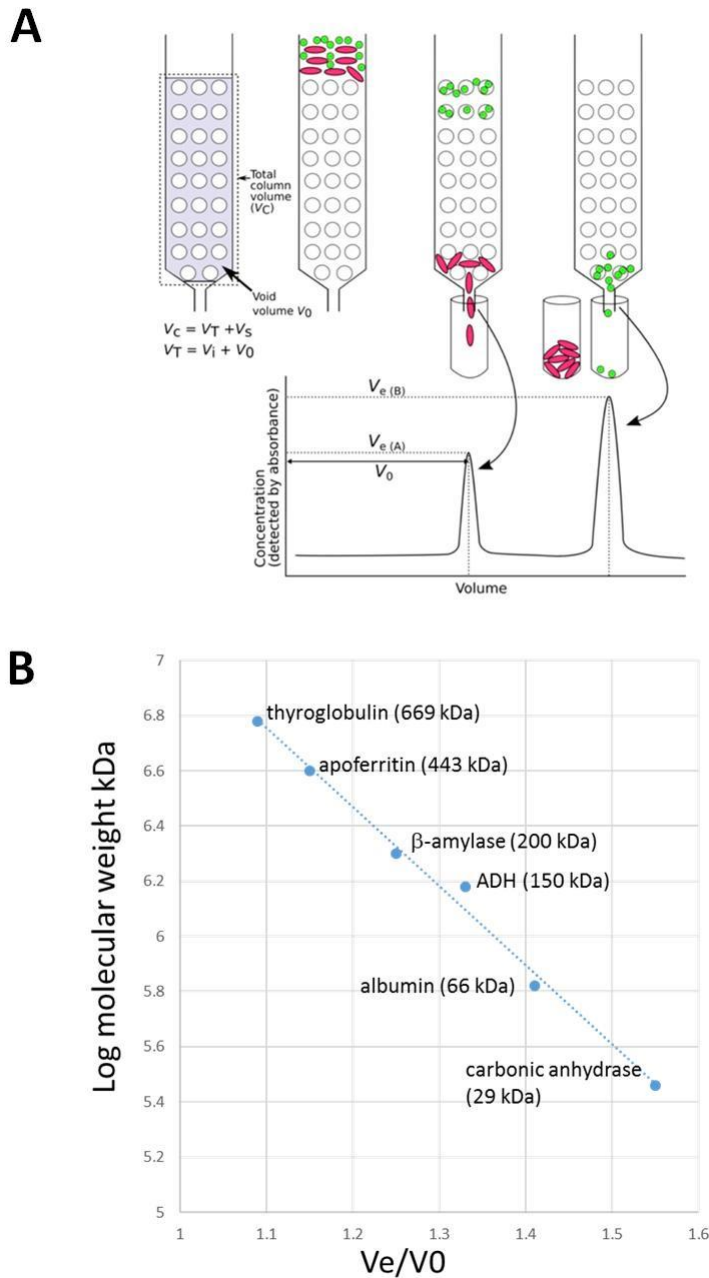


Figure 20: Calibration of gel filtration column: A. The graphical representation of gel filtration chromatography process and principle shown. The column is filled with porous beads and loaded with a mixture of two molecules A (pink and elongated) and B (green and round). The column hinders the movement of the smaller molecule because it can pass through pores of column beads and takes longer to elute. The larger elongated molecule cannot enter pores and elutes quickly. The elution peaks represent elution volumes (V_e) of A ($V_{e(A)}$) and B ($V_{e(B)}$). Due to its size and complete exclusion from beads, elution volume of A ($V_{e(A)}$) represents void volume (V_0). **B.** The plot represents linear relationship between ratios of elution volume to void volume (V_e/V_0) and log of molecular weights of standard proteins ranging 29 kDa-669 kDa. This plot was employed in the calculations of molecular weights of different fractions.

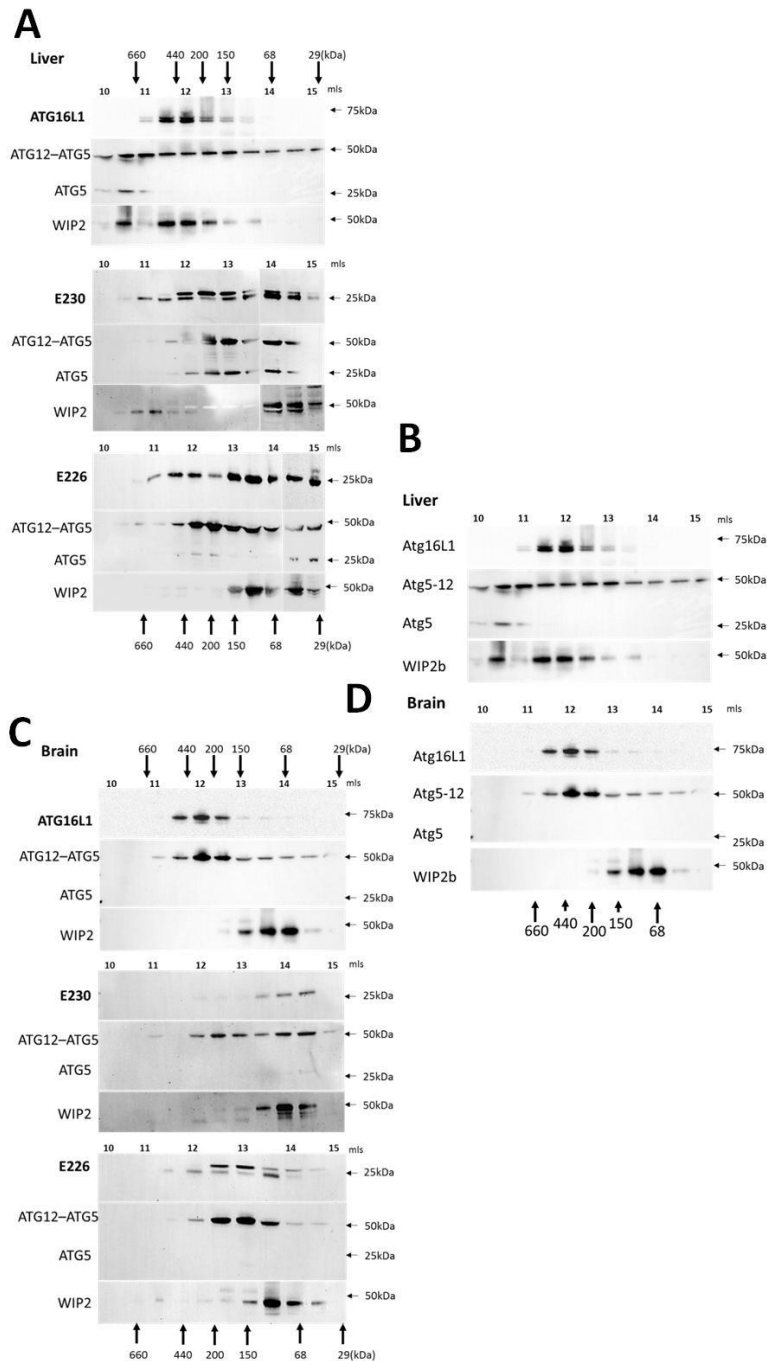


Figure 21: Analysis of ATG16L1 complex in liver and brain: **A & B:** Western blot analysis of liver lysates after gel filtration showed elution of ATG16L1 in 150-700kDa range in control, E230 and E226 livers. While ATG12-ATG5 and WIP2 were detected in the same range in control lysates, E230 lysates showed movement of ATG12-ATG5 towards lower molecular weight with faint band of WIP2 indicating weaker interaction. E226 lysates like E230 lysates showed migration of ATG12-ATG5 towards lower range but didn't show WIP2 in that range indicating no interaction. **C & D:** Column purified brain lysates also showed similar pattern of co-purification of ATG16L1 and ATG12-ATG5 in higher molecular weight range for controls but migration towards lower range in E230 and E226 brain lysates. Interestingly WIP2 purification pattern was different from liver in all the three strains and it was restricted to lower molecular weight range indicating a different interaction pattern in brain. **B&D** compare the difference in WIP2 pattern in the control liver and brain lysates.

5.3 Analysis of brain lysates: Analysis of brain lysates from control, E230 and E226 mice showed that ATG12-ATG5-ATG16L1 conjugate follows a similar pattern as seen in liver lysates, but it was not possible to detect movement of WIPI2 to high molecular weight fractions (Figure 21C & D). Figure 21B and D together compare the patterns of elution of ATG16L1, ATG12-ATG5 and WIPI2 in control liver and brain lysates highlighting the unusual elution of WIPI2 only in lower molecular weight fractions (150-65 kDa) unlike seen in liver lysates (600-150kDa). This suggested that the WIPI2 interaction with ATG12-ATG5-ATG16L1 complex maybe weak in brain and that the weak interaction that might occur for E226, are sufficient to allow a low level of autophagy in the brain of E226 mice leading to their survival during the post-natal period.

5.4 Discussion: The gel filtration analysis showed that full length ATG16L1 forms 600-300kDa complex in brain and liver (Figure 21A-D). In absence of WD domain, E230 and E226 tissues also had many intermediate sized 400-50kDa complexes which is consistent with the previously published results (69). Initial gel filtration based molecular size calculations suggested that an octamer of ATG16L1 binds to ATG12-ATG5 conjugate (69). A subsequent analysis of ATG12-ATG5-ATG16L1 complex by sucrose density sedimentation revealed dimer of ATG16L1 as an interactor to ATG12-ATG5 conjugate (78). This can possibly happen if ATG16L1 makes an elongated conformation because of which it can get early elution from the size exclusion chromatography. In spite of differences in the size of formed complexes, WIPI2 interaction was seen in all of them (Figure 21A-D). Due to presence of glutamate at 226 and 230 positions, the complete interaction of WIPI2 with full length ATG16L1 and ATG16L1^{E230} formed a functional complex capable to power autophagy, in liver, but not in case of ATG16L1^{E226} where loss of E226 formed non-functional complexes (Figure 21A-D).

E226 mice which lacked autophagy and LAP were weak, small, and infertile (Figure 14A). They had slower growth rate and showed disturbed homeostasis in liver, kidney, muscle and brain (Figures

14B-19). These mice resembled *Atg5*^{-/-} used by Yoshii et al (77). Unlike previously showed autophagy null mice by deletion of *Atg3*, *Atg5*, *Atg12*, *Atg16L1*, E226 mice survived neonatal lethality imposed by starvation generated due to loss of placental nutrient supply (57-61). This can be possible because of additional function provided by ATG16L1^{E226} which was absent in other autophagy null mice. As seen in the gel filtration results that ATG16L1^{E226} can form complex with ATG12–ATG5 which may have weak E3 ligase like activity to carry out low level of background autophagy in brain (Figure 21C & D). This was supported by further evidences of lesser p62/SQSTM1 inclusions in E226 MEFs compared to ATG16L1 knock out MEFs (Figure 12A). As shown by Yoshii et al (77), restoration of autophagy in the brain of an autophagy null mice helped it to survive neonatal lethality, the process of autophagy in brain turns out to be critical compared to other tissues and hence may happen differently. This was confirmed by observation where autophagy deficient E226 brain lysates showed normal levels of LC3-I comparable to their littermates (Figure 19D & E). Also the gel filtration analysis displayed a unique pattern of WIPI2 interaction with ATG12–ATG5-ATG16L1 complex in brain tissue compared to liver (Figure 21 B & D). These results all together can be used to conclude that E226 mice maintained a small amount of autophagy in brain which helps them survive post birth starvation although the same was not true in other tissues which results in loss of homeostasis in liver, kidney, muscles and brain (Figures 15-19).

Chapter-6

Cytokine analysis

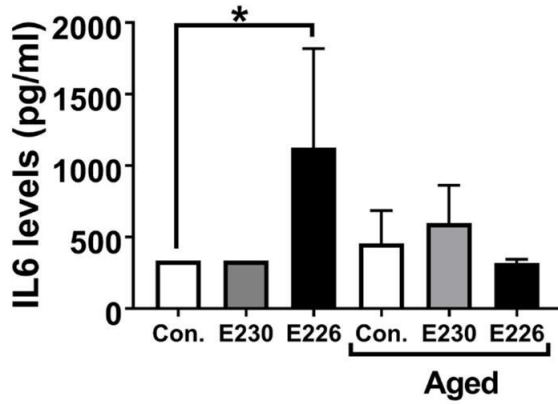
Cytokines are small extracellular messenger molecules (mostly glycoproteins) which act as bridge between innate and adaptive immune components to remove invading pathogen or overcome a tissue damage. Upon pathogen entry or tissue damage, immune cells like macrophages or helper T cells release cytokines which can perform various functions based on their interaction with the subsequent target immune cells. Based on their effect, cytokines can be of proinflammatory (IL-1 β , IL-8, and IFN- γ) or anti-inflammatory (IL-4, IL-10, and IL-13) type. This process is tightly regulated as an improper cytokine response can lead to inflammatory disorder.

Macrophages play an important role in the removal of dead cells and cells dying through apoptosis by phagocytosis. These internalised dead cells are then quickly processed for degradation in lysosome via LC3-associated phagocytosis (LAP). This process of clearing apoptotic or dead cells by macrophages is called "efferocytosis". Failure in efferocytosis triggers inflammatory cytokine response. Work published during the course of this thesis by Martinez et al (50) described a mouse deficient in RUBICON/RUBCN in all tissues. In this report, RUBICON was shown as an essential player for LAP signalling but not autophagy as *rubcn*^{-/-} mice displayed active autophagy but defective LAP. RUBICON as part of class III PI3P kinase complex, facilitates VPS34 activity and sustained Ptdins3P presence on LAPosomes. RUBICON also helps in recruitment as well as stabilisation of NOX2 complex required for generation of reactive oxygen species needed for LAP but not for autophagy. Hence *rubcn*^{-/-} mice were generated to study the LAP defect in presence of autophagy. These mice showed raised serum cytokine (G-CSF, IL1- α , IL1- β , IL-6 & KC) levels upon *Aspergillus fumigatus* infection. Further Martinez et al (62) generated another mouse where targeted deletion of RUBICON/RUBCN in myeloid cells was used to generate a mouse defective in LAP. Work with the *rubcn*^{-/-} mouse has demonstrated that LAP-deficient mice showed accumulation of dead and apoptotic cells in tissues

and in the cytoplasm of macrophages. These dead cells which are present in circulation, trigger immune responses like secretion of pro-inflammatory cytokines and production of autoantibodies (mostly against nuclear antigens) and leads towards the development of SLE. Although considered as “immunologically silent process”, efferocytosis triggers immune signalling for the production of anti-inflammatory cytokines to prevent tissue damage.

The serum of young (8-12 weeks) and aged (20-24 weeks) E230 (LAP^{-/-}), E226 (autophagy^{-/-} & LAP^{-/-}) with littermate control mice were therefore tested for the presence of autoantibodies and cytokines. It was not possible to detect anti-nuclear autoantibodies (data not shown) but raised levels of proinflammatory IL6 and CCL2/MCP1 were detected in E226 mice and these raised levels were absent from E230 and control mice (Figure 22). Comparable serum levels of IL1B, IL12 (p70), IL13, and TNF/TNF- α were found in E230, E226 and control mice (data not shown). Therefore, the complete LAP defective E230 mice did not appear to show any pro-inflammatory and autoimmune conditions displayed by macrophage specific LAP^{-/-} mice lacking RUBCN. Based on above observations it seems that systemically, autophagy but not LAP plays key role in the regulation of inflammatory response against infection or tissue damage.

A



B

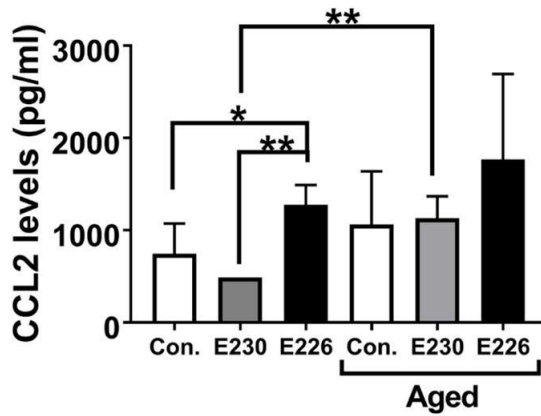


Figure 22: Role of WD domain on cytokine levels: Serum cytokine levels from young (2-3 months) and aged (~24 months) mice were analysed via LUMINEX assay system. **A.** Nearly two fold increase in the serum levels of IL6 was observed in young E226 mice compared to control mice but not in young E230 mice. No significant difference was observed in IL6 levels in aged mice of all three genotypes. **B.** Similarly, significantly higher levels of CCL2 were seen in young E226 mice serums compared to E230 and control mice. The levels of CCL2 were increased in aged E230 mice but not in aged controls and E226 mice serums.

Chapter-7

Discussion:

The WD40 domain contributes to more than half the amino acids of ~66 kDa ATG16L1 in higher eukaryotes like nematodes, insects, plants and humans. The ATG16 of yeast cells doesn't have WD domain yet they can activate autophagy (Figure 7A). Similarly, the WD domain is not required for autophagy in higher eukaryotes (67). This suggests that the WD domain has been added to ATG16L1 during evolution to operate in pathways other than canonical autophagy. The work in this thesis and the work of others (Fletcher, Martinez etc.) shows that the WD domain is required for non-canonical autophagy pathways that monitor the uptake of extracellular material by phagosomes, endosomes and macropinosomes. This allows unwanted external material and pathogens to be removed quickly to lysosomes for degradation. Targeting to lysosomes involves recruitment of LC3 to the endo-lysosome compartments and cells do this by co-opting the proteins used to conjugate LC3 to autophagosomes during canonical autophagy.

Fibroblasts and macrophages isolated from E230 mice couldn't activate LAP which confirmed the results of previous report stating that WD domain is required for several non-canonical autophagy like pathways which recruit LC3 on to endocytic compartments (Figure 13C) [61]. These compartments can be macropinosomes, phagosomes containing latex beads, dead cells or pathogens, swollen endosomes due to monensin or combination of ammonium chloride with vacuolating toxin A (of *Helicobacter pylori*) treatment. Loss of WD domain also hampered the deposition of LC3 on endosomes targeted by proton channel encoded by influenza virus (67). Furthermore, WD domain was also proved to be important in processes like secretion of TNF, IL1 β by dendritic cells in response to CLEC4N/ Dectin2 signalling (79) and also reduced antigen presentation (67).

WD domain forms a complex of 7 bladed β propellers and known for providing a scaffold/ platform for protein interaction (Figure 7C). The loss of function studies described in [61] suggest that the protein interaction platform provided by WD domain is critical for ensuring the quality control of endocytic pathways ensuring quick removal of damaged material entering cells by endocytosis or endosomes/phagosomes containing pathogens or dead cells. These important functions must be the reason for the evolution of this large domain at the C terminus of ATG16L1. Moreover, the same can be further strengthened by the findings confirming interaction of WD domain of ATG16L1 with NOD like receptors (NLRs) (80), MEFV/TRIM20 (25), TMEM (81) and EVA1A/TMEM166 (82) which are important for pathogen recognition.

Mice having conditional KO of LAP in phagocytic cells (macrophages, neutrophils, monocytes) by Lys-Mcre driven loss of RUBCN or CYBB/NOX2 grew slowly and later developed SLE (50, 62). In contrast the E230 mice which lack LAP, described in this thesis, grew normally and over the time frame tested, did not develop obvious SLE (Figure 14A & B). This maybe because the E230 mice have systemic loss of LAP and may have compensated for loss of LAP in phagocytic cells. In other words, inactivation of LAP via removal of WD domain or by deletion of RUBCN and CYBB/NOX2 might happen through different mechanisms. In the next step it will be interesting to see if WD domain interacts with RUBCN or UVRAG or components of CYBB/ NOX2 complex. In spite of lacking a very important function of pathogen removal and maintenance of quality of endosomal vesicles, the E230 mice with systemic loss of LAP didn't show any obvious abnormality and had intact tissue homeostasis (Figures 14-19). Only in few cases E230 mice developed head tilt which might be because of infection in the internal ear due to lack of LAP but needs further investigation (data not shown).

This thesis only emphasized the role of LAP in tissues that doesn't come in direct contact with microbiota/pathogens which indeed is more important question to address. This study significantly

establishes LAP^{-/-} E230 mice fit for further infection studies and next stage experiments based on bacterial and viral infection will provide key insight about exact in vivo role of LAP.

References:

1. Klionsky DJ, Cregg JM, Dunn WA, Emr SD, Sakai Y, Sandoval IV, et al. A unified nomenclature for yeast autophagy-related genes. *Developmental cell*. 2003;5(4):539-45.
2. Mizushima N. A brief history of autophagy from cell biology to physiology and disease. *Nature cell biology*. 2018;1.
3. Mizushima N, Komatsu M. Autophagy: renovation of cells and tissues. *Cell*. 2011;147(4):728-41.
4. Dikic I, Elazar Z. Mechanism and medical implications of mammalian autophagy. *Nat Rev Mol Cell Bio*. 2018 Jun;19(6):349-64. PubMed PMID: WOS:000432677200006. English.
5. Hamasaki M, Furuta N, Matsuda A, Nezu A, Yamamoto A, Fujita N, et al. Autophagosomes form at ER-mitochondria contact sites. *Nature*. 2013;495(7441):389.
6. Nascimbeni AC, Giordano F, Dupont N, Grasso D, Vaccaro MI, Codogno P, et al. ER-plasma membrane contact sites contribute to autophagosome biogenesis by regulation of local PI3P synthesis. *The EMBO journal*. 2017;36(14):2018-33.
7. Abada A, Elazar Z. Getting ready for building: signaling and autophagosome biogenesis. *EMBO reports*. 2014;15(8):839-52.
8. Nedelsky NB, Todd PK, Taylor JP. Autophagy and the ubiquitin-proteasome system: Collaborators in neuroprotection. *Bba-Mol Basis Dis*. 2008 Dec;1782(12):691-9. PubMed PMID: WOS:000261863500003. English.
9. Pengo N, Agrotis A, Prak K, Jones J, Ketteler R. A reversible phospho-switch mediated by ULK1 regulates the activity of autophagy protease ATG4B. *Nature communications*. 2017;8(1):294.
10. Sánchez-Wandelmer J, Kriegenburg F, Rohringer S, Schuschnig M, Gómez-Sánchez R, Zens B, et al. Atg4 proteolytic activity can be inhibited by Atg1 phosphorylation. *Nature communications*. 2017;8(1):295.
11. Scherz-Shouval R, Shvets E, Fass E, Shorer H, Gil L, Elazar Z. Reactive oxygen species are essential for autophagy and specifically regulate the activity of Atg4. *The EMBO journal*. 2007;26(7):1749-60.
12. Levine B, Kroemer G. Biological Functions of Autophagy Genes: A Disease Perspective. *Cell*. 2019 Jan 10;176(1-2):11-42. PubMed PMID: WOS:000455410800006. English.
13. Kimura T, Jia J, Kumar S, Choi SW, Gu Y, Mudd M, et al. Dedicated SNAREs and specialized TRIM cargo receptors mediate secretory autophagy. *The EMBO journal*. 2017;36(1):42-60.
14. Li F, Xie X, Wang Y, Liu J, Cheng X, Guo Y, et al. Structural insights into the interaction and disease mechanism of neurodegenerative disease-associated optineurin and TBK1 proteins. *Nature communications*. 2016;7:12708.
15. Shim MS, Takihara Y, Kim K-Y, Iwata T, Yue BY, Inatani M, et al. Mitochondrial pathogenic mechanism and degradation in optineurin E50K mutation-mediated retinal ganglion cell degeneration. *Scientific reports*. 2016;6:33830.
16. Silva IA, Conceição N, Gagnon É, Caiado H, Brown JP, Gianfrancesco F, et al. Effect of genetic variants of OPTN in the pathophysiology of Paget's disease of bone. *Biochimica et Biophysica Acta (BBA)-Molecular Basis of Disease*. 2018;1864(1):143-51.
17. Wong YC, Holzbaur EL. Optineurin is an autophagy receptor for damaged mitochondria in parkin-mediated mitophagy that is disrupted by an ALS-linked mutation. *Proceedings of the National Academy of Sciences*. 2014;111(42):E4439-E48.
18. Kitada T, Asakawa S, Hattori N, Matsumine H, Yamamura Y, Minoshima S, et al. Mutations in the parkin gene cause autosomal recessive juvenile parkinsonism. *nature*. 1998;392(6676):605.
19. Mira MT, Alcais A, Van Thuc N, Moraes MO, Di Flumeri C, Thai VH, et al. Susceptibility to leprosy is associated with PARK2 and PACRG. *Nature*. 2004;427(6975):636.
20. Xu L, Lin D-c, Yin D, Koeffler HP. An emerging role of PARK2 in cancer. *Journal of molecular medicine*. 2014;92(1):31-42.

21. Jiang P, Mizushima N. Autophagy and human diseases. *Cell research*. 2014;24(1):69.
22. Cirulli ET, Lasseigne BN, Petrovski S, Sapp PC, Dion PA, Leblond CS, et al. Exome sequencing in amyotrophic lateral sclerosis identifies risk genes and pathways. *Science*. 2015;347(6229):1436-41.
23. van Beek N, Klionsky DJ, Reggiori F. Genetic aberrations in macroautophagy genes leading to diseases. *Biochimica et Biophysica Acta (BBA)-Molecular Cell Research*. 2018;1865(5):803-16.
24. Ellinghaus D, Zhang H, Zeissig S, Lipinski S, Till A, Jiang T, et al. Association between variants of PRDM1 and NDP52 and Crohn's disease, based on exome sequencing and functional studies. *Gastroenterology*. 2013;145(2):339-47.
25. Kimura T, Jain A, Choi SW, Mandell MA, Schroder K, Johansen T, et al. TRIM-mediated precision autophagy targets cytoplasmic regulators of innate immunity. *J Cell Biol*. 2015;210(6):973-89.
26. Heuser J. Changes in lysosome shape and distribution correlated with changes in cytoplasmic pH. *The Journal of cell biology*. 1989;108(3):855-64.
27. Fass E, Shvets E, Degani I, Hirschberg K, Elazar Z. Microtubules support production of starvation-induced autophagosomes but not their targeting and fusion with lysosomes. *Journal of Biological Chemistry*. 2006;281(47):36303-16.
28. Yu L, Chen Y, Tooze SA. Autophagy pathway: Cellular and molecular mechanisms. *Autophagy*. 2018;14(2):207-15. PubMed PMID: WOS:000429594000005. English.
29. Tumbarello DA, Waxse BJ, Arden SD, Bright NA, Kendrick-Jones J, Buss F. Autophagy receptors link myosin VI to autophagosomes to mediate Tom1-dependent autophagosome maturation and fusion with the lysosome. *Nature cell biology*. 2012;14(10):1024.
30. Brandstaetter H, Kishi-Itakura C, Tumbarello DA, Manstein DJ, Buss F. Loss of functional MYO1C/myosin 1c, a motor protein involved in lipid raft trafficking, disrupts autophagosome-lysosome fusion. *Autophagy*. 2014;10(12):2310-23.
31. Takáts S, Pircs K, Nagy P, Varga Á, Kárpáti M, Hegedűs K, et al. Interaction of the HOPS complex with Syntaxin 17 mediates autophagosome clearance in *Drosophila*. *Molecular biology of the cell*. 2014;25(8):1338-54.
32. Jiang P, Nishimura T, Sakamaki Y, Itakura E, Hatta T, Natsume T, et al. The HOPS complex mediates autophagosome-lysosome fusion through interaction with syntaxin 17. *Molecular biology of the cell*. 2014;25(8):1327-37.
33. Chen D, Fan W, Lu Y, Ding X, Chen S, Zhong Q. A mammalian autophagosome maturation mechanism mediated by TECPR1 and the Atg12-Atg5 conjugate. *Molecular cell*. 2012;45(5):629-41.
34. Itakura E, Kishi-Itakura C, Mizushima N. The hairpin-type tail-anchored SNARE syntaxin 17 targets to autophagosomes for fusion with endosomes/lysosomes. *Cell*. 2012;151(6):1256-69.
35. Diao JJ, Liu R, Rong YG, Zhao ML, Zhang J, Lai Y, et al. ATG14 promotes membrane tethering and fusion of autophagosomes to endolysosomes. *Nature*. 2015 Apr 23;520(7548):563-+. PubMed PMID: WOS:000353334500048. English.
36. de Lartigue J, Polson H, Feldman M, Shokat K, Tooze SA, Urbe S, et al. PIKfyve regulation of endosome-linked pathways. *Traffic*. 2009 Jul;10(7):883-93. PubMed PMID: 19582903. Pubmed Central PMCID: PMC2723830.
37. Wang H, Sun HQ, Zhu X, Zhang L, Albanesi J, Levine B, et al. GABARAPs regulate PI4P-dependent autophagosome:lysosome fusion. *Proc Natl Acad Sci U S A*. 2015 Jun 2;112(22):7015-20. PubMed PMID: 26038556. Pubmed Central PMCID: PMC4460452.
38. Cebollero E, van der Vaart A, Zhao MT, Rieter E, Klionsky DJ, Helms JB, et al. Phosphatidylinositol-3-Phosphate Clearance Plays a Key Role in Autophagosome Completion. *Curr Biol*. 2012 Sep 11;22(17):1545-53. PubMed PMID: WOS:000308849900026. English.
39. Nakamura S, Hasegawa J, Yoshimori T. Regulation of lysosomal phosphoinositide balance by INPP5E is essential for autophagosome-lysosome fusion. *Autophagy*. 2016;12(12):2500-1. PubMed PMID: WOS:000390691600019. English.

40. Biazik J, Yla-Anttila P, Vihinen H, Jokitalo E, Eskelinen EL. Ultrastructural relationship of the phagophore with surrounding organelles. *Autophagy*. 2015 Mar;11(3):439-51. PubMed PMID: WOS:000353587600002. English.
41. Karanasios E, Walker SA, Okkenhaug H, Manifava M, Hummel E, Zimmermann H, et al. Autophagy initiation by ULK complex assembly on ER tubulovesicular regions marked by ATG9 vesicles. *Nature Communications*. 2016 Aug;7. PubMed PMID: WOS:000381526400001. English.
42. Dooley HC, Razi M, Polson HE, Girardin SE, Wilson MI, Tooze SA. WIPI2 links LC3 conjugation with PI3P, autophagosome formation, and pathogen clearance by recruiting Atg12-5-16L1. *Molecular cell*. 2014;55(2):238-52.
43. Yu L, McPhee CK, Zheng LX, Mardones GA, Rong YG, Peng JY, et al. Termination of autophagy and reformation of lysosomes regulated by mTOR. *Nature*. 2010 Jun 17;465(7300):942-U11. PubMed PMID: WOS:000278804500041. English.
44. Sanjuan MA, Dillon CP, Tait SW, Moshiah S, Dorsey F, Connell S, et al. Toll-like receptor signalling in macrophages links the autophagy pathway to phagocytosis. *Nature*. 2007;450(7173):1253.
45. Henault J, Martinez J, Riggs JM, Tian J, Mehta P, Clarke L, et al. Noncanonical Autophagy Is Required for Type I Interferon Secretion in Response to DNA-Immune Complexes. *Immunity*. 2012 Dec 14;37(6):986-97. PubMed PMID: WOS:000312575000008. English.
46. Kim JY, Zhao H, Martinez J, Doggett TA, Kolesnikov AV, Tang PH, et al. Noncanonical Autophagy Promotes the Visual Cycle (vol 154, pg 365, 2013). *Cell*. 2013 Oct 24;155(3):725-6. PubMed PMID: WOS:000326571800024. English.
47. Martinez J, Almendinger J, Oberst A, Ness R, Dillon CP, Fitzgerald P, et al. Microtubule-associated protein 1 light chain 3 alpha (LC3)-associated phagocytosis is required for the efficient clearance of dead cells. *P Natl Acad Sci USA*. 2011 Oct 18;108(42):17396-401. PubMed PMID: WOS:000295975300038. English.
48. Florey O, Kim SE, Sandoval CP, Haynes CM, Overholtzer M. Autophagy machinery mediates macroendocytic processing and entotic cell death by targeting single membranes. *Nature cell biology*. 2011;13(11):1335.
49. Huang J, Canadien V, Lam GY, Steinberg BE, Dinauer MC, Magalhaes MA, et al. Activation of antibacterial autophagy by NADPH oxidases. *Proceedings of the National Academy of Sciences*. 2009;106(15):6226-31.
50. Martinez J, Malireddi RS, Lu Q, Cunha LD, Pelletier S, Gingras S, et al. Molecular characterization of LC3-associated phagocytosis reveals distinct roles for Rubicon, NOX2 and autophagy proteins. *Nature cell biology*. 2015;17(7):893-906.
51. Florey O, Gammoh N, Kim SE, Jiang X, Overholtzer M. V-ATPase and osmotic imbalances activate endolysosomal LC3 lipidation. *Autophagy*. 2015;11(1):88-99.
52. Mostowy S, Cossart P. Bacterial autophagy: restriction or promotion of bacterial replication? *Trends Cell Biol*. 2012 Jun;22(6):283-91. PubMed PMID: WOS:000305660600001. English.
53. Cemma M, Brumell JH. Interactions of Pathogenic Bacteria with Autophagy Systems. *Curr Biol*. 2012 Jul 10;22(13):R540-R5. PubMed PMID: WOS:000306379600017. English.
54. Randow F, Munz C. Autophagy in the regulation of pathogen replication and adaptive immunity. *Trends Immunol*. 2012 Oct;33(10):475-87. PubMed PMID: WOS:000309947000001. English.
55. Hubber A, Kubori T, Coban C, Matsuzawa T, Ogawa M, Kawabata T, et al. Bacterial secretion system skews the fate of Legionella-containing vacuoles towards LC3-associated phagocytosis. *Scientific Reports*. 2017 Mar 20;7. PubMed PMID: WOS:000396890700001. English.
56. Choi J, Park S, Biering SB, Selleck E, Liu CY, Zhang X, et al. The Parasitophorous Vacuole Membrane of *Toxoplasma gondii* Is Targeted for Disruption by Ubiquitin-like Conjugation Systems of Autophagy. *Immunity*. 2014 Jun 19;40(6):924-35. PubMed PMID: WOS:000341440200014. English.
57. Kuma A, Hatano M, Matsui M, Yamamoto A, Nakaya H, Yoshimori T, et al. The role of autophagy during the early neonatal starvation period. *Nature*. 2004;432(7020):1032-6.

58. Komatsu M, Waguri S, Ueno T, Iwata J, Murata S, Tanida I, et al. Impairment of starvation-induced and constitutive autophagy in Atg7-deficient mice. *J Cell Biol.* 2005;169(3):425-34.
59. Sou Y-s, Waguri S, Iwata J-i, Ueno T, Fujimura T, Hara T, et al. The Atg8 conjugation system is indispensable for proper development of autophagic isolation membranes in mice. *Molecular biology of the cell.* 2008;19(11):4762-75.
60. Saitoh T, Fujita N, Jang MH, Uematsu S, Yang B-G, Satoh T, et al. Loss of the autophagy protein Atg16L1 enhances endotoxin-induced IL-1 β production. *Nature.* 2008;456(7219):264-8.
61. Malhotra R, Warne JP, Salas E, Xu AW, Debnath J. Loss of Atg12, but not Atg5, in pro-opiomelanocortin neurons exacerbates diet-induced obesity. *Autophagy.* 2015;11(1):145-54.
62. Martinez J, Cunha LD, Park S, Yang M, Lu Q, Orchard R, et al. Noncanonical autophagy inhibits the autoinflammatory, lupus-like response to dying cells. *Nature.* 2016;533(7601):115-9.
63. Joseph J, Ametepe ES, Haribabu N, Agbayani G, Krishnan L, Blais A, et al. Inhibition of ROS and upregulation of inflammatory cytokines by FoxO3a promotes survival against *Salmonella typhimurium*. *Nat Commun.* 2016 Sep 7;7:12748. PubMed PMID: 27599659. Pubmed Central PMCID: 5023958.
64. Novaes RD, Teixeira AL, de Miranda AS. Oxidative Stress in Microbial Diseases: Pathogen, Host, and Therapeutics. *Oxidative medicine and cellular longevity.* 2019;2019:8159562. PubMed PMID: 30774746. Pubmed Central PMCID: 6350582.
65. Duncan SA, Baganizi DR, Sahu R, Singh SR, Dennis VA. SOCS Proteins as Regulators of Inflammatory Responses Induced by Bacterial Infections: A Review. *Frontiers in microbiology.* 2017;8:2431. PubMed PMID: 29312162. Pubmed Central PMCID: 5733031.
66. Bajagic M, Büsing P, Scrima A. Structure of the WD40-domain of human ATG16L1. *Protein Science.* 2017.
67. Fletcher K, Ulferts R, Jacquin E, Veith T, Gammoh N, Arasteh JM, et al. The WD40 domain of ATG16L1 is required for its non-canonical role in lipidation of LC3 at single membranes. *The EMBO journal.* 2018:e97840.
68. Fujioka Y, Noda NN, Nakatogawa H, Ohsumi Y, Inagaki F. Dimeric Coiled-coil Structure of *Saccharomyces cerevisiae* Atg16 and Its Functional Significance in Autophagy. *Journal of Biological Chemistry.* 2010 Jan 8;285(2):1508-15. PubMed PMID: WOS:000273258200070. English.
69. Mizushima N, Kuma A, Kobayashi Y, Yamamoto A, Matsubae M, Takao T, et al. Mouse Apg16L, a novel WD-repeat protein, targets to the autophagic isolation membrane with the Apg12-Apg5 conjugate. *Journal of cell science.* 2003;116(9):1679-88.
70. Klionsky D. Guidelines for the Use and Interpretation of Assays for Monitoring Autophagy (3rd edition) (vol 12, pg 1, 2015). *Autophagy.* 2016;12(2):443-. PubMed PMID: WOS:000373982600022. English.
71. Takamura A, Komatsu M, Hara T, Sakamoto A, Kishi C, Waguri S, et al. Autophagy-deficient mice develop multiple liver tumors. *Genes & development.* 2011;25(8):795-800.
72. Komatsu M, Waguri S, Koike M, Sou Y, Ueno T, Hara T, et al. Homeostatic levels of p62 control cytoplasmic inclusion body formation in autophagy-deficient mice. *Cell.* 2007 Dec 14;131(6):1149-63. PubMed PMID: WOS:000252217100022. English.
73. Komatsu M, Kurokawa H, Waguri S, Taguchi K, Kobayashi A, Ichimura Y, et al. The selective autophagy substrate p62 activates the stress responsive transcription factor Nrf2 through inactivation of Keap1. *Nature Cell Biology.* 2010 Mar;12(3):213-U17. PubMed PMID: WOS:000275054200007. English.
74. Lau A, Wang XJ, Zhao F, Villeneuve NF, Wu TD, Jiang T, et al. A Noncanonical Mechanism of Nrf2 Activation by Autophagy Deficiency: Direct Interaction between Keap1 and p62. *Mol Cell Biol.* 2010 Jul 1;30(13):3275-85. PubMed PMID: WOS:000278626100011. English.
75. Masiero E, Agatea L, Mammucari C, Blaauw B, Loro E, Komatsu M, et al. Autophagy is required to maintain muscle mass. *Cell metabolism.* 2009;10(6):507-15.
76. Komatsu M, Waguri S, Chiba T, Murata S, Iwata J-i, Tanida I, et al. Loss of autophagy in the central nervous system causes neurodegeneration in mice. *Nature.* 2006;441(7095):880-4.

77. Yoshii SR, Kuma A, Akashi T, Hara T, Yamamoto A, Kurikawa Y, et al. Systemic analysis of Atg5-null mice rescued from neonatal lethality by transgenic ATG5 expression in neurons. *Developmental cell*. 2016;39(1):116-30.
78. Fujita N, Saitoh T, Kageyama S, Akira S, Noda T, Yoshimori T. Differential Involvement of Atg16L1 in Crohn Disease and Canonical Autophagy ANALYSIS OF THE ORGANIZATION OF THE Atg16L1 COMPLEX IN FIBROBLASTS. *Journal of Biological Chemistry*. 2009;284(47):32602-9.
79. Lamprinaki D, Beasy G, Zhekova A, Wittmann A, James S, Dicks J, et al. I ϵ 3-associated Phagocytosis is required for Dendritic cell inflammatory cytokine response to gut commensal Yeast *Saccharomyces cerevisiae*. *Frontiers in immunology*. 2017;8.
80. Travassos LH, Carneiro LA, Ramjeet M, Hussey S, Kim Y-G, Magalhães JG, et al. Nod1 and Nod2 direct autophagy by recruiting ATG16L1 to the plasma membrane at the site of bacterial entry. *Nature immunology*. 2010;11(1):55-62.
81. Boada-Romero E, Letek M, Fleischer A, Pallauf K, Ramón-Barros C, Pimentel-Muiños FX. TMEM59 defines a novel ATG16L1-binding motif that promotes local activation of LC3. *The EMBO journal*. 2013;32(4):566-82.
82. Hu J, Li G, Qu L, Li N, Liu W, Hongdu B, et al. TMEM166/EVA1A interacts with ATG16L1 and induces autophagosome formation and cell death. *Cell death & disease*. 2016;7(8):e2323.



Autophagy



ISSN: 1554-8627 (Print) 1554-8635 (Online) Journal homepage: <https://www.tandfonline.com/loi/kaup20>

The ATG5-binding and coiled coil domains of ATG16L1 maintain autophagy and tissue homeostasis in mice independently of the WD domain required for LC3-associated phagocytosis

Shashank Rai, Maryam Arasteh, Matthew Jefferson, Timothy Pearson, Yingxue Wang, Weijiao Zhang, Bertalan Bicsak, Devina Divekar, Penny P. Powell, Ronald Naumann, Naiara Beraza, Simon R. Carding, Oliver Florey, Ulrike Mayer & Thomas Wileman

To cite this article: Shashank Rai, Maryam Arasteh, Matthew Jefferson, Timothy Pearson, Yingxue Wang, Weijiao Zhang, Bertalan Bicsak, Devina Divekar, Penny P. Powell, Ronald Naumann, Naiara Beraza, Simon R. Carding, Oliver Florey, Ulrike Mayer & Thomas Wileman (2019) The ATG5-binding and coiled coil domains of ATG16L1 maintain autophagy and tissue homeostasis in mice independently of the WD domain required for LC3-associated phagocytosis, *Autophagy*, 15:4, 599-612, DOI: [10.1080/15548627.2018.1534507](https://doi.org/10.1080/15548627.2018.1534507)

To link to this article: <https://doi.org/10.1080/15548627.2018.1534507>



© 2018 The Author(s). Published by Informa UK Limited, trading as Taylor & Francis Group.



[View supplementary material](#)



Published online: 07 Nov 2018.



[Submit your article to this journal](#)



Article views: 2727



[View related articles](#)




[View Crossmark data](#)



Citing articles: 5 [View citing articles](#)

The ATG5-binding and coiled coil domains of ATG16L1 maintain autophagy and tissue homeostasis in mice independently of the WD domain required for LC3-associated phagocytosis

Shashank Raj^{a*}, Maryam Arasteh^{a*}, Matthew Jefferson^{a*}, Timothy Pearson^a, Yingxue Wang^a, Weijiao Zhang^a, Bertalan Bicsak^a, Devina Divekar^a, Penny P. Powell^a, Ronald Naumann^b, Naiara Beraza^c, Simon R. Carding^c, Oliver Florey^d, Ulrike Mayer ^e, and Thomas Wileman^{a,c}

^aNorwich Medical School, University of East Anglia, Norwich, Norfolk, UK; ^bMax-Planck-Institute of Molecular Cell Biology and Genetics, Dresden, Germany; ^cQuadram Institute Bioscience, Norwich, Norfolk, UK; ^dSignalling Programme, Babraham Institute, Cambridge, UK; ^eSchool of Biological Sciences, University of East Anglia, Norwich, Norfolk, UK

ABSTRACT

Macroautophagy/autophagy delivers damaged proteins and organelles to lysosomes for degradation, and plays important roles in maintaining tissue homeostasis by reducing tissue damage. The translocation of LC3 to the limiting membrane of the phagophore, the precursor to the autophagosome, during autophagy provides a binding site for autophagy cargoes, and facilitates fusion with lysosomes. An autophagy-related pathway called LC3-associated phagocytosis (LAP) targets LC3 to phagosome and endosome membranes during uptake of bacterial and fungal pathogens, and targets LC3 to swollen endosomes containing particulate material or apoptotic cells. We have investigated the roles played by autophagy and LAP *in vivo* by exploiting the observation that the WD domain of ATG16L1 is required for LAP, but not autophagy. Mice lacking the linker and WD domains, activate autophagy, but are deficient in LAP. The LAP^{-/-} mice survive postnatal starvation, grow at the same rate as littermate controls, and are fertile. The liver, kidney, brain and muscle of these mice maintain levels of autophagy cargoes such as LC3 and SQSTM1/p62 similar to littermate controls, and prevent accumulation of SQSTM1 inclusions and tissue damage associated with loss of autophagy. The results suggest that autophagy maintains tissue homeostasis in mice independently of LC3-associated phagocytosis. Further deletion of glutamate E230 in the coiled-coil domain required for WIPI2 binding produced mice with defective autophagy that survived neonatal starvation. Analysis of brain lysates suggested that interactions between WIPI2 and ATG16L1 were less critical for autophagy in the brain, which may allow a low level of autophagy to overcome neonatal lethality.

Abbreviations: CCD: coiled-coil domain; CYBB/NOX2: cytochrome b-245: beta polypeptide; GPT/ALT: glutamic pyruvic transaminase: soluble; LAP: LC3-associated phagocytosis; LC3: microtubule-associated protein 1 light chain 3; MEF: mouse embryonic fibroblast; NOD: nucleotide-binding oligomerization domain; NADPH: nicotinamide adenine dinucleotide phosphate; RUBCN/Rubicon: RUN domain and cysteine-rich domain containing Beclin 1-interacting protein; SLE: systemic lupus erythematosus; SQSTM1/p62: sequestosome 1; TLR: toll-like receptor; TMEM: transmembrane protein; TRIM: tripartite motif-containing protein; UVRAG: UV radiation resistance associated gene; WD: tryptophan-aspartic acid; WIPI: WD 40 repeat domain: phosphoinositide interacting

ARTICLE HISTORY

Received 8 February 2018
Revised 28 September 2018
Accepted 5 October 2018

KEYWORDS

ATG16L1; brain;
LC3-associated
phagocytosis; sequestosome
1/p62 inclusions; tissue
homeostasis; WD domain;
WIPI2

Introduction


Autophagy generates autophagosomes that deliver cytoplasmic material to lysosomes for degradation. Macroautophagy, hereafter referred to as autophagy, is activated during starvation and provides a short-term supply of amino acids to sustain protein synthesis and energy production. At the same time, basal autophagy helps to prevent tissue damage during development and ageing by reducing the accumulation of damaged proteins and organelles [1,2]. Autophagosome formation involves

the recruitment of LC3 from the cytosol to the limiting membrane of the phagophore where it provides a binding site for autophagy cargoes, and facilitates fusion with lysosomes. Recent studies [3] show that LC3 is also recruited to membranes by an autophagy-related pathway called LC3-associated phagocytosis (LAP). LAP is activated by TLR signalling and NADPH oxidase during phagocytosis of fungal and bacterial pathogens, and results in attachment of LC3 to the cytosolic side of the phagosome membrane where it facilitates phagosome maturation [4].

CONTACT Thomas Wileman  t.wileman@uea.ac.uk  Norwich Medical School, University of East Anglia, Norwich, Norfolk, UK; Ulrike Mayer, u.mayer@uea.ac.uk  School of Biological Sciences, University of East Anglia, Norwich, Norfolk, UK

*These authors contributed equally to this work.

This article has been republished with minor changes. These changes do not impact the academic content of the article.

 Supplemental data for this article can be accessed [here](#).

A similar LAP-like noncanonical autophagy pathway also operates in nonphagocytic cells resulting in recruitment of LC3 to single-membraned endolysosomal compartments during entosis, micropinocytosis [5] and following lysosomotropic drug treatment [6,7], and may occur during the uptake of particulate material or apoptotic cells [8–11].

Autophagy and LAP provide 2 different pathways for removing unwanted material from cells, but the relative roles played by each pathway in reducing tissue damage and maintaining homeostasis *in vivo* are not clear. Autophagy-null mice die shortly after birth because they are unable to adapt to the starvation that follows loss of placental nutrition [12]. Mice with tissue-specific loss of autophagy survive, but the tissues lacking autophagy invariably accumulate ubiquitin-positive inclusions containing protein aggregates and show signs of inflammation and tissue damage. These studies have inactivated autophagy genes such as *Atg3*, *Atg5*, *Atg7*, *Atg12* and *Atg16L1* [12–16] that are essential for both autophagy and LAP, making it impossible to determine if tissue damage results from loss of autophagy, or LAP, or both. Studies on LAP *in vivo* have focused on inactivation of RUBCN/Rubicon in myeloid cells [3,4]. *rubcn*^{-/-} myeloid cells are LAP-deficient and show defects in clearance of bacterial and fungal pathogens and dying and apoptotic cells. These mice also have elevated levels of inflammatory cytokines, and eventually develop an autoimmune disease that resembles systemic lupus erythematosus (SLE) [4,17]. While suggestive of a role for LAP in preventing inflammation and autoimmunity, the targeted loss of RUBCN from myeloid cells does not inform on the role played by LAP in non-myeloid cell types *in vivo*.

The recruitment of LC3 to membranes during both autophagy and LAP requires the E3 ligase-like activity of the ATG12–ATG5–ATG16L1 complex, which covalently binds LC3 to membranes. ATG16L1 contains an N-terminal domain that binds the ATG12–ATG5 conjugate (Figure 1), followed by a coiled-coil domain (CCD) that binds WIPI2

[18]. WIPI2 brings the ATG12–ATG5–ATG16L1 complex to phagophore membranes allowing conjugation of LC3 to phosphatidylethanolamine [19]. In higher eukaryotes, a linker region attaches the CCD to a large C-terminal WD (tryptophan-aspartic acid) domain containing 7 WD repeats folded into a circular β -propeller [20,21]. Recent studies show that the WD domain of ATG16L1 is required for LAP [22]. This allowed us to generate LAP-deficient mice by inserting 2 stop codons in frame at the end of the CCD of the *Atg16L1* gene (Figure 1). This mutation, called *atg16l1*^{E230}, allowed translation of the glutamate E226 and E230 residues in the CCD required for WIPI2 binding and autophagy [18], but prevented translation of the linker region and WD domain required for LAP. In a second mouse, called *atg16l1*^{E226}, an unexpected recombination removed the E230 glutamate residue required for WIPI2 binding. This mouse survived postnatal starvation but was defective in autophagy and LAP in all tissues. We have used these 2 mouse strains to determine the roles played by autophagy and LAP in reducing tissue damage and maintaining tissue homeostasis *in vivo*.

Results

Mice lacking the WD and linker domain of ATG16L1 were generated by homologous recombination in embryonic stem cells. The targeting vector was designed to insert 2 stop codons after glutamate residue E230 in the CCD, followed by the bovine growth hormone polyadenylation site and a flanked neomycin cassette. Homologous recombination was verified by Southern blotting. RNA analysis of the F1 generation established from independent chimeras showed that most mice carried the correct sequence and expressed the E230 residue required for autophagy. Surprisingly, some mice had a 14 base pair (bp) deletion at the end of the CCD, which deleted glutamate E230 and its preceding amino acid,

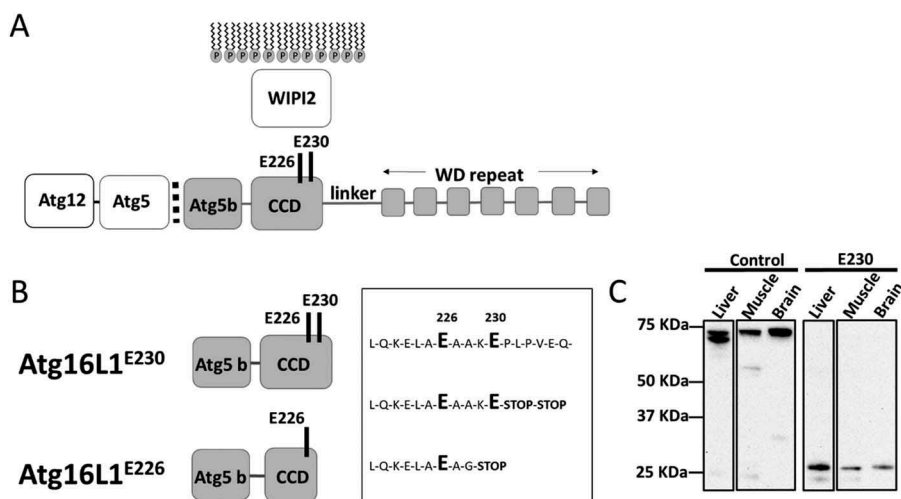


Figure 1. Generation of mice lacking the WD and linker domains of ATG16L1. (A) Domain structure of ATG16L1. The N-terminal ATG5 binding domain (ATG5 b) binds the ATG12–ATG5 conjugate. The coiled-coil domain (CCD) binds WIPI2 through glutamates E226 and E230. A linker domain separates the CCD from the 7 WD repeats of the WD domain. (B) Sites of stop codons. *atg16l1*^{E230}, 2 stop codons were inserted into exon 6 immediately after glutamate E230 to preserve binding sites for WIPI2, but prevent translation of the linker and WD domain. *atg16l1*^{E226}; an unexpected recombination inserted a glycine residue at position 228. (C) Tissue lysates were separated by SDS-PAGE and transferred to nitrocellulose membranes. Separate membranes sections were analyzed by western blot using antibody specific for ATG16L1.

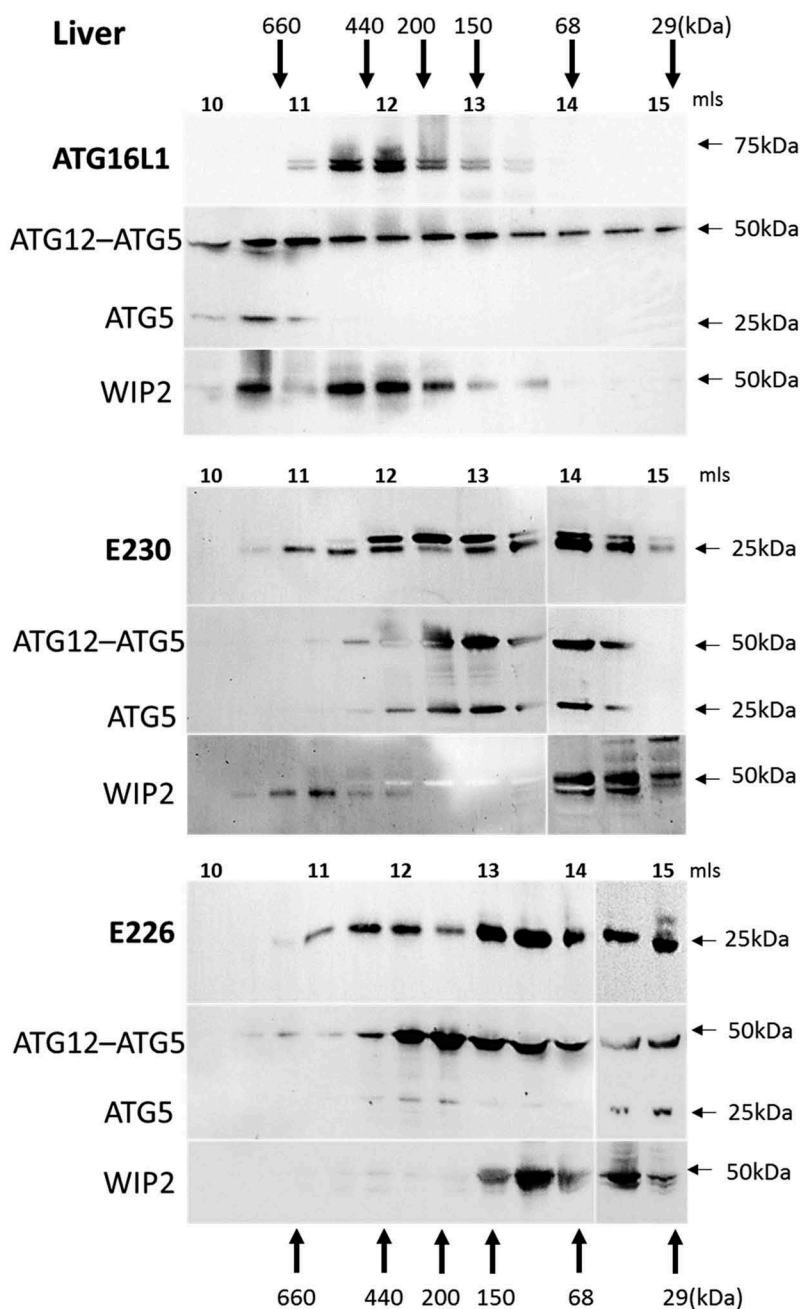


Figure 2. Analysis of ATG16L1 complexes in liver by gel filtration. The cytosolic fraction of liver homogenates was separated by size-exclusion chromatography on an ENrich™SEC 650 column. Fraction (0.5 ml) were analyzed by immunoblot for ATG16L1, ATG5 and WIP2 as indicated. Void volume 10 ml. Migration and elution of molecular mass standards are shown (kDa).

followed by a stop codon (Figure 1 A and B). These mouse strains were termed *atg16l1*^{E230} and *atg16l1*^{E226}.

Expression of the truncated ATG16L1^{E230} CCD was verified by comparing western blots of tissue lysates from the *atg16l1*^{E230} mice with littermate controls (Figure 1C). The ATG5 binding and CCD of ATG16L1 migrated at ~ 27 kDa compared to the ~ 70 kDa for full-length ATG16L1. As described by Mizushima et al [21], lysates from liver showed the α and β isoforms of ATG16L1 while the slower migrating β isoform predominated in muscle and brain. Full-length ATG16L1 was present in lysates obtained from littermate controls, but absent from tissues of *atg16l1*^{E230} mice. It was not possible to detect the truncated CCD of the *atg16l1*^{E226}

mice, in whole tissue lysates. This may be because the epitope is lost, or the protein is highly unstable.

The size of the ATG16L1 complex generated in the mice was determined by gel filtration of cytoplasmic fractions isolated from homogenized liver (Figure 2). In control mice the α and β isoforms of ATG16L1 eluted in high molecular-mass fractions suggesting formation of a 300–600 kDa complex. Previous work has shown that elution of ATG16L1 in high molecular-weight fractions is dependent on ATG5 [21]. The presence of the ATG12-ATG5 conjugate in the same high molecular weight fractions as ATG16L1 suggested binding of ATG5 to the N-terminal ATG5-binding domain present in the CCD of ATG16L1. Full-length ATG16L1 contains the E226 and E230

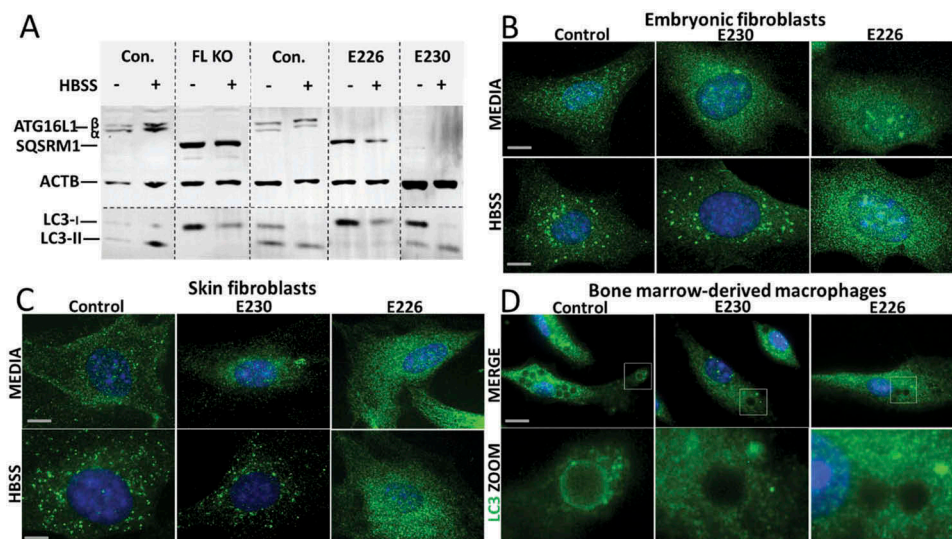


Figure 3. Role played by WD and linker domains of ATG16L1 during autophagy and LC3-associated phagocytosis. (A) MEFs from mice lacking ATG16L1 (FL KO), *atg16l1*^{E226} (E226) and *atg16l1*^{E230} (E230) and appropriate littermate controls were incubated in complete media or HBSS for 2 h to induce autophagy. Cell lysates were analyzed by western blot using antibodies specific for the indicated proteins. (B) MEFs or skin fibroblasts (C) from *atg16l1*^{E226} (E226) and *atg16l1*^{E230} (E230) mice and littermate controls were incubated in complete media or HBSS for 2 h to induce autophagy. Cells were immunostained for endogenous LC3. (D) BMDMs from *atg16l1*^{E226} (E226) and *atg16l1*^{E230} (E230) and appropriate littermate controls were incubated with Pam3CSK4-coupled polystyrene beads for 1.5 h in complete medium to induce LAP, and immunostained for endogenous LC3 (green). Boxed regions highlighting internalized beads are enlarged and shown in the lower panel. Magnification 63X, scale bars: 10 μ m.

glutamate residues required for WIPI2 binding, and indirect evidence for binding to WIPI2 was provided by the elution of the 49-kDa WIPI2 protein in high molecular-mass fractions ranging between 150 and 600 kDa. Analysis of the *atg16l1*^{E230} and *atg16l1*^{E226} mice was complex because the preparation of liver lysates appeared to result in limited proteolysis of CCDs, and the possible formation of dimers and trimers resistant to dissociation during SDS polyacrylamide electrophoresis (Fig. S1). The blots in Figure 2 show the elution profile of the 27-kDa CCD and the 25-kDa proteolytic products, which co-elute with multimers at 50 and 75 kDa (Fig. S1). The bulk of the CCD in the liver of *atg16l1*^{E230} mice eluted over a broad range from 50–400 kDa in fractions which also contained the ATG12–ATG5 conjugate and ATG5. As seen for control mice, WIPI2 was detected in high molecular-mass fractions eluting between 400–600 kDa; however, levels of WIPI2 were less than seen for control, and a low molecular-mass fraction was also detected between 50 and 100 kDa. The CCD of *atg16l1*^{E230} mice retained binding sites for ATG5 and WIPI2, and the elution profiles were consistent with assembly of complexes containing the CCD, ATG12–ATG5 and WIPI2. Unlike whole tissue lysates, it was possible to detect the CCD of the *atg16l1*^{E226} mouse in fractions eluting from the gel filtration column. The CCD eluted over a broad 30–400 kDa range in fractions that also contained ATG12–ATG5. The CCD of *atg16l1*^{E226} mice lacks the E230 glutamate residue required for WIPI2. The blots show that unlike control mice and *atg16l1*^{E230} mice, it was not possible to detect WIPI2 in high molecular-mass fractions, and WIPI2 eluted between 50 and 100 kDa. The results from this indirect assay based on the size of ATG16L1 complexes suggest that the CCD of *atg16l1*^{E226} assembles with ATG12–ATG5 through the ATG5 binding domain, but does not bind strongly to WIPI2.

The ability of cells isolated from the mice to activate autophagy was tested by western blot of autophagy substrates

SQSTM1/p62 (sequestosome 1) and LC3, and by following formation of LC3 puncta after starvation in Hanks balanced salt solution (HBSS) (Figure 3A–C). Mouse embryonic fibroblasts (MEFs) from mice lacking ATG16L1 (*atg16l1*^{-/-}) were used as an autophagy-negative control. MEFs from control mice expressed the α and β isoforms of ATG16L1 which were absent from *atg16l1*^{-/-}, *atg16l1*^{E226} and *atg16l1*^{E230} MEFs, whereas *atg16l1*^{E230} MEFs showed the smaller band expected at 27 kDa (data not shown). *atg16l1*^{-/-} MEFs showed defects in autophagy indicated by the expression of high levels of the autophagy substrate SQSTM1, and an inability to generate lipidated LC3-II (Figure 3A) after starvation. MEFs expressing ATG16L1^{E226} also expressed high levels of SQSTM1 and were unable to generate lipidated LC3-II showing that loss of E230 resulted in defects in autophagy. This supported the observation that MEFs (Figure 3B) and skin fibroblasts (Figure 3C) from *atg16l1*^{E226} mice were unable to generate LC3 puncta following starvation. In contrast, cells expressing full-length ATG16L1, or expressing the CCD but lacking the WD domain (ATG16L1^{E230}) were able to activate autophagy, indicated by low basal levels of SQSTM1 and generation of LC3 puncta in response to HBSS (Figure 3B,C). Taken together, these results showed that autophagy requires the E226 and E230 glutamate residues in the CCD needed for WIPI2 binding, but, as reported previously [19], autophagy did not require the WD domain. The role played by the WD domain during LAP was analyzed by incubating bone marrow-derived macrophages (BMDMs) from the mouse strains with Pam3CSK4 (a mimic of bacterial lipopeptides)-coupled polystyrene beads to follow LC3 translocation to phagosomes (Figure 3D). LC3 was recruited to phagosomes in macrophages from control mice, but not in macrophages from autophagy-defective *atg16l1*^{E226} mice, or *atg16l1*^{E230} mice that lack the WD domain and linker region of ATG16L1. As

reported previously [22,23] these observations indicate that the WD domain is required for LAP in myeloid cells, and confirmed that the *atg16l1*^{E230} mouse would provide a LAP-deficient mouse model to study the role played by LAP in maintaining tissue homeostasis *in vivo*.

Mouse growth and survival

The LAP-deficient *atg16l1*^{E230} mice survived the postnatal lethality seen in *atg16l1*^{-/-} mice [15], and were similar in size and weight to littermate controls and grew at comparable rates (Figure 4A, B). *atg16l1*^{E230} mice were born with Mendelian frequency with reproductive organs of normal size, and were fertile with a reproductive capacity comparable to controls (data not shown). The survival rate and litter sizes of *atg16l1*^{E230} mice were similar to wild-type mice with life spans of at least 24 months (data not shown). The majority of *atg16l1*^{E226} mice also survived postnatal lethality, but most grew slowly (Figure 4A, B) and died within 5–7 months of age.

Inflammatory cytokines

LAP-deficient mice generated by *Lyz2/LysM-cre*-driven loss of *Rubcn* from macrophages, monocytes and neutrophils (3) develop a SLE-like syndrome characterized by an age-dependent increase in serum cytokines and eventual generation of antibodies against nuclear antigens. Serum levels of IL1B, IL12 (p70), IL13, TNF, IL6 and CCL2/MCP1 reported to be elevated in *rubcn*^{-/-} mice were measured in control, *atg16l1*^{E230} and *atg16l1*^{E226} mice. Serum levels of IL1B, IL12 (p70), IL13, and TNF/TNF- α in *atg16l1*^{E230} and *atg16l1*^{E230} mice were the same as littermate controls at 8–12 and 20–24 wk. Elevated levels of IL6 and CCL2/MCP1 were detected in the autophagy-defective *atg16l1*^{E226} mice, but these were not seen in control or *atg16l1*^{E230} mice (Fig. S2). It was not possible to detect antinuclear antibodies able to stain the nuclei of cells in culture. The LAP^{-/-} *atg16l1*^{E230} mice do not therefore appear to develop the pro-inflammatory phenotype seen for *rubcn*^{-/-} mice lacking LAP in phagocytic cells.

Liver

A preliminary survey of the internal organs of the mouse strains showed that defects were most obvious in the liver of the autophagy-defective *atg16l1*^{E226} mice. The livers (Figure 5A) showed pronounced hepatomegaly with average liver weights of 2.6 g, compared to 1.6 g of control mice, and when liver weight was expressed as percentage of body weight (Figure 5B) to compensate for the smaller size of the *atg16l1*^{E226} mouse, livers were more than twice the size (11%) of littermate controls (5%). These results are in line with studies of mice with targeted loss of *Atg7* in liver [13], or the hepatomegaly observed in *atg5*^{-/-} mice where *Atg5* is restored in neuronal tissue [24]. Liver damage was evident from elevated levels of serum GPT/ALT (glutamic pyruvic transaminase, soluble), a liver function marker enzyme (Figure 5C). In contrast, there was little evidence for hepatomegaly in *atg16l1*^{E230} LAP-deficient mice with mean weights of 1.8 g being the comparable to littermate controls, and these mice did not show the raised serum GPT/ALT levels seen in autophagy-defective mice. Autophagy function in liver tissue was assessed by western blot of SQSTM1 and LC3, which are substrates for autophagy and are degraded in lysosomes. The signals for full-length ATG16L1 were present in blots of 3 representative livers taken from control mice. Two bands were seen, consistent with the expression of α and β isoforms of ATG16L1 in liver [21], but absent from blots of *atg16l1*^{E226} and *atg16l1*^{E230} mice (Figure 5D). Liver lysates from the *atg16l1*^{E226} mouse showed raised levels of LC3-I and SQSTM1 compared to control mice, suggesting impaired clearance of autophagy substrates ‘*in vivo*’ (Figure 5D). Immunohistological analysis showed SQSTM1 inclusions in hepatocytes, indicative of accumulation of damaged proteins and organelles in *atg16l1*^{E226} mice (Figure 5E). In contrast livers from the LAP-deficient *atg16l1*^{E230} mice were similar in size to littermate controls (Figure 5A), and lysates did not reveal raised levels of LC3-I and SQSTM1 (Figure 5D). Moreover, SQSTM1 inclusions were absent from hepatocytes (Figure 5E), suggesting that autophagy is active in the liver. Further analysis confirmed that hepatomegaly in *atg16l1*^{E226} mice correlated with hepatocellular hypertrophy as evidenced by the enlarged circumference of hepatocytes (Figure 6A) and increased hepatocyte proliferation indicated by a 4-fold increase in MKI67/Ki67 immunostaining (Figure 6B).

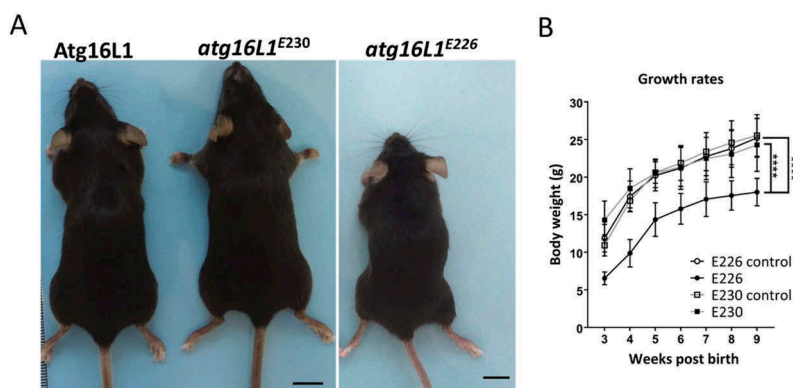


Figure 4. Phenotype of *atg16l1*^{E226} and *atg16l1*^{E230} mice. (A) Representative pictures of mice at ~2 months of age (scale bar: 1 cm). (B) Body weight of mice and littermate controls fed on chow diet. Mice were weighed at the indicated times and each point is generated from at least 6 individuals ($n = 11$ and 6 for E230 (*atg16l1*^{E230}) and control, respectively; $n = 11$ and 8 for E226 (*atg16l1*^{E226}) and control, respectively). Statistical analysis was done by unpaired t test. Error bars represents \pm SEM. ****- $P < 0.0001$.

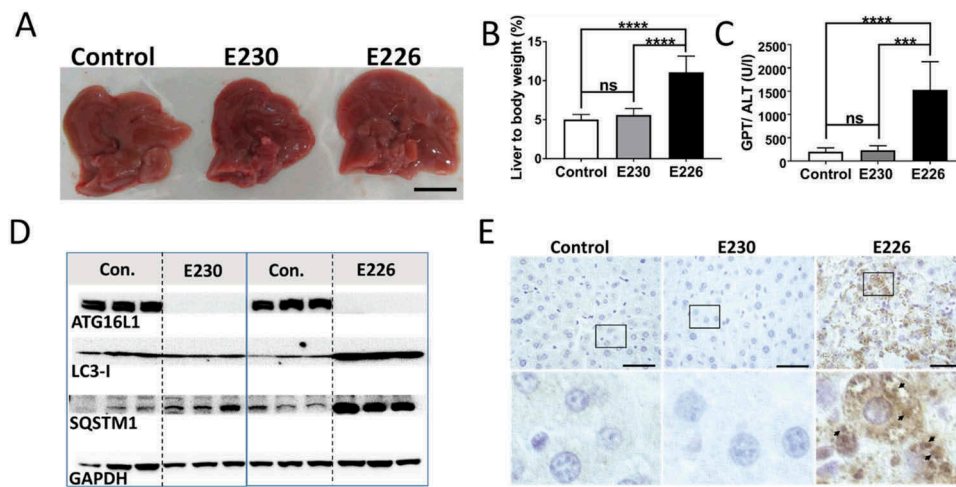


Figure 5. Analysis of autophagy substrates in liver. Panel (A) Representative livers at ~2 months (scale bar: 1 cm). (B) Liver weight expressed as a percentage of body weight at 2–3 months of age. E230 (*atg16l1^{E230}*) *n* = 9, control *n* = 8; E226 (*atg16l1^{E226}*) *n* = 9, control *n* = 7. (C) GPT/ALT in serum from mice aged between 2–3 months. E230 (*atg16l1^{E230}*) *n* = 7, control *n* = 5; E226 (*atg16l1^{E226}*) *n* = 5, v control *n* = 5. (D) Western blot of liver lysates from 3 representative mice. Membranes strips taken from the appropriate molecular weight range were analyzed separately using the indicated antibodies. (E) Representative histochemical sections of livers immunostained for SQSTM1. Enlarged regions of interest are shown in the lower panel. Arrows: SQSTM1 inclusions. In all figures data from littermate controls for E230 and E226 were pooled. Statistical analysis was done by unpaired t test. Error bars represents \pm SEM. ****-*P* < 0.0001, ***-*P* < 0.001; ns, non-significant. Image magnification 40X, scale bars: 50 μ m.

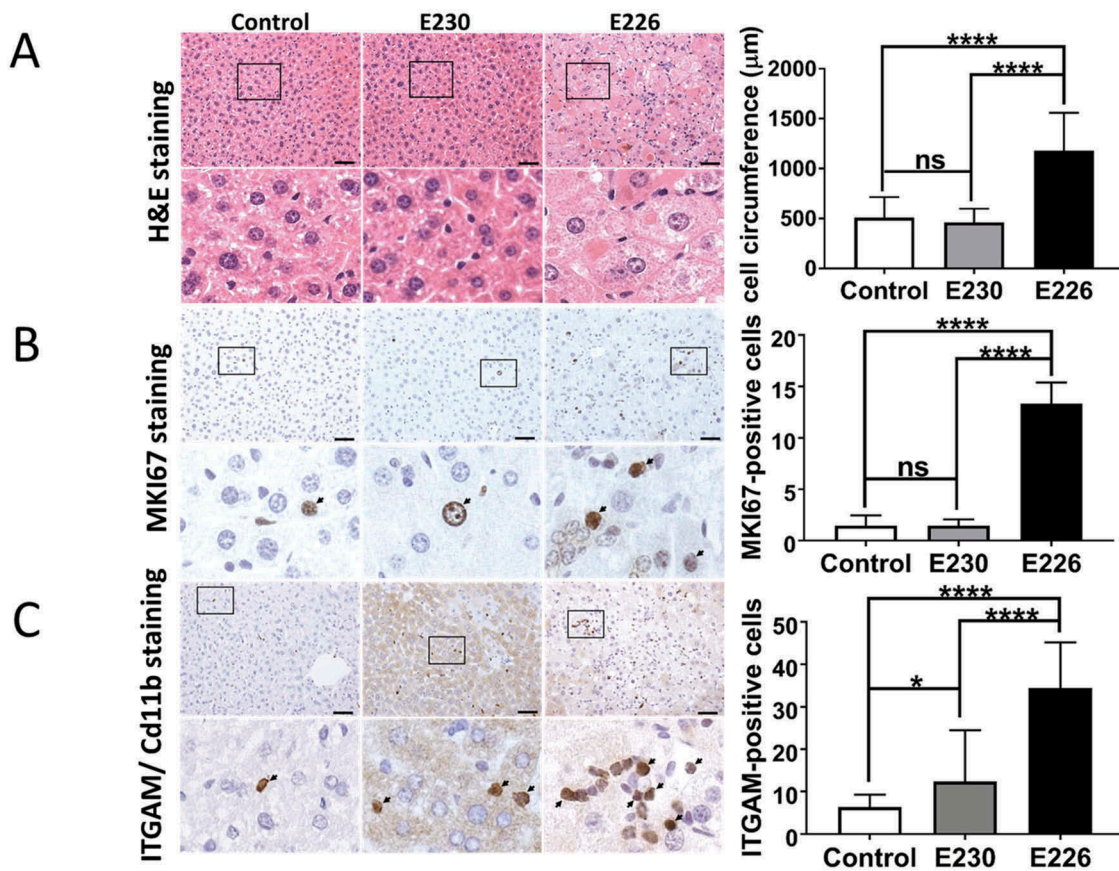


Figure 6. Analysis of liver homeostasis. (A) Representative images of H&E-stained sections of livers. Boxed regions of interest are enlarged in lower panels. The bar graph represents comparative circumferences of hepatocytes (*n* = 10) across the indicated strains (*n* = 3 for all the strains). (B and C) Representative histochemical sections of liver immunostained with antibodies against MKI67/Ki67 (B) or ITGAM/Cd11b (C). Regions of interest are enlarged and shown in lower panels. Arrows indicate positive staining. Bar graphs show number of positive cells (C) or percent positive cells (B). Five different zones for each liver section were analyzed (*n* = 3 for all the strains). Data across littermate control mice for E230 and E226 were pooled. Statistical analysis was done by unpaired t test. Error bars represents \pm SEM. ****-*P* < 0.0001, *-*P* < 0.1. Magnification 20X, scale bars: 50 μ m.

Liver inflammation was also evident from increased infiltration of ITGAM/CD11b-positive leukocytes (Figure 6C). In contrast, livers from the *atg16l1*^{E230} mice showed little sign of damage. A comparison of the mice suggested that LAP was not required to suppress tissue damage because the liver parenchyma damage, hepatocellular hypertrophy (Figure 6A) and raised serum GPT/ALT levels (Figure 5C) seen in the *atg16l1*^{E226} mice, were absent from *atg16l1*^{E230} mice. Furthermore, hepatocyte proliferation (Figure 6B) was comparable to that found in littermate controls. There was evidence of low level inflammatory cell infiltration in the livers from *atg16l1*^{E230} mice (Figure 6C), possibly indicating a role for LAP in reducing inflammation, but levels of ITGAM/Cd11b-positive cells were much lower than seen in livers of autophagy-defective *atg16l1*^{E226} mice.

Muscle and kidney

The *atg16l1*^{E226} mice showed evidence of muscle wasting because the gastrocnemius muscle was significantly smaller in *atg16l1*^{E226} mice when muscle weight was expressed as a percentage of body weight (Figure 7A). Lysates from muscle had high levels of SQSTM1 and LC3 (Figure 7B), and when normalized for GAPDH expression, muscle lysates from the *atg16l1*^{E226} mice showed 2–3 fold increases in LC3-I, and nearly 6-fold increases in SQSTM1 compared to control mice (Figure 7C), suggesting impaired clearance of autophagy substrates 'in vivo'. This was consistent with histological sections of muscle showing multiple SQSTM1 inclusions (Figure 7D). Morphological analysis of muscle did not, however, reveal the degenerative changes observed in mice lacking ATG7 in muscle tissue [25], such as vacuolated and centrally nucleated myofibers.

The kidneys of *atg16l1*^{E226} mice weighed less than controls, but this difference was not statistically significant when expressed as a percentage of body weight (Figure 8A). Kidney lysates of

atg16l1^{E226} mice contained raised levels of LC3-I and SQSTM1 (Figure 8B and C) and histological sections of kidney showed multiple SQSTM1 inclusions (Figure 8D). We were not, however, able to find evidence of obvious kidney damage and glomerular architecture remained intact. In contrast to the autophagy-negative *atg16l1*^{E226} mice, the muscle and kidney of LAP-deficient *atg16l1*^{E230} mice were of comparable size to littermate controls (Figures 7A and 8A) and blots of tissue lysates did not show raised levels of LC3-I or SQSTM1 (Figures 7B and 8B), consistent with the absence of SQSTM1 inclusions in tissue sections (Figures 7D and 8D). As seen for liver, tissue homeostasis in kidney and muscle required autophagy, but did not require the WD domain of ATG16L1 and was, therefore maintained independently of LAP.

Brain

The autophagy-defective *atg16l1*^{E226} mice showed a range of neurological defects including loss of motor coordination, abnormal limb claspings and an unusual splayed gait suggesting defects in both the peripheral and central nervous system (data not shown). The neurological phenotype of autophagy-defective *atg16l1*^{E226} mice mirrored the loss of motor coordination seen in mice deficient in ATG7 in the central nervous system [26]. The brains of the *atg16l1*^{E226} mice were smaller than littermate controls, but there was no significant difference when brain weights were expressed as a percentage of body weight (Figure 9A). There were high levels of SQSTM1 in brain lysates (Figure 9B and C), and brain sections showed evidence of SQSTM1 inclusions (Figure 9D). In contrast, brain lysates from the LAP-deficient *atg16l1*^{E230} mice had levels of LC3-I and SQSTM1 similar to controls (Figure 9B and C), and brains lacked SQSTM1 inclusions (Figure 9D). Although motor coordination appeared normal in the majority of the *atg16l1*^{E230} mice, some developed head tilt suggesting defects in the inner ear or possible ear infection.

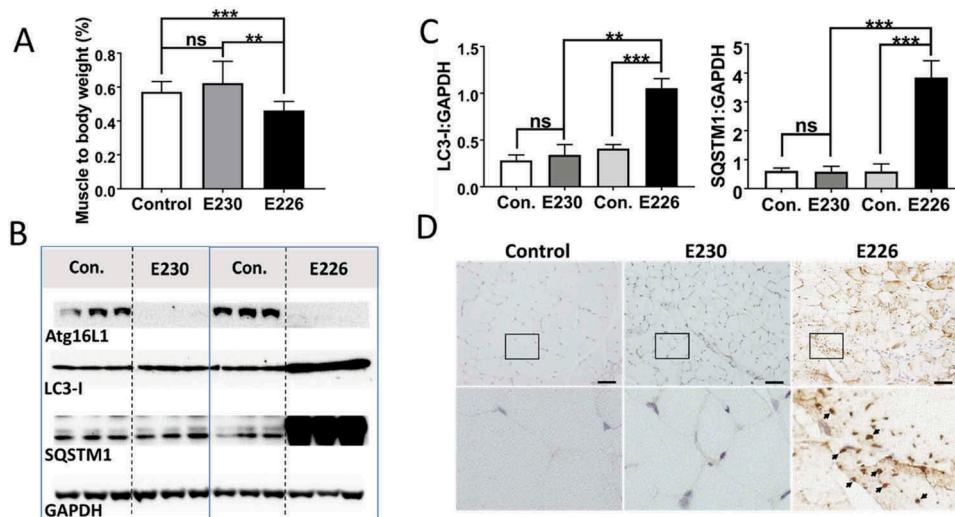


Figure 7. Analysis of muscle. (A) Gastrocnemius muscle weight expressed as a percentage of body weights at 2–3 months of age. E230 (*atg16l1*^{E230}) n = 6, control n = 5; E226 (*atg16l1*^{E226}) n = 8, control n = 6. (B) Western blot of muscle lysates from 3 representative mice. Membrane strips taken from the appropriate molecular weight range were analyzed separately by western blot using the indicated antibodies. (C) Bar graphs show levels of LC3 and SQSTM1 relative to GAPDH. (D) Histochemical sections of muscle were immunostained with antibodies against SQSTM1. Enlarged regions of interest are shown in the lower panels. Arrows: SQSTM1 inclusions. Statistical analysis was done by unpaired t test. Error bars represent \pm SEM. ***-P < 0.001, **-P < 0.01; ns, non-significant. Magnification 20X, scale bar: 50 μ m.

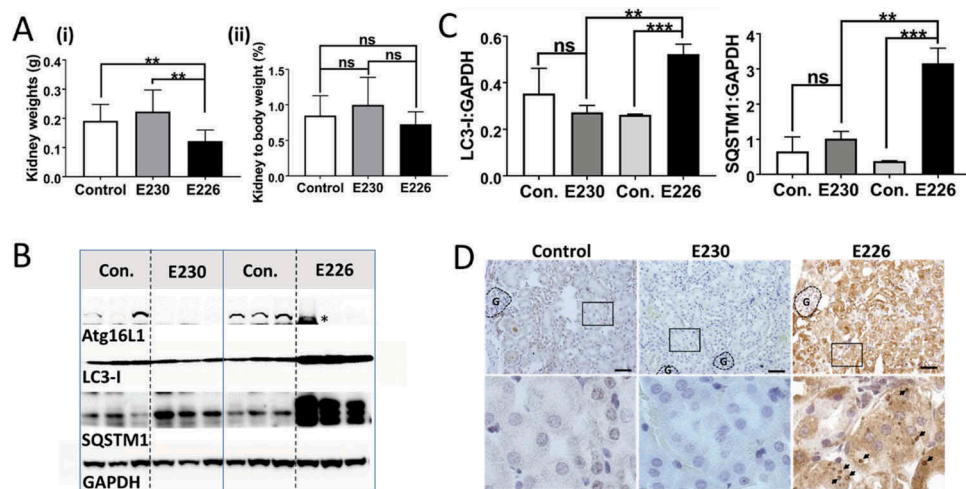


Figure 8. Analysis of kidney. (A) Kidney weights at 2–3 months expressed (i) directly: E230 (*atg16l1*^{E230} n = 8, control n = 8, E226 (*atg16l1*^{E226}) n = 7, control = 8; or as (ii) percentage body weight: E230 (*atg16l1*^{E230} n = 9, control n = 8, E226 (*atg16l1*^{E226}) n = 7, control = 6. (B) Western blot of kidney lysates from 3 representative mice. Membrane strips taken from the appropriate molecular weight range were analyzed separately using the indicated antibodies. (C) Bar graphs show levels of LC3 and SQSTM1 relative to GAPDH. (D) Histochemical sections of kidneys immunostained for SQSTM1. (G) Indicates glomerulus. Enlarged regions of interest are shown in lower panels. Arrows: SQSTM1 inclusions. Data from control mice were pooled. Statistical analysis was done by unpaired t test. Error bars represent \pm SEM. ***-P < 0.001, **-P < 0.01; ns, non-significant. Magnification 20X, scale bars: 50 μ m.

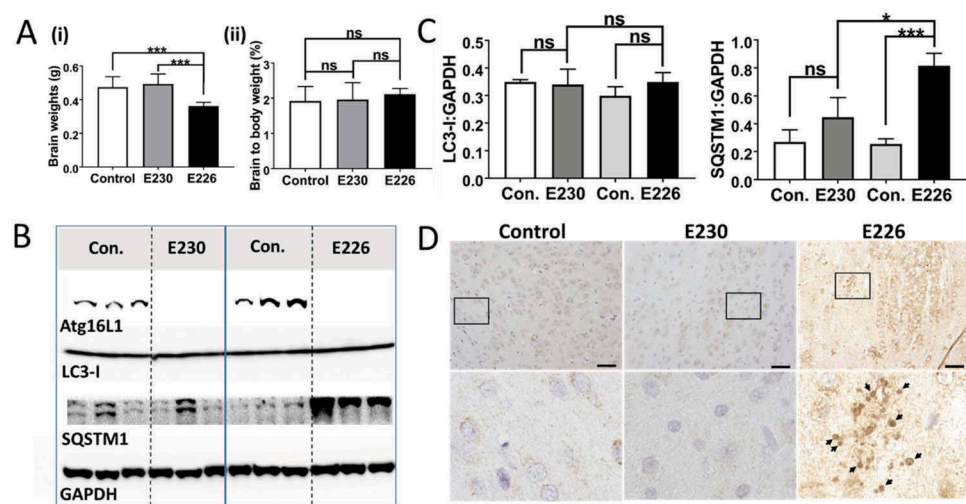


Figure 9. Analysis of brain. (A) Brain weights at 2–3 months expressed (i) directly: E230 (*atg16l1*^{E230} n = 8, control n = 7, E226 (*atg16l1*^{E226}) n = 7, control = 7; or (ii) as percentage body weight: E230 (*atg16l1*^{E230} n = 8, control n = 9, E226 (*atg16l1*^{E226}) n = 6, control = 5. (B) Western blot of brain lysates from 3 representative mice. Membrane strips taken from the appropriate molecular weight range were analyzed separately by western blot using the indicated antibodies. (C) Bar graphs show levels of LC3 and SQSTM1 relative to GAPDH. (D) Histochemical sections of brains were immunostained for SQSTM1. Enlarged regions of interest are shown in lower panels. Arrows indicate SQSTM1 inclusions. Data from control mice were pooled. Statistical analysis was done by unpaired t test. Error bars represents \pm SEM. ***-P < 0.001, *-P < 0.1; ns, non-significant. Magnification 20X, scale bars: 50 μ m.

Mice with systemic loss of ATG16L1 from all tissues (*atg16l1*^{-/-}) die at birth from a suckling defect [15]. This raised the question of how the *atg16l1*^{E226} mice, which appear autophagy-defective, survive neonatal lethality. Neonatal lethality in *atg5*^{-/-} mice can be reversed by brain-specific re-expression of ATG5 [24]. These rescued mice (*atg5*-null) lack ATG5 and autophagy in non-neuronal tissues and develop multiple organ abnormalities with a phenotype closely resembling the *atg16l1*^{E226} mouse described here. Both the *atg5*-null and *atg16l1*^{E226} mice, survived neonatal lethality, but grew slowly compared to control mice, and have pronounced hepatomegaly and sarcopenia. This makes it possible that *atg16l1*^{E226} mice described in our study survive neonatal lethality because they carry out a low level of autophagy in the brain. Interestingly, the LC3-I levels in the brain of *atg16l1*^{E226} mice were the same as controls (Figures 9B and 9C). This was in

contrast to peripheral tissues such as liver (Figure 5D), muscle (Figure 7B and C) and kidney (Figure 8B and C) where LC3 was elevated 3–4 fold. The preservation of control levels of LC3-I in *atg16l1*^{E226} mice suggest that LC3 may be degraded in the brain by autophagy. This observation, and the striking similarity in phenotype with the neuronal-specific rescue of *atg5*-null mice described by Yoshii et al [24], suggests that the brain of *atg16l1*^{E226} mice may compensate for the loss of autophagy arising from loss of the E230 residue required for WIPI2 binding. The size exclusion analysis of liver extracts in Figure 2 showed the elution of WIPI2 in high molecular-weight fractions in mice expressing full-length ATG16L1 or the CCD of ATG16L1 that retained glutamate E230 required for WIPI2 binding, but not in mice expressing the ATG16L1^{E226} CCD lacking E230. This provides an indirect assay for binding of WIPI2 to ATG16L1 when gel

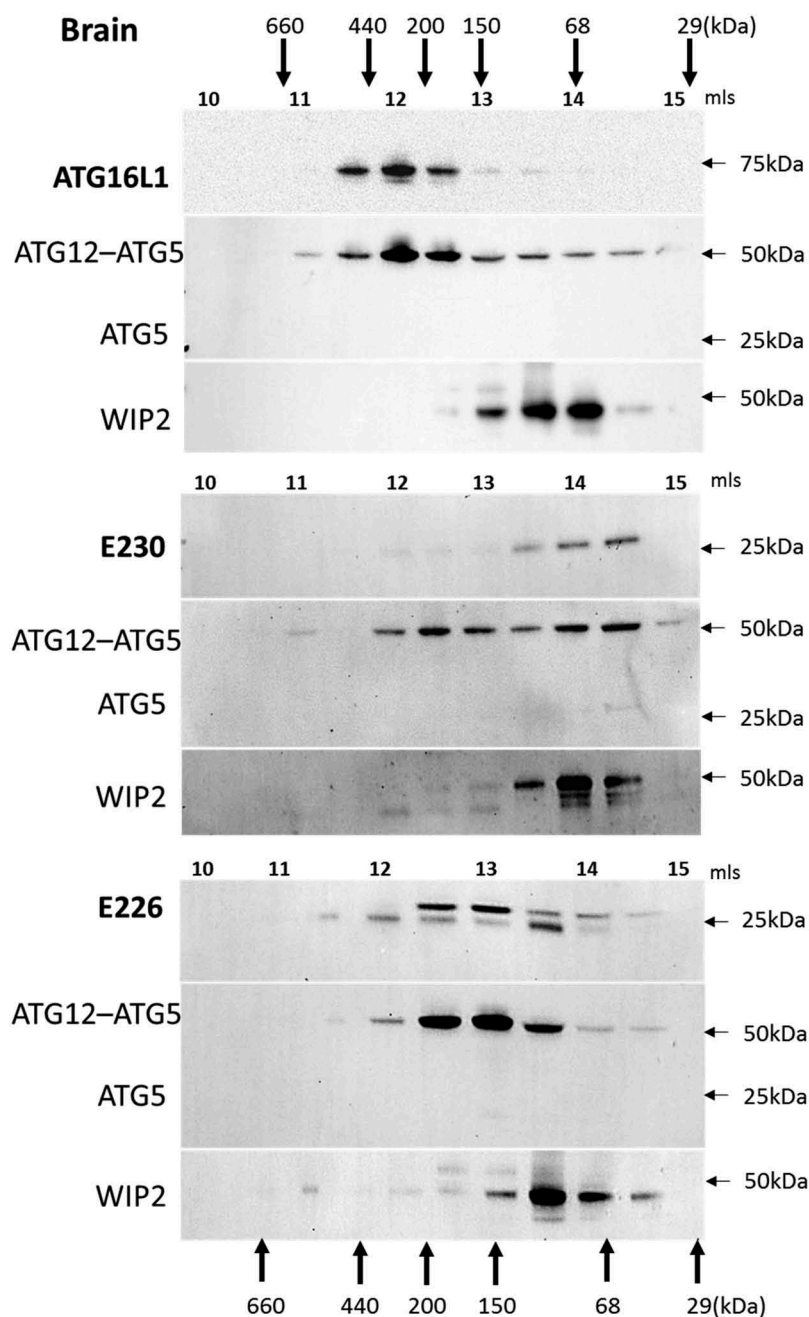


Figure 10. Analysis of ATG16L1 complexes in brain by gel filtration. The cytosolic fraction of brain homogenates was separated by size-exclusion chromatography on an ENrich™ SEC 650 column. Fraction (0.5 ml) were analyzed by immunoblot for ATG16L1, ATG5 and WIPI2 as indicated. Void volume 10 ml. Migration and elution of molecular mass standards are shown (kDa).

filtration was repeated for brain lysates (Figure 10). As seen in liver, ATG16L1 in control mice eluted in high molecular-mass fractions suggesting formation of a 300- to 600-kDa complex. These same fractions contained the ATG12-ATG5 conjugate, but surprisingly these fractions did not contain WIPI2, which eluted between 50 and 100 kDa (Figure 10). Similarly, the ATG16L1^{E230} and ATG16L1^{E226} CCDs formed high molecular-weight complexes and co-eluted with ATG12-ATG5 but were unable to move WIPI2 to high molecular-weight fractions. The profiles resembled that seen for the ATG16L1^{E226} CCD in liver that lacks the E230 glutamate required for WIPI2 binding (Figure 2). Taken together the results suggested that the binding of ATG16L1 to WIPI2 differs in brain compared to liver. This may provide the basis for a low level of autophagy in brain that allows the *atg16l1*^{E226} mice to survive neonatal lethality.

Discussion

We have generated mice lacking the WD and linker domains of ATG16L1 to study the roles played by autophagy and LAP in maintaining tissue homeostasis *in vivo*. The *atg16l1*^{E230} mice were unable to activate LAP, but retained glutamate E226 and E230 in the CCD required for WIPI2 binding and could therefore activate autophagy. These mice grew at the same rate as littermate controls, were fertile and did not have obvious defects in liver, kidney, brain or muscle homeostasis. This suggests that autophagy rather than LAP plays a major role in reducing tissue damage *in vivo*. The WD domain of ATG16L1 in higher eukaryotes including insects, nematodes,

plants and humans contains over half the amino acids of the 66-kDa protein [21]. Gel filtration analysis suggested that full-length ATG16L1 formed a 300- to 600-kDa complex in liver and brain. The CCDs of the *atg16l1^{E230}* and *atg16l1^{E226}* mice eluted over a broad size ranging from 50–400 kDa suggesting multimeric assembly in the absence of the WD domain. These results are consistent with previous gel filtration analysis [21] demonstrating 600- to 800-kDa complexes of ATG16L1 in lysates of liver, brain and fibroblast cell lines, and the formation of additional smaller complexes ranging between 100 and 300 kDa in fibroblasts expressing ATG16L1 lacking the WD domain. Initial calculations based on gel filtration suggest formation of complexes containing 8 copies of ATG16L1 bound to the ATG12–ATG5 conjugate [21]. Later work analyzing the ATG16L1 complex by sucrose gradient sedimentation suggests ATG16L1 exists as a dimer [27]. This discrepancy in size estimation could be explained if ATG16L1 adopted an elongated conformation in solution accelerating its elution from gel filtration columns. Regardless of the precise size of complexes formed by ATG16L1 and the CCDs of the *atg16l1^{E230}* and *atg16l1^{E226}* mice, all three co-eluted with ATG12–ATG5. This increase in apparent size of the 72 kDa ATG12–ATG5 conjugate suggests the conjugate binds all 3 CCDs via the N-terminal ATG5 binding domain. The binding of WIPI2 to ATG16L1 requires glutamate E230 in the CCD, which is absent in the CCD of the *atg16l1^{E226}* mice. The lack of elution of WIPI2 in high molecular-weight liver fractions containing the CCD of the *atg16l1^{E226}* mouse suggested that loss of glutamate E230 results in reduced WIPI2 binding *in vivo*.

The WD domains of ATG16L1 represent as much as a third of the total protein. It is perhaps remarkable that this complex of 7 bladed β -propellers, which are thought to provide a platform for protein-protein interactions important for autophagy, play little role in maintaining tissue homeostasis 'in vivo'. Instead, evolution appears to have confined this important role to the N-terminal ATG5 binding and CC domains conserved through to the yeast ortholog Atg16 [28]. Binding of ATG16L1 to WIPI2 requires glutamate residues E226 and E230 in the ATG16L1 CCD, which bind arginine R108 and R125 exposed on the surface of WIPI2. Deletion of either E226 or E230 in ATG16L1 abrogates binding to WIPI2, and expression of WIPI2 lacking R108 and R125 is unable to reconstitute LC3 recruitment to phagosomes in WIPI2-depleted cells [18]. Our study shows that the integrity of this WIPI2 binding site within the short N-terminal domain is critical for autophagy *in vivo*, because loss of one amino acid, E230, required for WIPI2 binding, results in loss of autophagy and results in multiple tissue abnormalities.

Macrophages and fibroblasts cultured from mice lacking the WD domain were unable to activate LAP. This is in agreement with previous work [22], showing that the WD domain is required for several noncanonical pathways that recruit LC3-II to endocytic compartments. These include newly formed macropinosomes, phagosomes containing latex beads or apoptotic corpses, endosomes swollen by monensin or a combination of ammonium chloride and the vacuolating toxin A from *Helicobacter pylori*, and endosomes

targeted by the M2 proton channel encoded by influenza virus. Furthermore, loss of the WD domain from ATG16L1 in dendritic cells results in reduced secretion of TNF and IL1B in response to CLEC4N/Dectin2 signalling [23] and reduced antigen presentation by dendritic cells [22]. The requirement of the WD domain for LAP suggests that the scaffold provided by the WD domains of ATG16L1 has evolved a specialized role, independent of autophagy, to ensure the quality control of endocytic pathways by conjugating LC3 to phagosomes containing pathogens or apoptotic cells, or endocytic compartments showing signs of damage. This is supported by the observation that the WD domain of ATG16L1 binds NOD-like receptors [29], MEFV/TRIM20 [30], TMEM59 [31] and EVA1A/TMEM166 [32], which are important in pathogen recognition. Our observation that mice remain viable and maintain tissue homeostasis over long periods in the absence of the WD domain suggests that LAP does not play an essential role in preventing tissue damage *in vivo*. LAP in phagocytic cells requires RUBCN and CYBB/NOX2 [3] and mice with *Lyz2/LysM-cre*-targeted disruption of either of these genes in macrophages, monocytes and neutrophils, grow slowly. We did not observe slowed growth for the *atg16l1^{E230}* LAP-defective mice suggesting that loss of LAP from all tissues allows mice to compensate for loss of LAP in phagocytic cells. Alternatively, the deletion of the WD domain, and loss of RUBCN and CYBB/NOX2, inactivate LAP by different mechanisms. ATG16L1 is downstream of RUBCN and CYBB/NOX2, and it will be interesting to determine if the WD domain interacts with RUBCN or UVRAG or components of the CYBB/NOX2 complex. Defective clearance of apoptotic cells following LAP deficiency resulting from lack of CYBB/NOX2 or RUBCN in phagocytic cells predisposes mice to an autoimmune disease resembling systemic lupus erythematosus [4]. At 52 wk, *rubcn^{-/-}* mice have increased levels of antibody against double-stranded DNA, anti-nuclear antibodies and deposition of immune complexes in the kidney. Our analysis of LAP-deficient *atg16l1^{E230}* mice at 20–24 wk did not show elevated cytokines or anti-nuclear antibodies (not shown), but this does not preclude development of lupus-like autoimmunity as they age further.

MEFs cultured from *atg16l1^{E226}* mice were unable to activate autophagy in response to starvation, and the mice showed accumulation of SQSTM1 *in vivo*. These mice grew slowly, were infertile and showed defects in liver, brain and muscle homeostasis, and neurological defects similar to those reported for mice with analogous tissue-specific loss of autophagy genes. These mice again highlight the importance of autophagy for maintaining tissue health *in vivo*, but, surprisingly, the *atg16l1^{E226}* mice were able to survive neonatal lethality. These mice therefore differ from mice with systemic deletion of *Atg3*, *Atg5*, *Atg12* or *Atg16l1*, which die within hours of birth because they cannot compensate for loss of placental nutrition [12,14,15]. This suggests that the truncated CCD^{E226} may provide functions that are missing when *Atg16l1* is deleted completely. The CCD^{E226} retains the ATG5 binding domain allowing the CCD^{E226} to bind the ATG12–ATG5 conjugate and assemble into an ATG12–ATG5–ATG16L1 CCD^{E226} complex. This complex may maintain E3 ligase activity and be able to facilitate lipidation of LC3 and autophagosome formation at a low level. Evidence for a low

level of autophagy is provided in Figure 3A where accumulation of SQSTM1 in MEFs from *atg16l1*^{E226} appeared lower than following complete loss of ATG16L1, and there was a faint band for LC3-II. In addition, the requirement for WIPI2 binding to ATG16L1 to initiate autophagy may differ between brain and peripheral tissues. Support for this is provided by gel filtration analysis which suggested that binding of WIPI2 to the E230 glutamate residue in the CCD of ATG16L1 occurred in liver, but binding was much weaker in brain.

The phenotype of the *atg16l1*^{E226} mouse was very similar to the *atg5*-null mouse described by Yoshii et al [24] where ATG5 expression was restored in the brain of *atg5*^{-/-} mice. In common with *atg16l1*^{E226} mice, the *atg5*-null mouse survived neonatal lethality but grew slowly and showed SQSTM1 accumulation in peripheral tissues, particularly liver and muscle. The *atg5*-null mice were sterile and have the pronounced hepatomegaly seen in *atg16l1*^{E226} mice. This makes it possible that a low level of autophagy in the brain of *atg16l1*^{E226} mice allows them to survive neonatal lethality. Indirect evidence for this is provided by the observation that LC3-I levels were not raised in the brains of *atg16l1*^{E226} mice (Figure 8B) compared to muscle (Figure 6B), liver (Figure 4D) and kidney (7B). The truncated CCD^{E226} is able to protect against neonatal lethality, but not able to provide long-term protection against neurological defects. This phenotype is similar to the mice lacking ATG7 in the central nervous system [26] where neurons accumulate SQSTM1 inclusions and ubiquitin, and Purkinje cells and pyramidal neurons are lost from the cerebellar cortex.

Materials and methods

Construction of the targeting vector

A P1 artificial chromosome (PAC) mouse genomic DNA library (Source BioScience, 711_RPCI21mPAC) was screened with a 0.5-kb Xho I-Sal I fragment obtained from the *Atg16l1* IMAGE cDNA clone 6,813,377/AV130 A2 (Source BioScience). A 10-kb XhoI and a 13-kb BamHI fragment, containing exons 1–10 of *Atg16l1*, were subcloned into pBSISK- (Agilent, 212,206). Two stop codons and restriction sites for NheI, XhoI, EcoRV and EcoRI were introduced into exon 6 after amino acid position 230 by PCR. Two 1.5-kb fragments were generated using primer pairs CCAATCCAGGTACCTCTCAG.seq in combination with ATCCTCGAGATCGATGCTAGCCTACTATTCCTTTGCTGCTTCTGCAAG.rev and ATCGATCTCGAGGATATCGAATTCCCTCTACCTGTTGAACAGTG.seq in combination with CCTGGCCCCGGGCATGATAATG.rev, followed by an annealing PCR of the 2 fragments using primers CCAATCCAGGTACCTCTCAG.seq and CCTGGCCCCGGCATGATAATG.rev to generate a 3-kb fragment, which was cloned into a SmaI-cut pUC19 vector (Addgene, 50,005). The bovine growth hormone polyadenylation site (bGH-pA; derived from pPGK-Cre-bpA, Addgene, 11,543) was cloned into the blunt-ended XhoI site, followed by cloning the blunt-ended PGK-Neo-frt cassette [33] into EcoRV. A KpnI-SmaI fragment of an 8.7-kb SacI-SmaI

fragment, generated from the 10-kb XhoI and 13-kb BamHI genomic clones, was then exchanged with the modified exon 6-containing genomic PCR fragment.

Embryonic stem cells and generation of homozygous mice

Embryonic stem cells were cultured as described previously [34]. R1 cells (2x10⁷) [35] were electroporated with 30 µg NotI-linearized targeting vector as described. G418-resistant clones were screened by Southern hybridization for homologous recombination. Positive clones were expanded, re-analyzed by Southern blot analysis and PCR, and injected into C57L/B6 blastocysts. Highly chimeric male founder mice were obtained, which were crossed with C57LB/6 females to obtain heterozygous F1 offspring. The neomycin cassette was removed by crossing F1 offspring with FlpO transgenic mice [36] and mice were subsequently crossed onto a C57L/B6 background. Genotype analysis was performed using primers CAAATATGCCTTCAGAACTG and GCTGTAGTTCCAA TCCCTAA, resulting in 290-bp and 640-bp fragments for wild-type and mutant mice, respectively.

Mice

These studies used adult male and female mice of approximately 2–3 months of age from the first cross of 129 and C57BL/6. All experiments were performed in accordance with UK Home Office guidelines and under the UK Animals (Scientific procedures) Act1986. The growth rate of these mice was estimated by recording weights each week. Mice were killed by schedule-1 procedures and dissected to harvest brain, liver, gastrocnemius muscle and kidney. The weights of the organs were recorded before fixing or freezing.

Cells and cell culture

MEFs were generated by serial passage of cells taken from mice at embryonic day 13.5 and cultured in DMEM (ThermoFisher scientific, 11,570,586) with 10% FCS. BMDMs were generated from bone marrow isolated from femur and tibia flushed with RPMI 1640 (Sigma, R8758). Macrophages were generated by culturing adherent cells in RPMI 1640 containing 10% FCS and CSF1/M-CSF (Peprotech, 315–02; 30 ng/ml) for 6 d. Macrophage populations were quantified by FACS using antibodies against FCGR3/CD16-FCGR2B/CD32, ADGRE1/F4/80 and ITGAM/CD11b (BioLegend, 101,320, 123,107).

Autophagy and LC3-associated phagocytosis

Autophagy was activated by incubating cells in HBSS (ThermoFisher, 11,550,456) to create starvation for 2 h at 37°C. LAP was stimulated in bone marrow-derived macrophages by Pam3CSK4-coupled beads. Carboxyl-modified beads (polybead carboxylate 3.0 µm, 09850) were conjugated with Pam3csk4 (invivogen, TLRL-PMS) by following the manufacturer's protocol (Bangs Laboratories, Inc. Tech Note 205, III.). Pam3CSK4-coupled beads were added to

macrophage cultures at a ratio of 10:1 (bead/cell) for 1.5 h before being fixed and the location of LC3 analyzed by immunofluorescence microscopy.

Tissue western blotting

Dissected tissue was snap-frozen in liquid nitrogen, ground to a fine powder under liquid nitrogen and lysed in RIPA buffer (150 mM sodium chloride, 1% TritonX-100 [Sigma, P1379-1L], 0.5% sodium deoxycholate [Sigma, D-5670], 0.1% sodium dodecyl sulfate [Fisher Bioreagents, BP166-500], 50 mM Tris, pH 8.0) containing protease (Sigma, P8340) and phosphatase (Sigma, P5726) inhibitors followed by homogenization and freeze thaw. Samples were clarified by centrifugation (10,600 g, 10 min at 4°C). Supernatants containing ~10 µg protein were boiled in Laemmli buffer followed by SDS-PAGE using 4–12% gradient gels (Expedeon, NBT41212). The resolved proteins were electro-blotted onto nitrocellulose membrane (Bio-Rad, 1,620,115), blocked (5% skimmed milk in 1X TBS [50mM Tris (pH 7.5), 150mM NaCl], 1 h, room temperature) and then probed first with appropriate primary (ATG16L1 [MBL, M150-3], SQSTM1/p62 [Abcam, ab91526], GAPDH [Abcam, ab9482] and LC3A/B [Cell Signalling Technology, 4108]) and then secondary antibody (Cell Signalling Technology, 7074S and 7076S). Blots were visualized by exposure to Supersignal West Pico chemiluminescent substrate (ThermoFisher Scientific, 34,080). Bands were quantified through ImageJ (NIH, USA), analyzed (unpaired t-test) and plotted via GraphPad prism 7 software.

Cell western blotting

Protein was extracted using M-PER (ThermoFisher Scientific, 78,501) with complete protease inhibitor cocktail (Sigma, 04693159001) for 30 min on ice. Samples were clarified by centrifugation (10,600Xg, 10 min). From the supernatants, protein concentrations were determined using the BCA protein assay system (ThermoFisher Scientific, 23,225) according to the manufacturer's protocol. Protein (20 µg) was separated on a precast 4–12% gradient SDS-PAGE gel (Expedeon, NBT41212) and transferred to immobilon PVDF (Millipore, IPFL00010) for blotting. Membranes were probed using antibodies for ATG16L1 (MBL), SQSTM1/p62, (Abcam), LC3A/B and ACTB/actin (Sigma, A5441). Primary antibodies were detected using IRDye labelled secondary antibodies (LI-COR biosciences, 926–32,211, 926–68,020) at 1:10,000 dilution. Proteins were visualized using the Odyssey infrared system (LI-COR).

Gel filtration chromatography

Freshly dissected livers and brains were suspended in cold phosphate-buffered saline (Oxoid, BR0014G) containing protease inhibitors (Roche, 05892791001) and homogenized using a Dounce homogenizer. Particulate material was removed by sequential centrifugation at 100Xg and 13,000Xg (4°C) for 20 min. The supernatants were clarified by ultracentrifugation (100,000Xg, 4°C, 1 h) and analyzed by the gel filtration using an ENrichTMSEC 650 (Bio-Rad, 780–1650,) column and AKTA purifier (GE Healthcare) to

collect 0.5-ml fractions. Fractions were analyzed by SDS-PAGE followed by western blotting on PVDF membranes probed for ATG16L1, ATG5 (Abcam, ab108327) and WIPI2 (Abcam, ab101985). The void volume (V_0) was estimated using Blue dextran (Sigma, D4772-1VL) and the elution volumes (V_e) of molecular size standards (Sigma, MWGF1000) allowed the determination of $V_e: V_0$ ratios to create a standard curve.

Cytokine assays

Serum from young (2–3 months) and aged (5–6 months) mice were analyzed for cytokines using ProcartaPlexTM Simplex Immunoassay kits (ThermoFisher Scientific, EPX01A-26,015–901, EPX01A-20,603–901, EPX01A-26,004–901, EPX01A-26,005–901, EPX01A-20,607–901 and EPX01A-26,002–901) by following the manufacturer's instructions. Samples were read on a LuminexTM 100/200TM instrument (Luminex Corp.).

Histochemistry

Dissected tissues were fixed in 10% neutral buffer formalin (Sigma, HT501128), dehydrated, paraffin embedded and sectioned (5-µm thickness) prior to staining in hematoxylin and eosin (H&E). For immunohistochemistry deparaffinized and rehydrated sections were subjected to microwave-based antigen retrieval in citrate buffer (~0.24% trisodium citrate dihydrate, ~0.038% citric acid, in water). The sections were then incubated in hydrogen peroxide buffer (10% H₂O₂ in methanol) to mask any background peroxidase activity followed by treatment with blocking solution (10% goat serum [Gibco, 16,210–072], 0.30% Triton X-100 in PBS). Sections were stained with appropriate primary (anti SQSTM1/p62 antibody, anti MKI67/Ki67 antibody [Abcam, ab66155], anti ITGAM/Cd11b antibody [Abcam, ab133357]) and secondary antibodies (anti rabbit-HRP; Dako, K4003). The signals were developed with chromogen buffer (Dako, K3468). Tissue sections were mounted using cover glass and mounting medium (Neomount; Merck, 1,090,160,100) and imaged using 20X and 40X objectives on a bright-field microscope (Zeiss). The images were analyzed using Axio Vision software (cell circumference measurement, Axio Vision SE64 Rel. 4.8) and ImageJ software (cell counter plugin, NIH, USA). The obtained data were analyzed (unpaired t test) and plotted through GraphPad prism 7 software.

Fluorescence imaging

Cells grown on glass coverslips were fixed at –20°C in ice cold methanol for 7 min, then blocked in 5% goat serum, 0.3% Triton X-100 in PBS (Sigma, G9023; X100). Cells were incubated with anti LC3A/B (Cell Signalling Technology, 4108; 1:500 in 1% BSA [Europa Bioproducts Ltd., EQBAH62-1000], 0.3% Triton X-100 in PBS). Washed cells were incubated with secondary antibody anti-rabbit-Alexa Fluor 488 (Life Technologies, A11008) and counterstained with 4', 6 diamidino-2-phenylindole (DAPI; ThermoFisher Scientific, 10,116,287) and mounted on slides with Fluoromount-G from Southern biotech (ThermoFisher Scientific, 15,586,276). Cells were imaged on a Zeiss Imager

M2 Apotome microscope with a 63X, 1.4 NA oil-immersion objective using 365 ± 40 nm excitation and 445 ± 25 nm emission for DAPI, 470 ± 20 nm excitation and 525 ± 25 nm emission for LC3. Images were obtained using a Zeiss Axioplan microscope with bright field.

Statistics

Unpaired t test was employed for the data analysis across all the experiments. The data were analyzed and plotted through GraphPad prism 7 software.

Microscopy

All the fluorescent imaging was carried out using an Apotome microscope from Zeiss, fitted with 63X objective. All the immunohistochemistry for bright-field imaging was carried out using an Axioplan 2 microscope from Zeiss, fitted with 20X, 40X objectives and a colored Axio Cam HRc camera from Zeiss.

Acknowledgments

This work was funded in part by the BBSRC Institute Strategic Programme Gut Health and Food Safety (BB/J004529/1) and by the Norwich Medical School through studentships to MA and BB. SR is supported by a PhD studentship from Crohn's in Childhood Research Association (CICRA).

Disclosure statement

No potential conflict of interest was reported by the authors.

Funding

This work was supported by the Biotechnology and Biological Sciences Research Council [(BB/J004529/1)].

ORCID

Ulrike Mayer  <http://orcid.org/0000-0003-2328-0052>

References

- Mizushima N, Levine B. Autophagy in mammalian development and differentiation. *Nat Cell Biol.* 2010;12(9):823–830.
- Mizushima N, Komatsu M. Autophagy: renovation of cells and tissues. *Cell.* 2011;147(4):728–741.
- Martinez J, Malireddi RS, Lu Q, et al. Molecular characterization of LC3-associated phagocytosis reveals distinct roles for Rubicon, NOX2 and autophagy proteins. *Nat Cell Biol.* 2015;17(7):893–906.
- Martinez J, Cunha LD, Park S, et al. Noncanonical autophagy inhibits the autoinflammatory, lupus-like response to dying cells. *Nature.* 2016;533(7601):115–119.
- Florey O, Kim SE, Sandoval CP, et al. Autophagy machinery mediates macroendocytic processing and entotic cell death by targeting single membranes. *Nat Cell Biol.* 2011;13(11):1335–1343.
- Florey O, Gammoh N, Kim SE, et al. V-ATPase and osmotic imbalances activate endolysosomal LC3 lipidation. *Autophagy.* 2015;11(1):88–99.
- Jacquin E, Leclerc-Mercier S, Judon C, et al. Pharmacological modulators of autophagy activate a parallel noncanonical pathway driving unconventional LC3 lipidation. *Autophagy.* 2017;13(5):854–867.
- Sanjuan MA, Dillon CP, Tait SW, et al. Toll-like receptor signaling in macrophages links the autophagy pathway to phagocytosis. *Nature.* 2007;450(7173):1253.
- Huang J, Canadien V, Lam GY, et al. Activation of antibacterial autophagy by NADPH oxidases. *Proc Natl Acad Sci.* 2009;106(15):6226–6231.
- Roberts R, Al-Jamal WT, Whelband M, et al. Autophagy and formation of tubulovesicular autophagosomes provide a barrier against nonviral gene delivery. *Autophagy.* 2013;9(5):667–682.
- Chen X, Khambu B, Zhang H, et al. Autophagy induced by calcium phosphate precipitates targets damaged endosomes. *J Biol Chem.* 2014;289(16):11162–11174.
- Kuma A, Hatano M, Matsui M, et al. The role of autophagy during the early neonatal starvation period. *Nature.* 2004;432(7020):1032–1036.
- Komatsu M, Waguri S, Ueno T, et al. Impairment of starvation-induced and constitutive autophagy in Atg7-deficient mice. *J Cell Biol.* 2005;169(3):425–434.
- Sou Y-S, Waguri S, Iwata J-I, et al. The Atg8 conjugation system is indispensable for proper development of autophagic isolation membranes in mice. *Mol Biol Cell.* 2008;19(11):4762–4775.
- Saitoh T, Fujita N, Jang MH, et al. Loss of the autophagy protein Atg16L1 enhances endotoxin-induced IL-1 β production. *Nature.* 2008;456(7219):264–268.
- Malhotra R, Warne JP, Salas E, et al. Loss of Atg12, but not Atg5, in pro-opiomelanocortin neurons exacerbates diet-induced obesity. *Autophagy.* 2015;11(1):145–154.
- Heckmann BL, Boada-Romero E, Cunha LD, et al. LC3-associated phagocytosis and inflammation. *J Mol Biol.* 2017;429:3561–3576.
- Dooley HC, Razi M, Polson HE, et al. WIPI2 links LC3 conjugation with PI3P, autophagosome formation, and pathogen clearance by recruiting Atg12–5–16L1. *Mol Cell.* 2014;55(2):238–252.
- Fujita N, Itoh T, Omori H, et al. The Atg16L complex specifies the site of LC3 lipidation for membrane biogenesis in autophagy. *Mol Biol Cell.* 2008;19(5):2092–2100.
- Bajagic M, Büsing P, Scrima A. Structure of the WD40-domain of human ATG16L1. *Protein Sci.* 2017;26:1828–1837.
- Mizushima N, Kuma A, Kobayashi Y, et al. Mouse Apg16L, a novel WD-repeat protein, targets to the autophagic isolation membrane with the Apg12–Apg5 conjugate. *J Cell Sci.* 2003;116(9):1679–1688.
- Fletcher K, Ulferts R, Jacquin E, et al. The WD40 domain of ATG16L1 is required for its non-canonical role in lipidation of LC3 at single membranes. *Embo J.* 2018;37:e97840.
- Lamprinak D, Beasy G, Zhekova A, et al. Icf3-associated Phagocytosis is required for Dendritic cell inflammatory cytokine response to gut commensal Yeast *Saccharomyces cerevisiae*. *Front Immunol.* 2017;8.
- Yoshii SR, Kuma A, Akashi T, et al. Systemic analysis of Atg5-null mice rescued from neonatal lethality by transgenic ATG5 expression in neurons. *Dev Cell.* 2016;39(1):116–130.
- Masiero E, Agatea L, Mammucari C, et al. Autophagy is required to maintain muscle mass. *Cell Metab.* 2009;10(6):507–515.
- Komatsu M, Waguri S, Chiba T, et al. Loss of autophagy in the central nervous system causes neurodegeneration in mice. *Nature.* 2006;441(7095):880–884.
- Fujita N, Saitoh T, Kageyama S, et al. Differential involvement of Atg16L1 in crohn disease and canonical autophagy analysis of the organization of the Atg16L1 complex in fibroblasts. *J Biol Chem.* 2009;284(47):32602–32609.
- Suzuki K, Kirisako T, Kamada Y, et al. The pre-autophagosomal structure organized by concerted functions of APG genes is essential for autophagosome formation. *Embo J.* 2001;20(21):5971–5981.
- Travassos LH, Carneiro LA, Ramjeet M, et al. Nod1 and Nod2 direct autophagy by recruiting ATG16L1 to the plasma membrane at the site of bacterial entry. *Nat Immunol.* 2010;11(1):55–62.
- Kimura T, Jain A, Choi SW, et al. TRIM-mediated precision autophagy targets cytoplasmic regulators of innate immunity. *J Cell Biol.* 2015;210(6):973–989.

- [31] Boada-Romero E, Letek M, Fleischer A, et al. TMEM59 defines a novel ATG16L1-binding motif that promotes local activation of LC3. *Embo J.* 2013;32(4):566–582.
- [32] Hu J, Li G, Qu L, et al. TMEM166/EVA1A interacts with ATG16L1 and induces autophagosome formation and cell death. *Cell Death Dis.* 2016;7(8):e2323.
- [33] Conrad M, Brielmeier M, Wurst W, et al. Optimized vector for conditional gene targeting in mouse embryonic stem cells. *Biotechniques.* 2003;34(6):1136–1138, 40.
- [34] Mayer U, Saher G, Fässler R, et al. Absence of integrin $\alpha 7$ causes a novel form of muscular dystrophy. *Nat Genet.* 1997;17(3):318–323.
- [35] Nagy A, Rossant J, Nagy R, et al. Derivation of completely cell culture-derived mice from early-passage embryonic stem cells. *Proc Natl Acad Sci.* 1993;90(18):8424–8428.
- [36] Kranz A, Fu J, Duerschke K, et al. An improved Flp deleter mouse in C57Bl/6 based on Flpo recombinase. *Genesis.* 2010;48(8):512–520.